

Investigating Abundances in Galaxy Clusters and Gas Motions in M87 using XRISM

by

Neo Dizdar

A thesis
presented to the University of Waterloo
in fulfillment of the
thesis requirement for the degree of
Masters of Science
in
Physics and Astronomy

Waterloo, Ontario, Canada, 2024

© Neo Dizdar 2024

Author's Declaration

I hereby declare that I am the sole author of this thesis. This is a true copy of the thesis, including any required final revisions, as accepted by my examiners.

I understand that my thesis may be made electronically available to the public.

Abstract

While being the forefront of extra galactic diffuse x-ray astrophysics, the history of galaxy cluster formation and longevity still contain many unknowns. Two prevalent issues currently exist, the metal abundance history of clusters and the conversion rate of jet energy into atmospheric kinetic energy. The creation of XRISM, a new X-ray imaging and spectroscopy mission, may lead to gleaning information for these two missing links. XRISM's payload contains an instrument with the highest spectral resolution (5 eV) in the field of x-ray astronomy so far. With this resolution we observe metal abundances and the broadening of metal lines through turbulent motions in the intracluster medium.

In this thesis I present the conversion of data from the Chandra X-ray Observatory to XRISM. This includes the preparation and selection of clusters in Chandra, simulating selected clusters for XRISM and applying for proposals. Finally I extract abundance and velocity information from the Virgo cluster's early XRISM data.

I prepare a subset of 16 galaxy clusters with a wide array of morphologies and redshifts using the Chandra X-ray database. This produces radial profiles of metallicity, temperature and cooling time for each cluster. The entire subset shows that the metallicity asymptotes at 0.3 solar abundance (Z_{\odot}) for each cluster, this independence to redshift implies that there was early enrichment in clusters. Within this sample of clusters there are 2 that appear as outliers for the two category system of cool core and non-cool core, implying that the categories may be dated. This dataset of clusters is reformatted into datasheets with the addition of extracting a spectrum in the size of XRISM's footprint. These datasheets are used to select candidate clusters for XRISM observation proposals. The 3 selected clusters are HydraA, A2199 and MS07. This selection was done by creating upscaled simulations of Chandra spectra mimicking the expected properties of XRISM. The minimum exposure time required to accurately model the simulated turbulent broadening velocity was found by modelling the Fe-K complex in each cluster. The pointings and required exposure times are collected and composed into proposals to observe clusters in XRISM's A01 cycle.

To conclude the thesis, I present a primary analysis of the Virgo cluster's structure and atmospheric motions. The cluster shows a significant super solar abundance ratio over all metals found between 1.7 - 10 keV. The turbulent velocity in the cluster is low ($57 \frac{km}{s}$ - $149 \frac{km}{s}$) as is expected from a weaker jet of $\sim 10^{43}$ ergs/s. The bulk flow shows a small systematic blue shift over all 4 pointings, suggesting that the brightest cluster galaxy is oscillating around the center of the gravitational potential well. Narrowband observations show that cooler softband metals move at higher speeds in most of the pointings in this cluster and have increased abundance in the southwest arm. This suggests the need of two temperature fitting in clusters and a separate study between "hotter" and "cooler" metals.

Acknowledgments

I would like to thank my supervisor Prof. Brian McNamara for the opportunity at working with new data in galaxy clusters, guiding me into the right direction and his continuous support. I thank my committee members Michel Fich and James Taylor for their suggestions and hard hitting questions in my presentations. I would like to thank the members of the M87 XRISM team for taking me in and helping with modelling errors. I thank colleagues and friends in Brian's research group for their guidance and assistance with handling new data. In particular I would like to thank Julian Meunier and Tom Rose for our collaborative work between the XRISM teams. I thank Prathamesh Tamhane for getting me started with Chandra analysis and XRISM simulation work.

I have to thank my undergraduate friends, Erik, Ethan, Damian, Jacob, Emma, Jess and everyone else for their continuous jokes, game nights and overall support even to this day.

I would like to thank all of the professors at the University of Waterloo that taught both in undergraduate and graduate school, your knowledge culminated into me writing this thesis.

And finally I thank my parents and my brother for listening to my ramblings about astrophysics, showing continuous love and support every single day.

Table of Contents

Author's Declaration	ii
Abstract	iii
Acknowledgments	iv
List of Figures	viii
List of Tables	x
1 Galaxy Cluster Background	1
1.1 Hot Atmospheres	2
1.1.1 Bremsstrahlung Emission	2
1.2 Metallicity	3
1.2.1 SNeIa and SNeII	4
1.3 Cooling Clusters	6
1.4 AGN Jets	8
1.5 Cavities	12
1.5.1 Cavities: Resisting Instabilities	15
1.5.2 Cavities: Uplift	20
1.6 X-Ray Spectral Components	23

2 CHANDRA: Low Spectral Resolution Radial Metallicities	26
2.1 CHANDRA	27
2.1.1 Cluster ObsIDs	29
2.2 Data Extraction	30
2.2.1 RMFs and ARFs	32
2.3 Modelling CHANDRA Spectra	34
2.3.1 Xspec Model Components	34
2.3.2 Model Outputs	37
2.4 Data Analysis: Radial Profiles	39
2.5 Data Analysis: XRISM Region	49
2.6 Conclusion	52
3 Simulating High Spectral Resolution Galaxy Clusters	53
3.1 XRISM	54
3.1.1 Gate Valve	56
3.2 Simulating Spectra	58
3.3 Selecting Clusters	60
3.3.1 HydraA	64
3.3.2 MS07	66
3.3.3 A2199	67
3.4 Modelling Broadening	68
3.5 Conclusions & Proposal Outcomes	74
3.6 Future Work	76
4 XRISM: A Study of M87’s Intracluster Medium	77
4.1 M87	78
4.2 Data Extraction	80
4.3 Observing Metals	80

4.4	Model Selection	83
4.5	Data Analysis	85
4.5.1	SPEX or Xspec	86
4.5.2	Metallicities	88
4.5.3	Turbulent Broadening	90
4.5.4	Bulk Motions	91
4.6	Conclusion	93
5	Conclusion	95
References		98
APPENDICES		110
A	Chandra Cluster Datasheets	111
A.1	XRISM Narrowbands	111
A.2	The Datasheets	113

List of Figures

1.1	Metals Produced by Different Processes	5
1.2	HerculesA Multi-Wavelength image	11
1.3	Motion of Cavities (and Reverse Jets)	14
1.4	Velocity Vectors of 4 Cavities in Different ICM Fields after 150 Myr.	17
1.5	Effects of Viscosity on Generating Cavities	19
1.6	Simulated Displacement by Cavities	21
1.7	Simulated Displacement Energy Gain	21
1.8	Components of an X-Ray Continuum	24
2.1	ACIS CCD format	28
2.2	Abell 426 (Perseus Cluster) Summed ObsID	31
2.3	A426 RMF and ARF	33
2.4	A426 Bapec vs Btapec model	36
2.5	Radial Spectra of A426	38
2.6	Location of Annuli on A426	38
2.7	Cool core and non-cool core cluster	39
2.8	A2029 Radial Properties	40
2.9	A2319 Radial Properties	40
2.10	A2199 Dust Core Example	43
2.11	A2142 Flat Metallicity Cool Core Cluster	43
2.12	A3571 Intermediate Cluster	44

2.13	Galaxy Cluster Radial Metallicity Comparison (no error bars)	46
2.14	Mass and SFR comparisons to Radial Trends	48
2.15	Metals in A426 Spectrum	50
3.1	Hitomi Perseus Spectrum	55
3.2	Gate Valve Open and Closed Simulation	57
3.3	M87 XRISM Simulated Images	59
3.4	Fe-K Complex Lines	61
3.5	HydraA Pointing Proposal	65
3.6	MS07 and A2199 Pointing Proposal	67
3.7	Fe-K Multifit Model	70
3.8	Fe-K Single-fit Model	70
3.9	HydraA Proposal Simulations	73
4.1	XRISM M87 Pointings	79
4.2	XRISM Pixel Values	81
4.3	M87 Central Pointing Xspec Model	84
4.4	Broadband Turbulence Comparison SPEX vs Xspec	87
4.5	Metallicities of M87	88

List of Tables

2.1	List of Clusters and ObsIDs	29
2.2	List of Cool Cores and Non Cool Cores	41
2.3	Cluster Data found in Datasheets	51
3.1	Photon Counts of Simulated clusters	63
3.2	Modelled Velocity Broadening vs True Values	71
4.1	Narrowband Limits on XRISM Models	82
4.2	SPEX vs Xspec: Fe Central Pointing	86
4.3	M87 Narrowband Turbulent Velocity	90
4.4	M87 Observed Bulk Motion	91
4.5	M87 Heliocentric Bulk Motion	92

Chapter 1

Galaxy Cluster Background

Galaxy clusters are the largest gravitationally bound structures in the universe having a mass range between 10^{14} and $10^{15} M_{\odot}$. Their masses are primarily composed of dark matter (80%), with 12% attributed to a hot gaseous material (intracluster medium), and only 8% to stars [49]. These massive objects are normally found at intersections of cosmic filaments [9, 49]. Surprisingly while being one of the largest structures there are still many unknowns about the evolution of clusters, mainly how active galactic nuclei heat the intracluster medium (ICM), and why metal abundances of clusters are found to be higher than expected. Most clusters contain a brightest cluster galaxy (BCG), which is found at the center of the galaxy cluster's potential well. As all massive galaxies host a supermassive black hole and BCGs fit the requirements to host one, it is expected to find a supermassive black hole center of most clusters [18]. When large influxes of matter fall towards the bottom of a galaxy cluster's potential well the BCG's supermassive black hole becomes active by tangling magnetic field lines produced in the growing accretion disk. This process emits radiation throughout the electromagnetic spectrum. Beyond the thermal emission of the accretion disk the black hole ejects particles at high speeds in the form of relativistic jets. These jets appear as large radio lobes, producing bright arms in the radio band [8, 105]. These regions of continuous emission around the active black holes are named active galactic nuclei, encompassing both the black hole and its immediate surroundings. AGN jets and other emissions are theorized to pump energy back into the environment of the galaxy cluster, reheating and pushing out cooled out gas into the surrounding ICM [120].

1.1 Hot Atmospheres

The intracluster medium (ICM) is a large region of plasma composed of mostly H and He pervading the entire galaxy cluster. This plasma is in hydrostatic equilibrium with the potential of the cluster. This plasma is heated to over 1.7 keV (approximately 20 million Kelvin) due to accretion shocks. Extended objects with plasma temperatures less than this limit exist but are given a different classification: galaxy groups, and will not be covered further in this thesis [75]. This plasma surrounding the galaxy cluster is very diffuse, having a density around $10^{-3} \frac{\text{atoms}}{\text{cm}^3}$ [99]. The optically thin plasma of the ICM glows in the X-ray band, this is between 10^{43} and $10^{46} \frac{\text{ergs}}{\text{s}}$ [70]. A majority of the glow is produced through bremsstrahlung radiation.

1.1.1 Bremsstrahlung Emission

A bremsstrahlung photon is emitted by a free-free coulomb interaction between an electron and an ion. The cross-section of this interaction scales the amount of energy emitted, with smaller distances producing photons at higher frequencies [42]. This process defines most of the full X-ray continuum emitted by the ICM and is treated as background emission for calculating metal abundances.

The emissivity of thermal bremsstrahlung photons shapes the expected continuum of the cluster's spectrum.

$$\epsilon_{\text{ff}} = 1.4 \times 10^{-27} Z^2 n_e n_i \sqrt{T} \bar{g} \quad \frac{\text{ergs}}{\text{cm}^3 \text{s}} \quad [97]. \quad (1.1)$$

Eq 1.1 is defined by the charge of an ion (Z), the number densities of electrons and ion (n_e and n_i) the temperature of the gas (T) and the frequency averaged Gaunt Factor (\bar{g}). The Gaunt Factor is a quantum correction to the cross section between the two particles.

There is a higher probability of more free-free interactions at larger radii, which produces more low energy photons approaching asymptotically towards 0eV. While this is found in simulations, in real observations the lowest X-ray energies in the spectra appear to attenuate. This is caused by instrumental filtering as the X-ray CCD will deflect rays not strong enough to fully penetrate the instrument's components, thus removing them from the observed continuum. On the opposing end there is an upper threshold for X-ray emission: the maximum photoenergy of an electron. This limit must occur since bremsstrahlung radiation is not the production of energy, merely the conversion of kinetic energy into radiation. Under the law of conservation of energy there cannot be more X-ray energy produced than the kinetic energy input by the electron.

1.2 Metallicity

The ICM consists of primarily ionized hydrogen (75% of gas mass), helium (23%) and other ionized heavier elements. Some of the most prominent x-ray lines found in the cluster's atmosphere include: S, Si, O, Ca, Ni, Ar, Mg, and Fe. Abundances of each metal are obtained through observing the flux of each element's spectral fingerprint. These fingerprints are fluorescent lines produced by an optically thin plasma in ionization equilibrium. Characteristic spectral lines and recombination lines can be used to define the relative abundance of each element. This allows us to measure the number of photons produced in these lines over a set exposure time and compare to solar values. Therefore the abundances of metals in a galaxy cluster is always given as a ratio in terms of solar values.

Iron is one of the brightest metals to observe when measuring the metallicity of the ICM as it has two spectral line complexes with high emissivity in the X-ray continuum. These two complexes are named Fe-L and Fe-K, relating to photons emitted by electron transitions to the first (K) and second (L) electron shells [19]. Fe-L is located around 1 keV and Fe-K is located around 6.7 keV in the X-ray spectrum. CHANDRA, a low spectral resolution X-ray instrument, uses these two lines to measure metal content in galaxy clusters, importantly it has a high image resolution allowing for radial metallicity measurements. Through this method a trend appears which the metallicity in the outer regions of clusters asymptote towards $0.3 Z_{\odot}$ [107]. This value is higher than expected, and the constant observations of $0.3 Z_{\odot}$ leads to early enrichment theories. The metallicity in the center of clusters is related to one of two cluster classifications, cool core clusters and non-cool core clusters. Within non-cool core clusters the metallicity does not appear to change between central and outer regions, stagnating around 0.3. In most cool core clusters there is a steady rise in metallicity towards the center of the cluster, ranging from 0.5 to $3 Z_{\odot}$ [74, 104, 107]. Some outliers to this trend appear where the metallicity rises towards the core and proceeds to show a significant drop at the central-most regions. Theories suggest that if this sudden extinction is occurring due to ions cooling out and combining with dust at the cores of clusters, these compounds would then stop emitting bremsstrahlung photons [74, 85, 86].

Spectral lines are broadened by four main factors: thermal broadening, Doppler broadening, instrumental broadening and natural line width. This can be problematic if characteristic line energies are too close in proximity. Broadening leads to overlapping lines that require model fitting to trace back the original line producing the photon.

1.2.1 SNeIa and SNeII

Most elements are produced by supernovae. Atoms with higher atomic numbers such as Fe, Si, S and Mg must be produced by the process of stellar supernovae. Thus observing metallicity values within galaxy clusters defines the frequency of past supernovae in these large structures. Since galaxy clusters may be considered a “closed box”, as external enrichment is rare aside from mergers, the history of all metal enrichment a galaxy cluster has experienced can be found through observing their spectral abundances [71]. The two main types of supernovae that will be discussed are the thermal runaway supernovae (SNeIa) and the core collapse supernovae (SNeII).

Type 1a supernovae form when a white dwarf star accretes mass beyond the Chandrasekhar limit. The dwarf star fails to emit enough electron degeneracy pressure to offset the gravitational force acting on its outer layers, causing a collapse [62, 95]. This collapse initiates nuclear fusion within the core and will eject its outer layers in a luminous shock-wave known as a supernova. As white dwarves typically do not form with masses higher than $1.44 M_{\odot}$ (the Chandrasekhar limit) Type 1a supernovae must occur through accretion or binary interactions. The most common model is a binary system wherein a red giant forms next to a white dwarf. This red giant enlarges past the Roche limit as the outer layers get pulled in by the white dwarf’s gravitational well, allowing the white dwarf to accrete mass from it. This accretion process bypasses the Chandrasekhar limit [62]. Type 1a supernovae will synthesize Fe, Ar, Mn and a subset of elements that surround the Iron peak like Cr and Ni [35, 58]. Notably Type 1a supernovae may also output Ca, Ti, V, Si and S in less prominent amounts. Si and S should be focused on as they are also affected by SNcc supernovae, and will produce characteristic emission lines in the ICM [58]. When observing Fe, Cr, Ni and Mn one can extrapolate their abundances with the amount of Type 1a supernovae that have occurred.

The other common type of supernovae found in clusters are the Type II core collapse supernovae. Core collapse occurs when stars produce Fe in their core, as they create layers of different elements that undergo fusion when the previous element “runs out” (is trapped in an upper layer). As fusing Fe will actually absorb energy, being the peak in the binding energy curve, it leaves an inert Fe core within stars at the end of their lifecycle. Once this Fe core reaches the Chandrasekhar limit, much like the type 1a supernovae, the electron degeneracy pressure fails to oppose gravity and the core collapses within seconds [54]. As this occurs the outer layers begin fall onto the rebounding core, expelling energy through nuclear fusion and shedding the outer regions in a large supernova. The mass and metallicity of the parent star alter the final outcome of this process, producing a black hole or neutron star, more importantly trapped metals are emitted out into the surrounding environment. Core collapse supernovae proceed to expel the stable alpha elements from

the trapped stellar layers: O, Ne, Mg, Si and S [114]. They also produce more metals but only a few are visible in the ICM’s X-ray broadband, such as Ar, Ca and some Ni. Observing the abundance of O, Ne, Mg, Si and S gives a hint to the amount of core collapse supernovae that have occurred within a cluster [4].

The ICM can also be enriched through stripping, as stellar winds may interact with stars from the asymptotic giant branch. These winds strip metals like C and N off of the enlarged outer layers of the giant stars [35, 48]. The overall effect that this has on the ICM is minuscule in comparison to the metals produced by SNeIa and SNII.

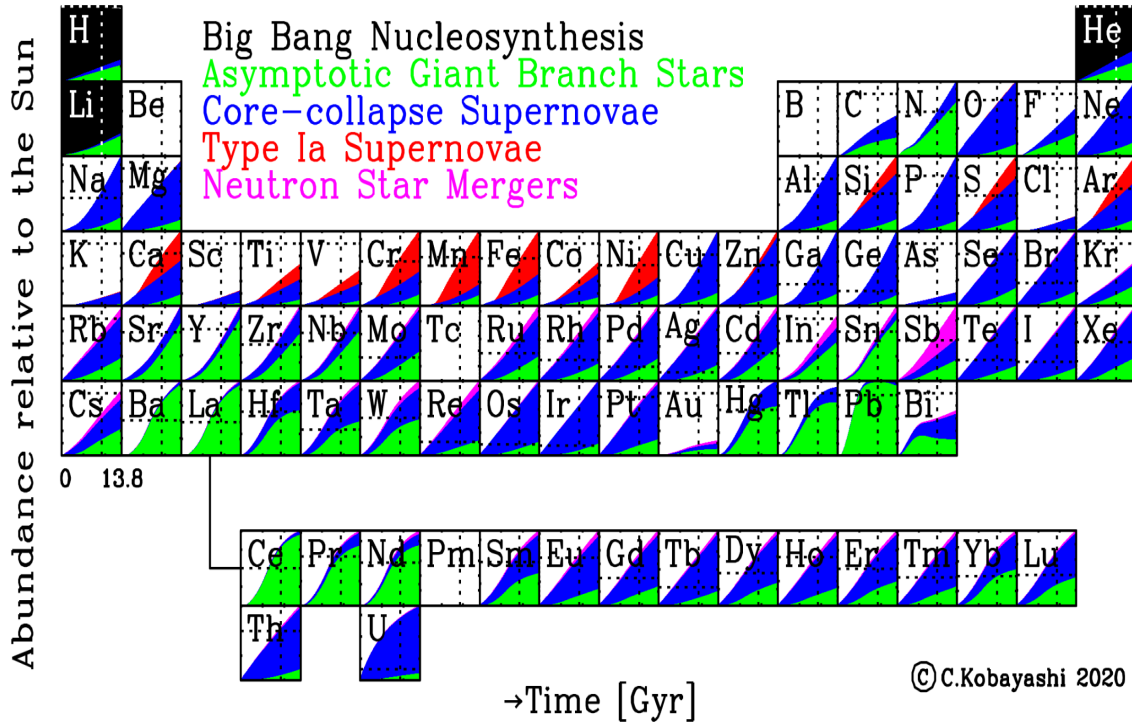


Figure 1.1: A chart showcasing the process of metal enrichment of galaxies and clusters caused by different processes. The dotted line defines solar metallicity. By C. Kobayashi (2020) [58]

There is an issue with the current paradigm comparing abundances to the rate of supernovae in galaxy clusters. Current values of stellar metallicities are well under the metallicity measured in the ICM, this implies that galaxy clusters had to be enriched by early type galaxies. There had to be galaxies with iron values from 2-5 times the iron mass we see today to produce the abundance ratios seen in most clusters [4, 65]. Since

Type 1a supernovae are the main process known to expel iron into galaxy clusters it would imply that such supernovae were more frequent in the early universe. There is no physical reason that more SNeIa occurred, in fact the opposite has been predicted (this can be seen in Fig. 1.1 as the abundance ratio increases with time). Observations of higher redshift clusters show no change to this trend proving that there is not a late stage influx of metals introduced into clusters. This instead supports current early enrichment theories [71, 77]. Deeper studies of metallicities in high redshift clusters with telescopes such as ATHENA may be required to truly understand how galaxy clusters have obtained this injection of metals in their early life.

1.3 Cooling Clusters

There are currently two categories of galaxy clusters that are dependent on the cooling timescale of the ICM. If the cooling time is less than the Hubble time of the cluster then it is classified as a cool core cluster (CC), otherwise if the cooling time is greater than the age of the cluster then it is classified as a non-cool core cluster (NCC). Cool core clusters are defined by their decrease in temperature and entropy within their central regions of the cluster. There currently is no trend in the distance from the center in which this drop of temperature occurs, meaning that there are multiple cooling factors affecting clusters uniquely [53]. The central region of a cool core cluster is still a hot plasma that can emit bremsstrahlung photons making it visible to x-ray telescopes. Cool cores have temperatures that decrease to a factor of 3 lower than the surrounding temperature of the heated ICM [98]. For example Abell 2199 has an ICM temperature of 4.7 keV (5.4×10^7 K) in the outer regions of the cluster, whilst the inner core drops to a temperature of 2.2 keV (2.5×10^7 K) [values from the datasheets]. It is believed that “cooling flows” is the mechanism responsible for these cool cores.

Over time the plasma undergoes radiative cooling from the continuous emission of X-rays and thus increases the density to the point that radiative pressure fails to separate the cooled out plasma. This creates denser clouds of the ICM which in turn start migrating towards the center of the gravitational potential well. This occurs because the denser cloud experiences a higher gravitational pull than its heated plasma environment, so much so that gravity overtakes the radiative pressure of the plasma underneath it. These clumps naturally continue to migrate towards the center until it reaches hydrostatic equilibrium. This process is then repeated throughout the cooler/lower entropy regions at a higher rate as the entropy is proportional to cooling time. The cooling time equation is:

$$t_{\text{cool}} = \frac{p}{(\gamma - 1)n_e n_H \Lambda(T)}. \quad (1.2)$$

Within Eq. 1.2 p is defined as gas pressure, γ is considered to be Laplace's coefficient, or more well known as the adiabatic index, and $\Lambda(T)$ is the cooling function. As the entropy of the ICM plasma drops it lowers its gas pressure, this shows that the cooling time shortens for denser gases. Observations of cool core clusters show a temperature gradient, allowing for their inner cores to be shell-like. Due to multiple different heating and cooling factors the size of these cool core regions do not have a concrete relation between different clusters, but a range has been defined using metal enrichment. Generally enrichment begins to occur within a region about 100-150kpc from the center of the cluster [90]. These methods of cooling can be used to then explain why the BCG, which tends to be an older elliptical galaxy, experiences higher than expected rates of stellar formation beyond the standard 1 Solar mass per year. It is theorized that the accretion of cooled gas in the surrounding environment causes this. Since the BCG would then contain more metals than standard galaxies due to its continuous accretion of gas in a metal rich environment the high star formation rate is expected, as in high mass galaxies an increase in metals is known to increase stellar formation rates [117].

When comparing the size and number of cool core clusters and non-cool core clusters one must pay attention to the Malmquist Bias. The Malmquist bias is an intrinsic systematic bias that occurs when observing the luminosity of objects in space [12]. This selection bias was first noticed when stars and galaxies visible at higher redshifts were missing low luminosity stars, implying that at high redshifts all stars had a higher luminosity. This of course is untrue, and is due to the inverse square law wherein the brightness of a luminous object decreases by $\frac{1}{r^2}$, thus making less luminous objects at high redshifts indistinguishable to the surrounding noise. This bias is prevalent when comparing cool core and non-cool core clusters. As the cores of cool core clusters contain denser optically thin plasma these regions appear to have a higher luminosity. Non-cool core clusters do not have bright structures as they have yet to produce cooling flows. This means that non-cool core clusters will appear less often, as they have to either be at very low redshifts or have a large angular size in the sky (see: Coma Cluster). This, in tandem with no visible cavities in non-cool core clusters causes datasets to focus more on cool core clusters.

1.4 AGN Jets

The cooling time for the plasma in the ICM is less than 1 GYr [71]. With classical cooling flow models it is anticipated that around 1000 solar masses of cooled gas should accumulate per year in a cooling cluster [32]. This value has not been observed in standard cool core clusters. This implies that there should be a mechanism that offsets cooling faster than the cooling time within the core of a cluster. As we see many clusters existing with a heated ICM beyond this 1 Gyr benchmark, and cooling rates are not as high as classical models imply, there has to be a heating process beyond standard thermal conduction. Another possibility is that our current models of radiative cooling are incorrect.

One of the key components that may cause reheating in the cluster is caused by its active black hole and relativistic jets. As the cooled down gas compresses around the core of cluster it also compresses around the BCG. With an increase in gas entering the region around the AGN this causes an excess of gas to accrete onto the central black hole. Some of this gas may pile up into an accretion disk around the black hole. While black holes do glow from their accretion disks, the emission that truly impacts the structure of a galaxy cluster is in the form of large relativistic radio jets. These jets emitted from the AGN output energy into the surrounding environment in the order of 10^{53} erg/ M_{\odot} [120]. The process of a black hole emitting relativistic jets and its underlying mechanisms is still poorly understood. One theory is suggested by the Blandford–Znajek process, wherein a Kerr black hole may cause the magnetic field formed by the plasma within its accretion disk to twist. This action of twisting magnetic fields allows for the system to convert rotational energy around the black hole into large relativistic jets [8, 105]. These jets do not have to follow the plane of the galaxy that houses the AGN, and rather they follow the poles of the black hole. Beyond the initial emission sometimes jets appear to bend, they do this under the influence of their environment, some causes are: galactic winds, and bulk motion. Either way the particles found within a relativistic jet coil around a magnetic field line and with each gyration around the magnetic field line the relativistic particle (electron) experiences magnetobremssstrahlung [39]. As the particle coils it emits radiation to account for the acceleration it experiences.

Synchrotron radiation emitted from the relativistic jets dominate the radio band. This causes the jets themselves to be invisible to X-ray telescopes such as XRISM and CHANDRA. Yet the effect the jet has on the surrounding ICM is crucial, as it pushes out the gas surrounding it, creating a shock front appearing from the core of the ICM. When observing this through an X-ray telescope the regions where the radio emission seems to end show a large void in the ICM, as the pressure of the jet pushes away the gas. This action may be the driving force that breaks self similarity in active cool core galaxy clusters. As this

pressure pushes on the gas one can discern that the jet has pushed cool gas from the center out into the warmer outer regions of cluster.

In a well documented cluster, MS0735.6+7421, these jets were seen to fire out to 50-90 kpc. The jets themselves were still within the predicted metal enriched core, but then they appear to become diffuse and expand into lobes 200kpc across [70]. The fact that this portion of the jet clearly passes the cool core threshold (beyond 100-150kpc) it means that the cooled gas from the core has successfully reached a warmer environment. The surrounding gas lifted by the jet will then be heated through thermal conduction.

Jets then heat through work, pushing low entropy plasma up into higher entropy regions of a cluster, and they also inject their own energy into the surrounding environment creating a shock front. This shock front is important, as it forms a circular shape with a lower density of X-ray emitting plasma, these are called cavities or bubbles due to their shape and buoyant nature. Cavities tend to be stand out X-ray features within a galaxy cluster and form in most cool core clusters. It is mainly seen in cool core clusters as the luminosity of the cavities drops to 40% below the surrounding ICM, this would not be easily identifiable in non-cool core clusters as they are too dim [30, 71]. The amount of energy within each cavity is equivalent to the energy of the radio lobe plus the work required to inflate the cavity against the pressure of the surrounding ICM. This means that the energy requirement to produce this cavity is equivalent to its enthalpy [106]. Enthalpy, by definition, is a combination of an object's internal energy and the work that it needs to push out its surroundings under a constant pressure. This simplifies into an equation which finds the overall energy to produce a cavity with a set volume.

$$E_{\text{cavity}} = H = E_{\text{jet}} + pV \quad (1.3)$$

$$E_{\text{jet}} = \frac{1}{\gamma - 1} pV \quad [71] \quad (1.4)$$

Within the Eq 1.3 and 1.4 p is defined as the pressure of the ICM, V is the volume of the inflated cavity and finally γ is the adiabatic index. Understanding the adiabatic index of a radio lobe simplifies this calculation. Usually the radio lobes inflating the cavities are considered to be dominated by relativistic particles, especially since the lobes emit synchrotron radiation, meaning that the adiabatic index is equivalent to $\frac{4}{3}$ [7]. This is the standard for initial cavity production. There also is an adiabatic index for generating a cavity with non-relativistic gas, this is equivalent to $\frac{5}{3}$ [106]. This comes from the assumption that the ICM is comprised of monoatomic gas, where the particle only has 3 degrees of freedom [22]. Putting these values into Eq. 1.4 equates to $4pV$ for a relativistic gas and $2.5pV$ for a non-relativistic gas. A third case exists in which cavities are dominated

by magnetic fields instead of relativistic and non-relativistic particles, in this case the enthalpy of the radio lobe is equivalent to $2pV$ [71]. As they are under the influence of multiple factors the enthalpy of relativistic gas driven lobes is used as the upper bound while the enthalpy of the magnetic field driven lobes is used as the lower bound. The true enthalpy of the radio lobe will usually be found between these two values. Papers on simulating cavity production usually discuss the upper limit of a radio lobe's enthalpy [116]. With this value the power of a cavity may be defined. This is done by comparing this calculated enthalpy of the cavity and the overall age of the cavity.

$$P_{\text{cavity}} = \frac{E_{\text{cavity}}}{t_{\text{cavity}}}. \quad (1.5)$$

AGN jets are not instantaneous events. After the initial outburst a jet may continue to inject energy into the surrounding ICM for over thousands of years. This means that the ICM is continuously being reheated with an ever expanding cavity at the end of this jet. This explains how MS0735.6+7421 has produced a pair of cavities with a radius of at least 200kpc [70]. To find the actual energy output of the AGN we use an equation relating its luminosity to the mass accreted by the AGN:

$$L = \epsilon_r \dot{M}_{\text{acc}} c^2 = 5.7 \times 10^{45} \left(\frac{\epsilon_r}{0.1} \right) \left(\frac{\dot{M}_{\text{acc}}}{M_\odot} \text{ year}^{-1} \right) \frac{\text{ergs}}{\text{s}} [109]. \quad (1.6)$$

Here ϵ_r is defined as the radiative efficiency, a value relating to the accretion rate of the black hole and the type of accretion disks that may form. This value will be equivalent to $\leq 10^{-3}$ if either it has a low or high accretion rate. If the accretion disk is cold, optically thick but geometrically thin then this value is dependent of the black hole's spin, with ϵ_r being usually around 0.05 to 0.2 [59, 109]. The luminosity and output energy is then defined by the mass accretion rates and the rotation speed of the Kerr black hole. The AGN can be characterized by two different modes of feedback: quasar mode, occurring only if the AGN is considered radiatively efficient and radio mode, where the AGN is considered radiatively inefficient and emits large radio jets [109]. This thesis will only focus on the radio mode, its energy injection rate is defined below:

$$\dot{E}_k = \epsilon_{f,k} \dot{M}_{\text{acc}} c^2 = 5.7 \times 10^{46} \epsilon_{f,k} \left(\frac{\dot{M}_{\text{acc}}}{M_\odot} \text{ year}^{-1} \right) \frac{\text{ergs}}{\text{s}}. \quad (1.7)$$

Here $\epsilon_{f,k}$ is defined by the efficiency of the kinetic energy coupling driving the outflow around the ICM. Recent simulations show that this value may range from 10^{-3} up to 0.08

depending on rotation speeds [51, 119, 118]. Since some jets last more than 1 Myr the total injected energy provided by them is immense. As Carilli (2002) states, the cluster PKS 1138-262 has a pair of jets that have been injecting their power into the surrounding ICM for 2×10^7 years, at a rate of $5 \times 10^{46} \frac{\text{ergs}}{\text{s}}$ [13, 120]. This implies that the total energy the jet's have emitted into the surrounding ICM (assuming an accretion rate of $1 M_\odot$ per year) would be a total of $\epsilon_{f,k} \times 3.154 \times 10^{61}$ ergs. These large energy pumps then inflate a pair of cavities in the surrounding ICM to start the heating cycle again.

Paradoxically this high energy process that fires off the cold diffuse gas around the central BCG helps in keeping clusters heated since it lifts the cold gas and injects it into the warmer regions of the cluster.

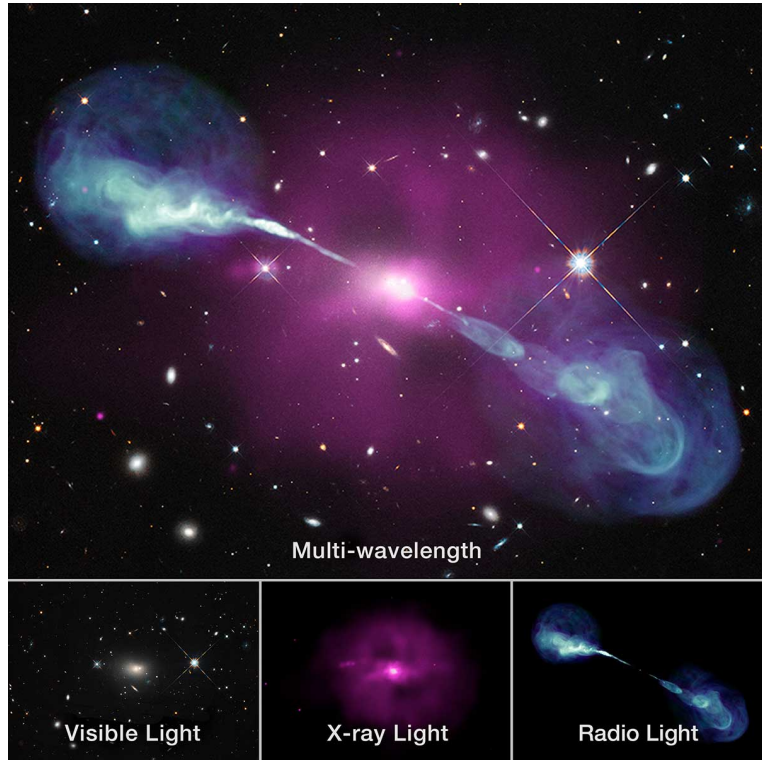


Figure 1.2: HerculesA multi-wavelength image with bright radio jets. The optical wavelength data is provided by the STScI, X-ray produced by Chandra, and Radio produced by the NRAO VLA

1.5 Cavities

Cavities, sometimes called bubbles, are visually striking features of low density X-ray gas located within cool core clusters. They are produced by the sudden introduction of a high powered jets into its convectively stable environment. Through continued injection the jet produces an expanding elliptical region of lower density plasma, with a higher density shock front enveloping the edges of the cavity. This shock front contains a mix of cool gas from the core of the cluster and the gas in the surrounding environment. Since this is essentially a low density gas enveloped by a higher density “surface” surrounded by an environment with a density gradient the cavity acts like a buoyant bubble. This means that the cavity will move up in the gravitational well due to the pressure of the ICM. This may decouple the cavity from the AGN jet, allowing it to “float” further than the jet’s influence may go. Many cavities appear to be formed from older jets and still continue to rise well after they stopped firing. This decoupling allows for multiple cavity pairs to be found in clusters, HydraA, for example, has at least 6 cavities that heavily influence the motions of the ICM around them. Understanding the motions of cavities is key to understanding the velocity structure and the dispersion of metals within the ICM.

Like a standard bubble a cavity is not a stable object within the cluster, it is prone to a multitude of instabilities. For instance ram pressure, a pressure exerted on a body moving through a fluid, can start stripping off the front shock of the cavity as it permeates through the cluster.

$$P_r = \rho_e \nu^2 [43]. \quad (1.8)$$

In the equation for ram pressure, ρ_e is defined as the density of the environment, which in this case is the density of the ICM, while ν is defined as the velocity of the cavity. When cavities are initially inflated they appear to be spherical but ram pressure can cause them to deform. As the environment exerts its pressure onto the moving cavity it causes the cavity to flatten with the wider axis of the ellipse being perpendicular to its motion [11]. Ram pressure can furthermore deform this by forcing the cavity into a fabiform as the material on the front shock must slide to the edges of the cavity, increasing the pressure on the edges. This ram pressure acts essentially as a drag force against the cavity, but depending on the strength it may strip away at its weak shock shell. If this outer layer is stripped away the cavity “pops” as the environmental inflow fills the low density region. This implies that cavities may be prone to fluid instabilities such as the Rayleigh–Taylor instability and the Kelvin–Helmholtz instability. Each of these act on different regions in the cavity and influence the wake of the cavity’s path after being pushed out by the AGN jets.

Importantly for Rayleigh–Taylor instabilities the cavity can be considered a fluid that is flowing into a higher density fluid, the ICM, working against gravitational potential. Any form of perturbation on the interface between the two fluids causes the denser fluid (the ICM) to attempt to pierce through the lighter fluid (the cavity) [56]. As this occurs the lighter fluid is then displaced upwards into the denser fluid. This creates “finger-like” protrusions as surface perturbations occur on several points. These protrusions form into plumes, creating “mushroom caps” if the perturbation continues to grow [16]. As the instabilities increase and further penetrate through the initial fluid interface, the cavity’s ability to hold shape and push against the surrounding pressure fails, leading to the cavity “popping”. The Rayleigh–Taylor instability only acts on the face of the cavity leading out of the gravitational well.

The Kelvin–Helmholtz instability occurs when there is an interface between two fluids moving at different velocities. Since cavities are buoyantly rising up through the ICM, both fluid-like components are then moving at different velocities, successfully passing the criteria for this instability to be observed [56]. As the interface between the sides of the cavity and ICM experience a velocity shear it creates perturbations on the cavity edges and uplifted gas following in the wake of the cavity. This process creates downstream vortices (eddies) in the wake of the cavity which drags up gas behind the cavity faster than the motion of the cavity itself [121]. This provides another mechanical function to pull cold gas out from the cool core to the warmer regions of the cluster, further improving the efficiency of the jet heating in clusters. These vortices are important features to note when observing the turbulence of the ICM behind cavities.

Simulations made by C. Zhang et al (2022) showcase this formation of small Kelvin–Helmholtz eddies within the wake of the cavity [121]. These eddies are defined by the darker particles in the wake in Fig 1.3, pulling up gas from the core. There seems to be larger pair of eddies forming at 30 kpc at 0.5 Gyr, creating an unstable region that turns in on itself. This forms a backflow into the core of a cluster, injecting warmer gas from the surrounding regions of the coiled up eddies back into the cooler center [93]. These backflows allow for a new form of core heating where parcels of warmer ICM are injected into cooler regions, further churning the innermost regions of a cluster. This can explain the stark difference in the ICM between the churned and relaxed regions in the core of the cluster. This feature of simple backflows has been simulated and showcased in magneto-hydrodynamics prior to this, but simulations of reverse jets are new to the field [73].

This means that a cavity should experience R-T instabilities on the side furthest from the cluster’s core and it should experience K-H instabilities on its sides that are parallel to its motion. These concurrent effects would imply that cavities are short lived structures, yet they have existed well beyond the timescale in which instabilities would have completely

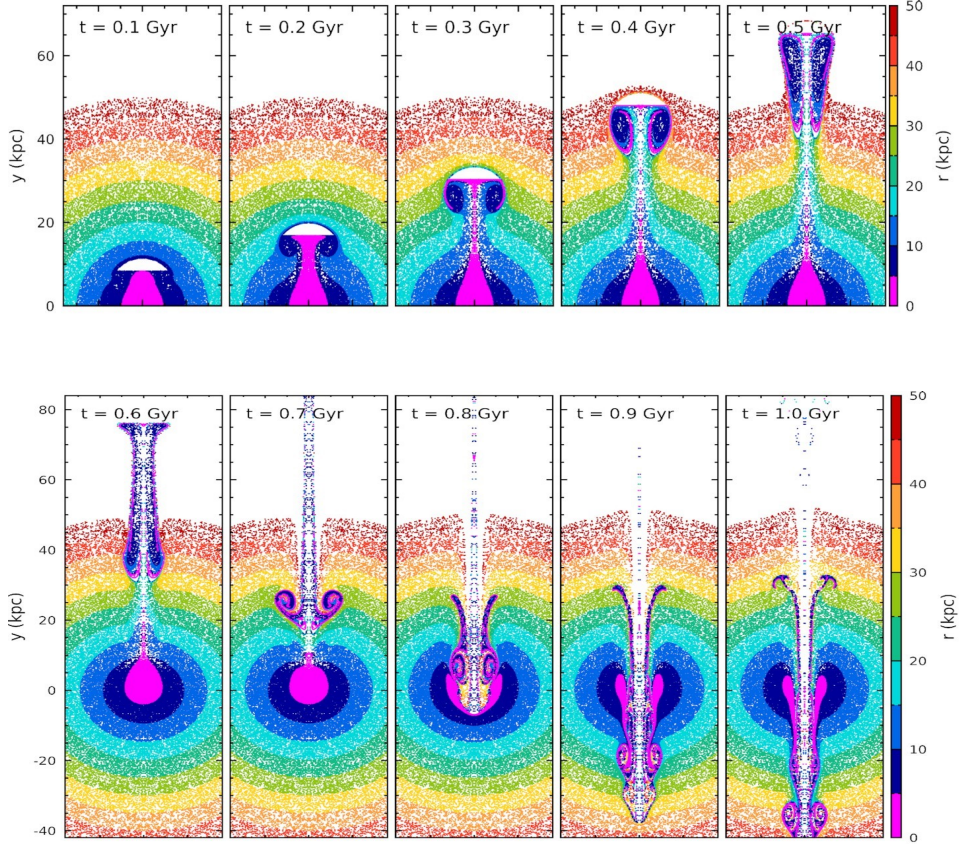


Figure 1.3: Simulation of a Cavity pulling up gas from BCG, the particles are colour coded by their original location to showcase uplift - [121]

shred them [26]. This suggests that there is at least one component in cavities that makes them stable, or at least heavily resists these instabilities.

The equations for the growth time of both Rayleigh–Taylor and Kelvin-Helholtz instabilities are shown below:

$$t_{\text{KH}} = \frac{\lambda_h}{\Delta\nu} \frac{(\rho_L + \rho_H)^2}{\rho_L \rho_H}, \quad (1.9)$$

$$t_{\text{RT}} = \sqrt{\left(\frac{\lambda_h}{2\pi A|g|} \right)} \quad [26]. \quad (1.10)$$

Within each equation λ_h is defined as the size scale of the instability, A is the Atwood number (a value defining the shape of the R-T instability), $\Delta\nu$ is the velocity difference between the cavity and the bulk motion, ρ_L is the density of the cavity, ρ_H is the density of the environment, and g is gravitational acceleration. These timescales offer values in which certain cavities cannot exist for more than 5 Myr in some clusters, well below their estimated ages. A quick calculation for the age of a cavity may use this equation:

$$t_{\text{cavity}} = \frac{R}{\nu_{\text{term}}} . \quad (1.11)$$

R is defined as the radius from the center of the cavity, and ν_{term} is defined as the terminal velocity of the cavity. With instability values under this timescale this means that there must be a component in cavities that resists both forms of instabilities [26]. The current prevailing theories for resistances to both Kelvin–Helmholtz and Rayleigh–Taylor instabilities are: cavity expansion [89], magnetic field lines [66], and viscosity [45, 93, 96].

1.5.1 Cavities: Resisting Instabilities

There are three standing theories that exist to offset the cavity instability timescale tension, cavity expansion, tangled magnetic fields and gas viscosity. Each of these is being explored as both the sole solution to offset the instabilities and in conjunction with the other solutions.

The calculation for a cavity's age under constant Rayleigh–Taylor instabilities would never allow it to decouple from the radio jets. It has been theorized that the mechanical action of inflation on a cavity is strong enough to dampen the effect of Rayleigh–Taylor instabilities [60]. One of the main proponents of this theory is that inflation creates a drag effect on the growth rate of the Rayleigh–Taylor instabilities, a coefficient akin to Hubble drag dampening the perturbations in the Universe's expansion [89]. The Rayleigh–Taylor instability has an e-folding time (the time in which the R-T instability grows by a factor of e) that is inversely proportional to the force of gravity acting upon the cavity. This expansion component acts against the direction of the gravity, lowering its overall acceleration and increasing the e-folding time of the R-T instability [89]. The location in which the cavity is produced can also effect its lifetime, as the initial cavity radius is inversely proportional to the density of the surrounding ICM, higher densities cause the Atwood number of a cavity to increase [27]. The Atwood number is a relation between densities of fluids, a larger number denotes stronger R-T instabilities. Since the e-folding time is inversely proportional to the Atwood number then cavities formed close to the center

of the cluster will be more susceptible to the Rayleigh–Taylor instability. If the cavity was expanded through inflation then the edge furthest from the core would increase its e-folding time as the Atwood number decreases in lower density regions. As inflation is not indefinite for these cavities, since jets single-handily power this expansion, cavities will still succumb to R-T instability just over a longer timescale. Cavity inflation only weakens Rayleigh–Taylor instabilities, they do not change the timescales of Kelvin–Helmholtz instabilities.

Tangled magnetic fields may be produced in cavities by AGN jets, since the AGN creates synchrotron radiation through the Blandford–Znajek process [61, 80]. Magnetic field lines may be the secret to offset both the Rayleigh–Taylor and Kelvin–Helmholtz instabilities as long as they are parallel to the surface of the cavity and the environment [14]. Testing multiple simulations by injecting a cavity into an environment with weak magnetic fields shows that R-T and K-H instabilities take over quickly. In simulations where the magnetic fields are strong enough (over $1 \mu\text{G}$) the instabilities are significantly quenched [55, 73]. Magnetic fields within cavities are theorized to align along the cavity surface allowing it to further bolster its strength against instabilities. If the field lines of the ICM are parallel to the cavity’s motion it will only constrain the expansion of the sides of the cavity. If the field lines are perpendicular to the motion of the cavity it will increase the e-folding time of both R-T and K-H instabilities in addition to constraining expansion. Simulations from Diehl et al (2008) suggest that observed cavities are similar to bubbles that were produced by an inflation of a chaotic bundle of magnetic field lines [26]. These simulations suggest that inflation without field lines would have to be continuous for most cavities to exist in the timescales that have already been observed.

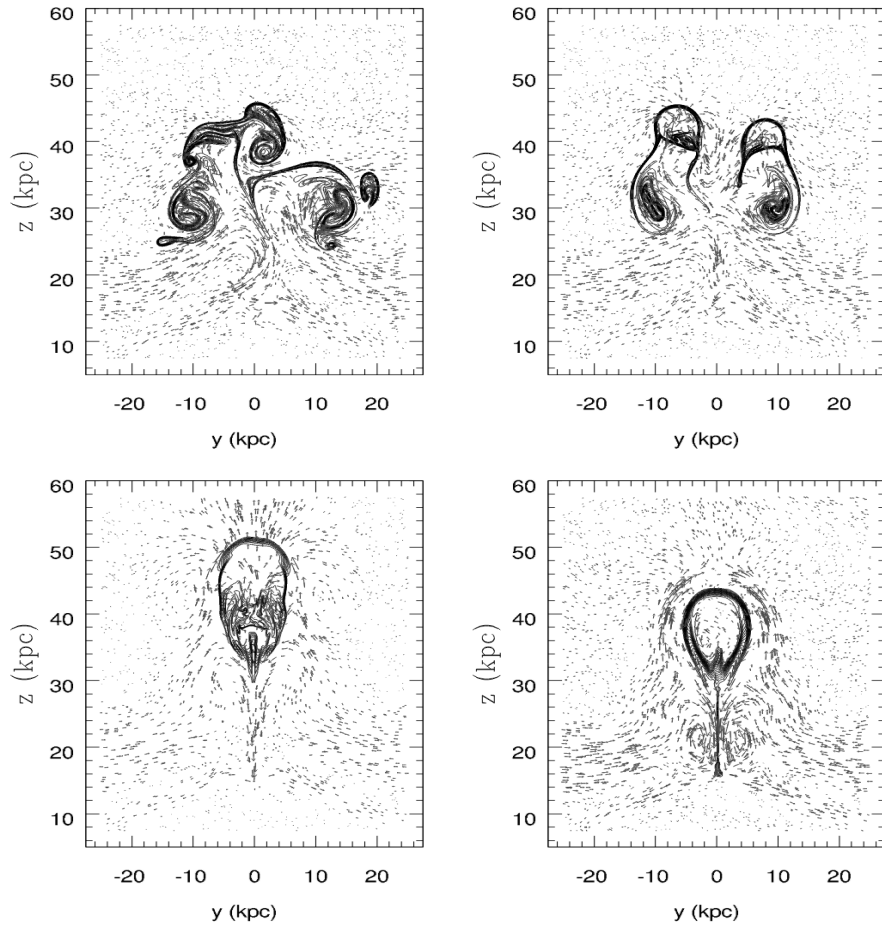


Figure 1.4: Velocity vectors of 4 cavities in different ICM fields after 150 Myr (**Top-L**): ICM field strength: $0.2 \mu\text{G}$, cavity field strength: $2 \mu\text{G}$. (**Top-R**): ICM field strength: $1 \mu\text{G}$, cavity field strength: $10 \mu\text{G}$. (**Bottom-L**): ICM field strength: $5 \mu\text{G}$, cavity field strength: $50 \mu\text{G}$. (**Bottom-R**): ICM field strength: $5 \mu\text{G}$, cavity field strength: $50 \mu\text{G}$, reversed field - [55]

Viscosity is considered a separate method of lowering the effects of both the Rayleigh–Taylor and Kelvin–Helmholtz instabilities. It is a component that only comes into effect in the late stages of a cavity, which is the predicted time in which some cavities should “pop”. Observations of simulations focus on the shape of the cavity that is produced. Simulations were run with and without a viscosity component, and every single run without viscosity had the cavity devolve into a “torus-like” object. Simulations with a constant viscosity

component caused cavities to continue to be spherical [44]. Different viscosities between cavities were tested by altering the Reynolds number of the simulation. A Reynolds number is the ratio between viscosity and inertial forces, with a low Reynolds number defining as a highly viscous system reaching to a laminar flow, while high Reynolds numbers give highly turbulent systems. The equations for viscosity in a plasma and the Reynolds number are shown below:

$$\mu = 7.3 \times 10^{-17} \sqrt{T^5} \frac{g}{cm \ s}, \quad (1.12)$$

$$Re = \frac{\nu L \rho}{\mu}. \quad (1.13)$$

μ is defined as the viscosity of the cavity/plasma, the standard range that was tested in C.S Reynolds' (2005) [93] simulations had a magnitude of 10^{-3} - 10^{-2} , ν is defined as the velocity of the cavity, L is defined as the size of the cavity and ρ is the density of the surrounding ICM. This viscosity can also explain the torus like structures of H α located just behind certain cavities, such as the one found in the Perseus cluster [31]. Viscous dissipation can also be used as a method to carry energy throughout the cluster in longer timescales, providing another source of heating. The slow heating and cooling of a viscous fluid may also explain why a cool envelope of the ICM surrounds cavities [93].

Simulations of all three components working in tandem have currently not been shown, but each component provides promising explanations as to why we see cavities exist well beyond the expected timescales. Theoretically if all components act consecutively on a cavity there would be 3 stages to the life cycle of a cavity offsetting instabilities: an inflation mode for early cavities, a magnetic field mode as a constant throughout, and a viscous mode for late stage cavities. This suggests that cavities are actually stable structures that drag cool gas into heated environments through multiple mechanical methods.

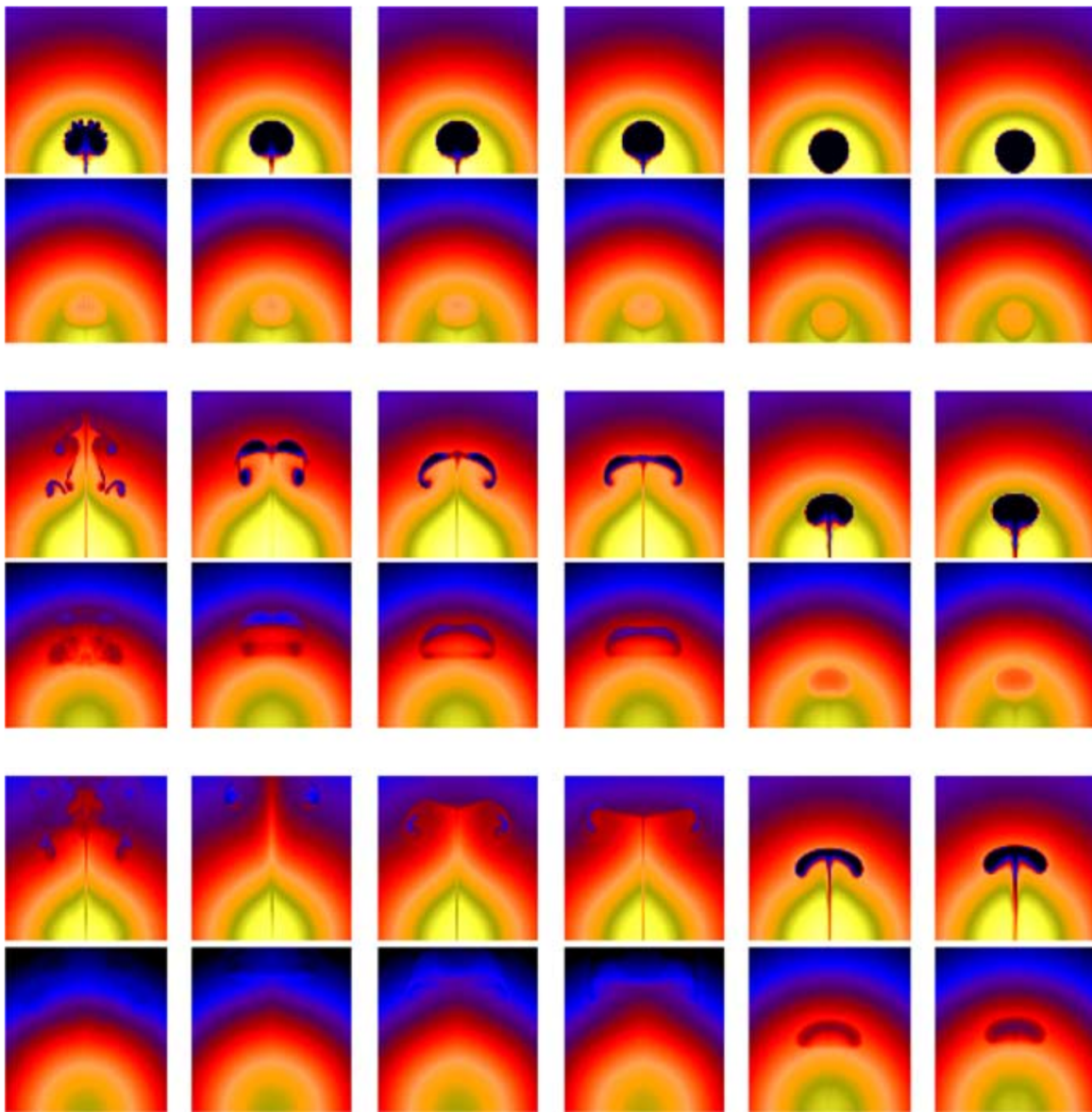


Figure 1.5: Effects of Viscosity on Generating Cavities - Simulations of multiple viscosities done by C.S Reynolds (2005), the images are sets of 2 with density maps (upper) and X-ray luminosity maps (lower), the x-axis is increasing in viscosity and the y-axis is decreasing in time [93]. Thus the late stage, least viscous simulation is in the bottom left.

1.5.2 Cavities: Uplift

The efficiency of the heat pump created by the motions of cavities is key to understand the longevity of galaxy clusters. It is important to calculate the movement or uplift of gas from the core of the galaxy cluster and observe the locations where this gas is deposited. A cavity will carry gas up through its shock front as it buoyantly rises through the cluster while also pulling up gas through its trailing outflows. These outflows will deposit some gas along the wake providing linear filament structures behind each cavity [28]. These two processes mechanically lift metal rich packets of gas within the cluster to distant metal-poor regions, this means that the total metallicity of galaxy cluster increases due to metal enrichment from the cooled out core. If there is a consistent radius in which cavities deposit most this cooled out gas then there should be a peak in metallicity not directly at the core of the cluster. A turnover does occur within several clusters shown in the datasheets in the appendix, the known clusters that show this peak in metallicity are: A426, A2199, AWM7, Centaurus, HydraA and Ophiuchus. Other sources such as M. Gendron-Marsolais (2017) have found this drop and peak feature to exist in different clusters [36]. In NGC 4472 that the metallicity drops at 6 kpc away from the core, and flattens out at a peak in between 8-20 kpc from the core. The decrease of metallicity in the core may be an effect of dust combination with cooled out ions, thus the metallicity turnover is not necessarily from cavities removing and depositing cooled gas in the same region.

While metallicities may be difficult to define where in the cluster the metal originates from, a simulation of how far gas gets displaced from the core by a cavity may be studied. These simulations can extract information on the energy efficiency a single cavity, as this is the process where energy is used to transport and (re-)heat gas. If this process is found to be energy inefficient galaxy clusters will cool down over time and will not be able to perpetually reheat themselves through thermal conduction. Y-H Chen (2019) created a simulation where each particle can be traced back to their starting position to observe the overall displacement per particle [15]. Within the simulation it is shown that around 15% of the gas within the inner 10 kpc of the cluster ends up being lifted and deposited more than 20 kpc away while the upper layers of gas in the cluster cause an inflow. This inflow injects heated gas from the outer regions in the ICM into the core as well. The inflow appears as a negative radius to the initial distance of the particle in Fig 1.6.

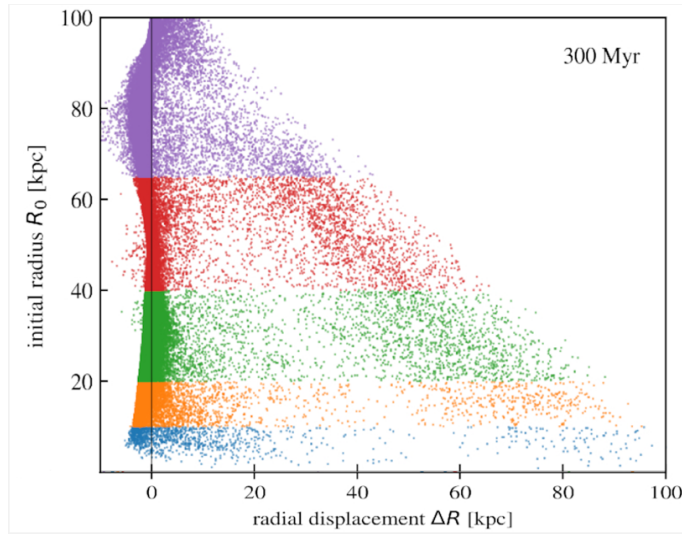


Figure 1.6: A simulation of a cavity being produced and buoyantly rising through the ICM for 300 Myr, this showcases the displacement of gas at certain radii while interacting with a cavity - Image produced by Y-H Chen (2019) [15]

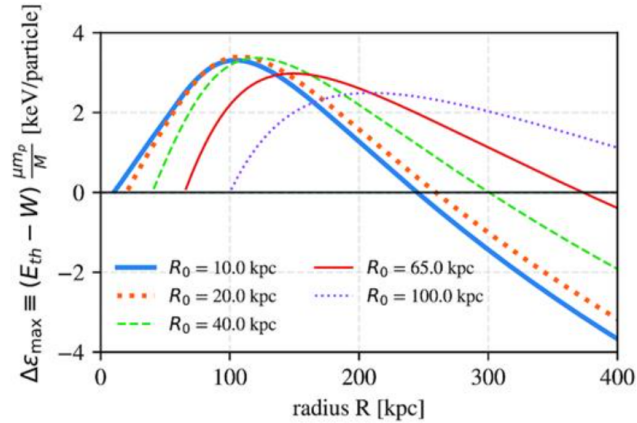


Figure 1.7: A simulation of a cavity being produced and buoyantly rising through the ICM for 300 Myr, this showcases the thermal energy budget for each particle's initial location and where they have been lifted to - Image produced by Y-H Chen (2019) [15]

The findings in Y-H Chen's (2019) paper define that the process of lifting gas by a cavity acts almost exactly like a geothermal heat pump, wherein a heated fluid enters the core and cooled fluid gets pushed up to the outer edges of the cluster to be reheated [15]. Unlike an actual geothermal heat pump there is no work expended lifting the cooled particles up against gravity due to buoyancy. Thus particles are lifted up with no work and gain energy by being placed into a heated environment, meaning the efficiency of this simulation (quantified as potential thermal energy gain over work done to the particle) is $>100\%$ [15]. This simulation shows another important aspect to energy gain within clusters, the temperature raises to a peak just outside of the core of a galaxy cluster and has decreasing heat gradient. If the gas is pushed out into the cooler diffuse regions it will have a negative thermal energy budget, as it emits heat into the cooler environment. This simulation shows the strength and energy efficiency of cavity uplift. This is the answer to the cooling catastrophe that was predicted initially by galaxy clusters, as the heat is recycled through an efficient geothermal heat pump-like process offsetting the cooling produced by thermal radiation. Through this cavities deposit metal rich parcels of gas into metal poor regions at specific radii, this deposit location is dependent on the initial radial position of the gas. To observe the increase in metals around cavities, and to find the regions where they should be deposited, high spectral and angular resolution X-ray telescopes are required. While CHANDRA can be used to observe annular radii around the cluster its spectral resolution is somewhat poor, XRISM has the opposite issue wherein the angular resolution is poor but the spectral resolution is cutting edge. This points towards future missions like ATHENA being required for a deeper look into this field.

1.6 X-Ray Spectral Components

An X-ray spectrum from a galaxy cluster's ICM contains multiple convolved components, the main structural component comes from the bremsstrahlung continuum. The bremsstrahlung continuum creates the overarching shape of the spectrum as it emits free-free radiation from a slew of different cross-sections. The shape of the spectrum follows the emissivity of thermal bremsstrahlung as it tapers off at higher energies, but there is filtering extinction caused by the instrument containing materials that block off low energy X-rays. The X-ray continuum cannot just be bremsstrahlung emission, there are photons that appear beyond the limit of maximum photoenergy and there are spikes within the continuum that are not produced by bremsstrahlung photons.

The spikes of photon counts can be attributed to characteristic X-ray emission lines. These photons are emitted when electrons transition from outer shells of an atom into vacant inner shells [77]. These characteristic emission lines are broadened through several factors, such as natural line width, collisional broadening, instrumental broadening and Doppler broadening. Natural line width occurs due to the Heisenberg uncertainty principle, as the decay of an electron to another state is not spontaneous causing the emission of the photon to have an uncertainty on the energy. The natural line width is a Lorentzian shape around the absolute energy [40]. Collisional broadening occurs due to interactions between these photon emitting atoms. A gas at a high pressure can cause the two atoms to interact and may add or remove energy into the electron. This process can increase or decrease the lifetime of that electron's excited state [5]. Either of these interactions will cause broadening in this line in a 4-component Gaussian profile [88]. Instrumental broadening is related to the spectral resolution of the instrument, and may shift the energy across its bin in a Gaussian profile. Doppler broadening, the last main type of broadening, occurs while observing particles in a moving gas, as the motion of particles may cause some to be slightly blue-shifted while others may be redshifted. This produces a Gaussian profile around the characteristic X-ray energy value. Doppler broadening can be separated into two components, thermal broadening and turbulent broadening. The thermal broadening FWHM may be calculated by finding the temperature of the cluster. The thermal component can be subtracted from the Doppler Gaussian to find the turbulent speeds. Finally, bulk motions do not appear to influence the broadening of these lines, rather they shift the line centers, causing the cluster to appear to be at a slightly different redshift.

There has to be another form of emission that is causing photons to appear beyond the maximum photoenergy limit. The cause of these extra photons is through another component of thermal bremsstrahlung named recombination radiation. Recombination radiation is a free-bound interaction with an ion and an electron [108]. This interaction occurs when a free electron passes by an ion and gets captured in an outer shell. The ion outputs a quanta of radiation equivalent to the difference between the excited shell energy and the free electron energy. This creates “recombination lines” where there are specific edges in the spectra correlating to the different excited states an electron may be captured in [81]. The width of recombination lines relate to the overall energy range of the interacting electron, as they may have undergone free-free bremsstrahlung prior to this interaction. This appears as a step-like effect on the overall continuum.

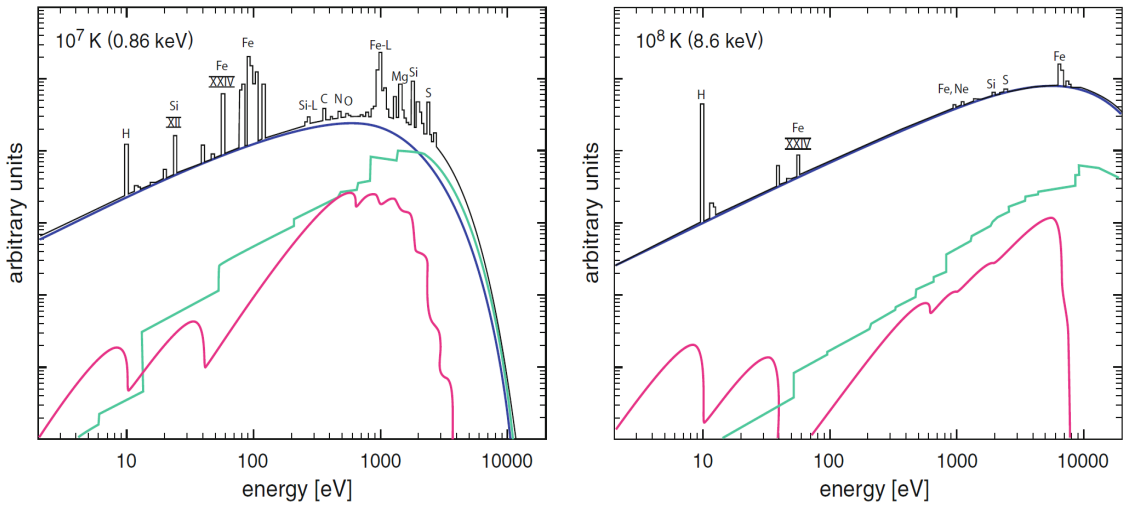


Figure 1.8: Two simulated spectra from clusters that have different temperatures. The blue line represents bremsstrahlung emission, the green line represents recombination radiation and the red line represents two photon emission. Bremsstrahlung is clearly the dominating emission, but recombination radiation has an effect on the upper energy values - [101]

There is another component shown in Fig 1.8 named two-photon emission. Two-photon emission is a process where an atom must completely undergo its multi-photon cascade to reach a relaxed state. All excited electrons must transition to the lowest unoccupied shells, emitting radiation on each transition, until it reaches the 2s shell. Upon entering the 2s shell with a vacancy in the 1s shell the electron may attempt to drop even further [17, 103]. The law of conservation of angular momentum prohibits this process as both 1s and 2s shells have a spin of 0, while a photon being emitted will have a spin of 1, thus the emission of a single photon to go to the next stable shell will fail to occur. Normally the process of going from 2s to 1s requires an absorption of energy to go up to 2p and then the electron will output a photon to reach the 1s shell. Galaxy cluster gas is so sparse that the atom will not have the capability of exciting its electron over an extended amount of time [17]. The electron then has to drop states with no added energy, this is done through a process that conserves angular momentum, the production of a virtual state. A virtual state allows for forbidden transitions to occur as it is a short lived quantum state. The electron drops into the virtual state, emits a photon with angular momentum, and quickly drops again to the final state producing a second photon with opposing angular momentum. The production of two photons allows for angular momentum to be conserved through this forbidden transition, outputting a pair of photons with similar (but not the same) wavelengths. This appears as pairs of rounded features on the spectral continuum, yet in the temperature ranges of galaxy clusters the other components dominate in relation to this one. This makes the two-photon effect is difficult to spot in comparison to the rest [101].

These four components all add up to a single spectrum observed by CCD imaging in X-ray telescopes. Each of these can provide robust values for temperature, redshift, velocity and metallicities, with the most important component being in the X-ray characteristic emission lines. This thesis will focus mostly on emission lines produced by both real low spectral resolution data and simulated high spectral resolution data. Through these observations velocities, redshift and metallicity can be calculated by modelling characteristic lines, while temperature can be obtained from the continuum.

Chapter 2

CHANDRA: Low Spectral Resolution Radial Metallicities

Understanding the physical differences between cool core and non-cool core clusters requires using a high spatial resolution X-ray dataset to differentiate regions within a cluster. Currently the most useful X-ray telescope for this is CHANDRA, a high spatial resolution low spectral resolution instrument, as it contains the largest database of cluster spectra available to the public. Using CHANDRA imaging, multiple radial metallicity curves, radial temperature curves and cooling time curves can be made for several well known clusters. Other components may be pulled from these images as well such as overall luminosity and photon counts from the Iron-K complex. This may glean important features in clusters, such as observing the metallicity of outer cluster regions, as it may leave hints to early cluster enrichment scenarios. Therefore within this chapter I reformat these images into datasheets that contain the radial curves for comparisons between clusters. I also extract spectra and create datasheets for regions with the same angular size as XRISM's Resolve instrument to create baselines for future data expected from XRISM.

This chapter includes original research, using data from the publicly available CHANDRA X-Ray Observatory database, it also includes mass data produced by Mike Hogan to normalize the radii. All the X-ray data within this chapter was analyzed and produced by Neo Dizdar unless stated otherwise.

2.1 CHANDRA

CHANDRA is an X-ray telescope that was deployed in 1999, with its design being focused on observing high energy X-ray data from clusters and other X-ray sources. On the CHANDRA payload there are four scientific instruments: ACIS (the Advanced CCD Imaging Spectrometer), HRC (High Resolution Camera), HETG (High Energy Transmission Grating) and LETG (Low Energy Transmission Grating). ACIS is the scientific instrument that is used in this chapter, selected due to its spectral energy range over 0.2 - 10 keV and spectral resolution of 95 eV. This spectral resolution causes characteristic X-ray lines to blur into large Gaussians, covering many other weak lines and causing some metals to become unresolved. CHANDRA's ACIS can produce detailed images with an imaging resolution of 0.5 arcsec and a total field of view of 16.9 x 16.9 arcmin (Wide Field Mode) or 8.3 x 8.3 arcmin (High Resolution Mode) as each chip captures a 8.3 x 8.3 arcmin region in the sky [37].

CHANDRA's ACIS instrument comes with 10 CCDs in two configurations, ACIS-I and ACIS-S. ACIS-S appears as a straight line of 6 CCDs, classified as S0 - S5. Chips S1 and S3 are back-illuminated CCDs while the rest of the CCDs in both configurations are front illuminated [82]. The back illuminated chips have higher energy resolutions and observe low energy X-rays unlike the front illuminated chips. ACIS-I on the other hand is an offset set of four CCDs in a 2x2 square, it is offset from ACIS-S by 163 arcsec, each CCD is classified as I0-I3 [82]. ACIS-I does not have any back illuminated CCDs, thus imaging is at a slightly lower resolution. When the an exposure is taken of a cluster S3 and I3 are usually the CCD centered on the cluster, meanwhile S0 and S5 seem to be rarely used in any image. Most exposures contain six CCDs, these tend to contain four CCDs from one configuration and two CCDs from the other configuration. The two CCDs are used for background flare removal, filtering out non-ICM emission from the images allowing for clearer imaging.

Each CCD is separated by a small gap causing blank spots in the images. In the ACIS-S configuration the CCDs are offset by 9 arcseconds (18 pixels) while in the ACIS-I configuration the CCDs are offset by 11 arcseconds (22 pixels). To lower the effect of these blank spots appearing on the images multiple rounds of imaging with different roll angles (or different pointings) must be made. Images taken with the ACIS-I configuration are particularly affected by the CCD spacing, as the spacings are larger and that configuration usually is used for large angular size clusters. This creates a large dark cross in the most large non-cool core cluster images.

ACIS FLIGHT FOCAL PLANE

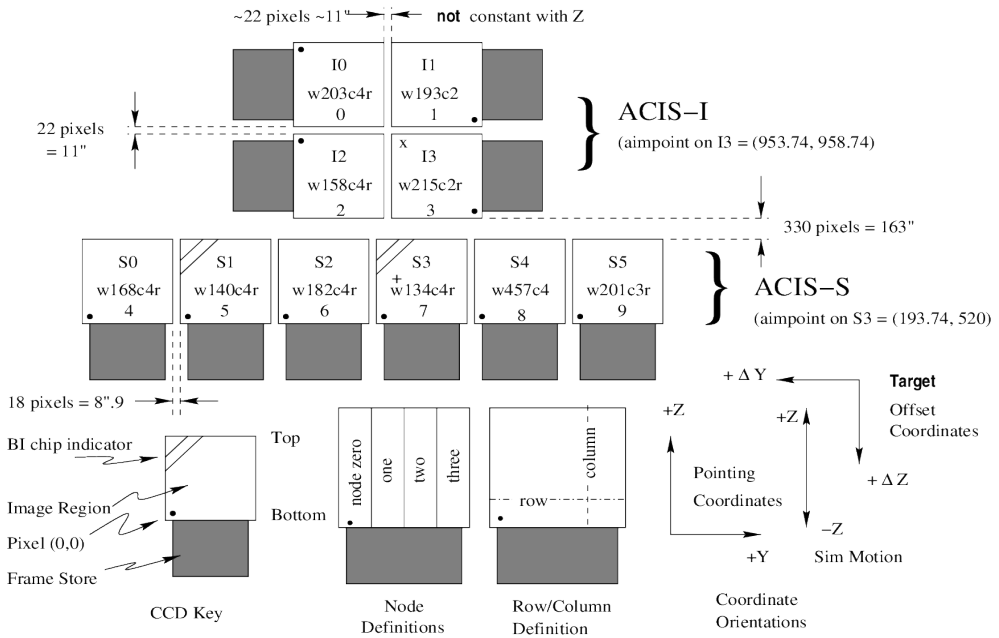


Figure 2.1: A diagram showing the format of CHANDRA's ACIS instrument

The CHANDRA X-Ray Observatory is a mission that has been used for 25 years, providing one of the most robust X-ray databases of different categories of cosmic objects. While CHANDRA has made many steps in the other categories, such as observing the first exoplanet outside of the Milky Way [25], measuring the Hubble Constant using the Sunyaev-Zel'dovich effect [10], and constraining the cross section of dark matter interaction by observing the Bullet cluster [67], it has been the cornerstone of X-ray studies in galaxy clusters. The database contains a large amount of ACIS images for many clusters with high image resolution and usable spectral resolution. This allows for large scale studies of temperature and metallicity profiles between different varieties of clusters. To access and use this data a tool provided by the mission was made: CIAO (CHANDRA Interactive Analysis of Observations) which requires the observation ID (or ObsID for short) to extract data from the database. It is suggested to use more than one observation for robust results, as it will increase the signal-to-noise ratio on each object.

2.1.1 Cluster ObsIDs

ObsIDs of Clusters used	
Cluster	ObsID
Abell 426	1513, 3209, 4289, 4946, 4947, 4949, 6145, 11713, 11714
Abell 478	1669, 6102
Abell 754	577, 10743
Abell 2029	891, 4977, 6101
Abell 2142	5005, 7692, 15186, 16564, 16565
Abell 2199	497, 498, 10748, 10803, 10804
Abell 2319	3231, 15187
Abell 3571	4203
Abell 3667	889, 5751, 5752, 5753, 6292, 6295, 6296, 7686
AWM7	908, 11717, 12016, 12017, 12018
Centaurus	504, 505, 4954, 4955, 5310, 16223, 16534, 16608, 16610
Coma	9714, 10672, 14406, 14411
CygnusA	6226, 6228, 6229, 6250, 6252
HydraA	576, 4969, 4970
MS0735	4197, 10468, 10470, 10471, 10822, 10918, 10922, 16275
Ophiuchus	3200, 16142, 16143, 16464, 16626, 16627, 16633, 16634, 16635, 16645

Table 2.1: The clusters shown are used to produce cluster datasheets, the ObsIDs given can be found in CHANDRA's database and is available for use by the public

The clusters were selected due to having multiple observations, being well known, or being a known non-cool core cluster. Unfortunately there are certain clusters that failed to load properly and had to be removed. This leads to some clusters (Abell 3571, Abell 2319 and Abell 754) having only one or two observations, causing a lower signal-to-noise ratio which increases the errors in photon counts. The errors propagate further to metallicity and temperature calculations as modelling these values is based solely on source photon counts over background counts. This creates a dataset of 16 known clusters, each of which will be output with their own datasheet that will contain information on the cluster. These datasheets are found in the appendix of the thesis.

2.2 Data Extraction

Data from CHANDRA is extracted through the use of CIAO tools, it is first taken as separate ObsIDs and reprojected to correlate a point to a singular point in the sky. This relates right ascension and declination to the image coordinates. Background subtraction is done by using blank-sky images, this has to be done when there is an extended object in the sky as it is difficult to disentangle the background and low luminosity ICM. The blank sky images account for vignetting and readout lines within the telescope. This full process is done with multiple ObsIDs to project each image with different roll angles onto the same position.

If done correctly this creates images with clear distinctions between the background noise and the extended object, but this also brings out the point sources in and around the galaxy cluster. Point sources like background stars and galaxies may pollute the spectral dataset and need to be removed for studies of the ICM. This can be adjusted with instruments that have high spatial resolution, like CHANDRA's ACIS, but will affect missions like XRISM as point sources become unresolved under Resolve's low spatial resolution CCDs. This means that for Chapter 3 this process must be repeated, this time allowing the presence of point sources. CHANDRA's tool for finding point sources (`wavdetect`) scans the image for Ricker wavelets, the Laplacian of a Gaussian function, and highlights these wavelets as point sources [111]. These Ricker wavelets are scaled by a point-spread function file attached to the image, widening the predicted point source regions. This function then generates a list of these regions with their luminosity values in each cell. While extracting a spectrum from the entire image these listed regions can then be removed allowing for studies of only the ICM.

To obtain radial profiles of a cluster the image must be subdivided into smaller regions. As gravitational potential wells create spherical objects, if a cluster is relaxed then they may be approximated to be spherical. With a spherical object the best way of obtaining a profile is to create concentric rings, or circular annuli, and extracting information from each ring. To dictate the size and location of each ring the center is defined to be on the BCG, defining the first inner ring. While a good approximation a BCG may be slightly offset from the true gravitational center of the cluster. The rest of the rings are produced by counting the amount of photons in a circular area outwards until a predetermined photon limit is reached, in this thesis each ring represents 3000 photons. This produces scaled bins of photon counts, but the physical size of the rings will change, with the smallest being near the BCG and the other rings being in the heated regions of the ICM. With the radius of the inner and outer edges of the ring stored each ring will have a separate spectrum extracted and attached with an average radius creating a radial profile of spectra.



Figure 2.2: This is an image of all of the ObsIDs of Abell 426 overlapped, the CCD gaps are very noticeable in this image due to it being taken at a log photon counts scale.

Each annulus contains its own dataset where spectra can be extracted from, turning pixel photon counts into a .pi file. This reads the input photon count data from a fits file and converts it to a graph comparing the specific energy channel and the amount of counts of photons in that energy channel bin per second. This process uses the known added exposure time of the pixel and divides the total photon count of an energy channel by this exposure time. The extracted spectral data is a histogram showing a distribution of photon energy in energy channels. These energy channels do not have a physical meaning and require a function to relate them to energy values rather than channels. This is done by creating an RMF (a response matrix file) and an ARF (an ancillary response file).

2.2.1 RMFs and ARFs

An RMF is a response matrix file it maps the photon's pulse height to the energy of a given detector. This process spreads photon counts over the resolution of the detector through using matrix multiplication. Each detector requires a different response matrix file and over time as a detector degrades these response matrices change. It is suggested that an rmf should be produced every time a new observation is made. Usually a response matrix will appear as a diagonal relationship relating energy channels and photon energy in a straight line, but this occurs only for high resolution instruments [21]. The CCD detectors on CHANDRA ACIS instrument do not have a perfect diagonal and are instead affected by escape peaks, and low energy tails. These two features change the matrix on specific energies, otherwise it is useful to assume a diagonal relationship between energy channels and keV [87].

An ARF is an ancillary response file, observing the effects of each pixel in the CCD and mapping the efficiency of the detector itself based off of the area of the chip. One of the basic features of an ARF is that it measures the effect of vignetting on the CCD, wherein the peripheral pixels on the CCD appear dimmer as less photons reach them. An ARF is the combination of the effective area of the instrument and the quantum efficiency of the instrument. The quantum efficiency is the fraction of incoming photons detected over the total amount of photons hitting the detector. While detectors strive to be 100% quantum efficient this has yet to be done [79]. ACIS's quantum efficiency is strong (near 100%) between 0.5 keV and 10 keV but drops significantly approaching energy values of 0.1 keV (below 10% at 0.1) [57].

Certain CCDs may have pixels that are failing, therefore they have to be removed and ignored as to not contaminate real data. Other CCDs may also have a chip turned off to use as a guide, as this chip can showcase the orientation of the telescope without needing a roll angle as a precursor. This requires updating the arf files with correct chip regions, as is chips/pixels are failing that drastically changes the instrument's effective area.

This implies that extracting spectra from any region needs to have an arf and an rmf produced to properly convert the spectra into keV. Pulling data from the annulus rings of the stacked CHANDRA ObsIDs requires an arf and rmf for each region and each different ObsID, these then are stacked into a summed rmf and arf file.

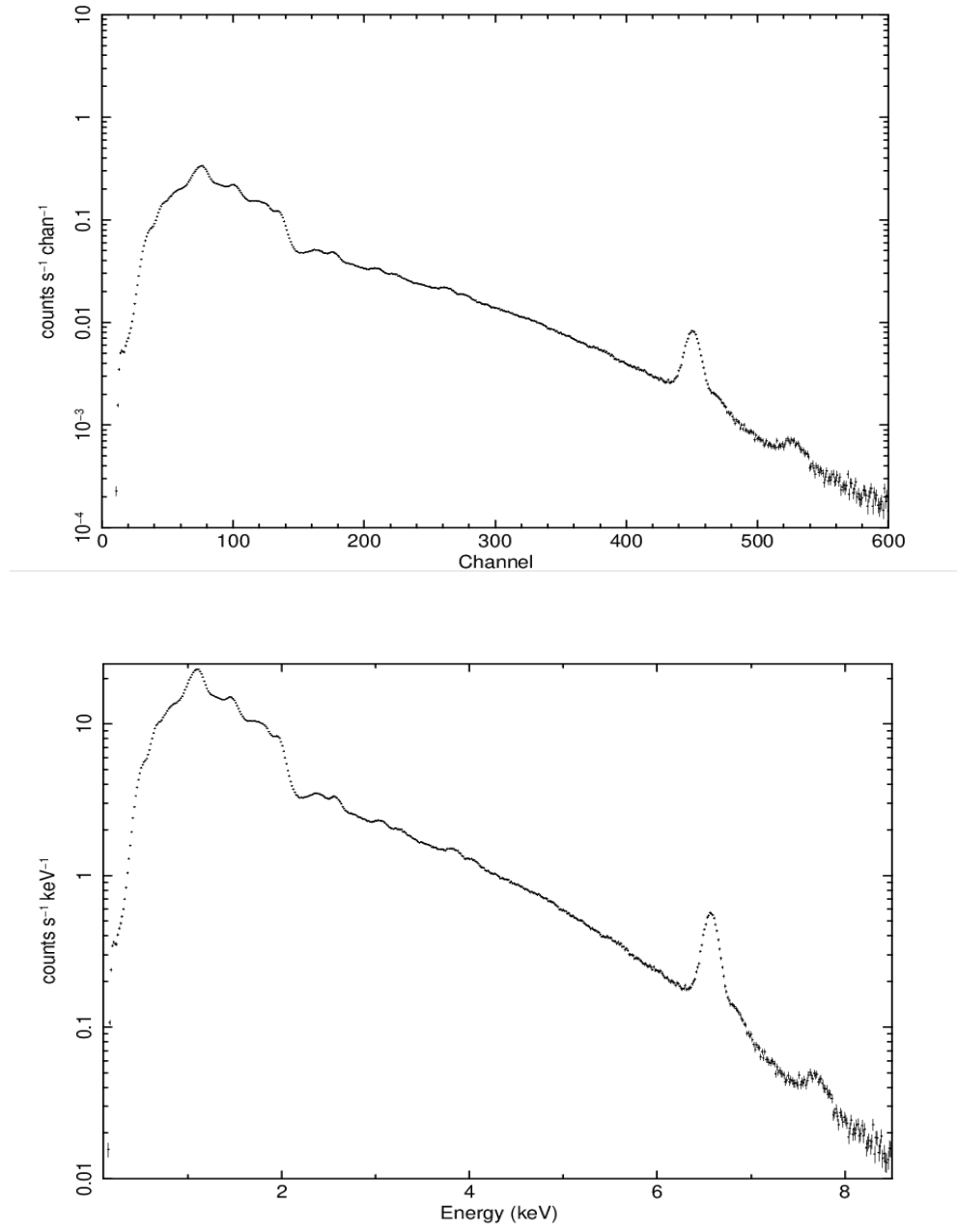


Figure 2.3: This is a spectra of the Perseus cluster using CHANDRA, the upper image is the raw .pi file while the lower image is the spectra with an rmf and arf attached. The axis changes to real units through this.

2.3 Modelling CHANDRA Spectra

To extract metallicity, temperature, turbulent velocity and redshift from the data, a model must be fit over the rmf and arf corrected data. A model will attempt to guess a set of values and output a generated spectra. This model will then use chi-squared statistics to increase/decrease values to match the observed data. There are several tools used to create these models with different model types, but the two that are used in this thesis are Xspec, a model fitting tool made by NASA’s HEASARC, and SPEX a model fitting tool made by SRON (Netherlands Institute for Space Research). These two tools are the standard in modelling emission spectra in X-ray astronomy. For CHANDRA data the tool used was Xspec, in Chapter 4 XRISM data will test the use of both Xspec and SPEX.

All models used for CHANDRA cannot use the full broadband available as the quantum efficiency in the ACIS drops well below 90% below 0.5 keV, and the signal-to-noise ratio diminishes beyond 10 keV. This means that photons beyond these regions must be ignored, and photons from “bad” pixels will also be ignored. To define the metallicity abundances a model must use a predetermined abundance table that defines solar metallicity values up to Zinc. There are multiple abundance tables used that do not agree with each other, with the two most common as: Andres and Grevesse [2] and Lodders [64]. While working with CHANDRA data the Andres and Grevesse abundance table will be used. The models also must include the current cosmological parameters to account for proper redshift calculations, which in this thesis are: $H_0 = 70 \frac{km/s}{Mpc}$, $\Omega_M = 0.3$ and $\Omega_\lambda = 0.7$.

2.3.1 Xspec Model Components

Xspec supports multiple different model components that may be combined to produce full spectra. These components are split into 5 different subsections: additive components, multiplicative components, pile-up components, convolution components, and mixing model components [3]. Additive components represent the forms and sources of emission, additive components are the only component required to produce a model. Multiplicative and convolution components apply transformations on the additive component, multiplicative only applies flat transformations per energy bin while convolution may go across bins. A pile up component is used for bright point sources, removing pile-up effects from the brightest objects in the X-ray spectrum. Mixing model components are only effect systems that require reading in multiple regions at one time, taking into account the influence of neighbouring regions onto their spectra. Mixing model components create 2D models which are out of scope for this thesis.

The two main components used are `apec`, an additive model component, and `phabs`, a multiplicative model component, thus the naming scheme of these models will be in the form of `phabs*apec`. `apec` (Astrophysical Plasma Emission Code) is a model that contains data of more than 10^6 different characteristic X-ray lines, it calculates the emissivity of both the characteristic X-ray lines and the continuum [102]. `apec` assumes that the object observed (the ICM) is a hot optically thin plasma that is in collisional ionization equilibrium, the data of the characteristic lines is stored in the AtomDB database. The standard `apec` component has 4 different parameters, these are temperature, metallicity, redshift and normalization. The temperature is defined as the plasma temperature of the ICM in terms of keV, 1 keV is equivalent to 11.6×10^6 K, if the temperature falls below 1.7 keV it is considered to be a galaxy group instead [75]. The metallicity of the standard `apec` model is a combination of elements between C - Ni, the output then provides a total abundance ratio in comparison to solar metallicities. The redshift should be the redshift of the center of the galaxy cluster, this usually is the BCG's redshift. Redshift is a parameter that should be passed in as a known value otherwise the computing time for model generation increases exponentially. The normalization is defined as:

$$norm = \frac{10^{-14}}{4\pi(D_A(1+z)^2)} \int n_e n_H dV. \quad (2.1)$$

D_A is the angular diameter distance to the cluster, n_e is the electron density and n_H is the hydrogen density (proton density). `apec` has more component variants, such as `bapec`, `vapec`, `vvapec` and `btapec`, with each representing an additional component atop the `apec` model. `bapec` has a parameter for a Gaussian sigma, this is used for velocity broadening in characteristic X-ray lines, providing a broadening sigma in terms of $\frac{km}{s}$. `vapec` contains 13 parameters, each representing abundances of elements between He - Ni, the abundances are taken with respect to Solar ratios. `vvapec` can adjust all metal abundances up to Zn, both `vapec` and `vvapec` can be combined with a velocity broadening parameter named `bvapec` and `bbvvapec` respectively. Finally `btapec` is a two temperature + velocity broadening model, where the X-ray continuum and emission lines disentangle their temperatures and become separate parameters in terms of keV.

`phabs` is a model component that represents photoelectric absorption with only one parameter given: the projected hydrogen density through the full column of the cluster ICM. This is the only other parameter that is given a predicted value per cluster, the value for hydrogen density is found through HEASARC's H column density tool, pulled from the HI 4 Pi Survey. The `phabs` model is a scalar variable defined by this equation:

$$M = \exp^{-n_H \sigma(E)}. \quad (2.2)$$

$\sigma(E)$ is the photoelectric effect cross section, the cross section where a ray and atom interact. This with **bapec** and **btapec** produces most of the models within this chapter.

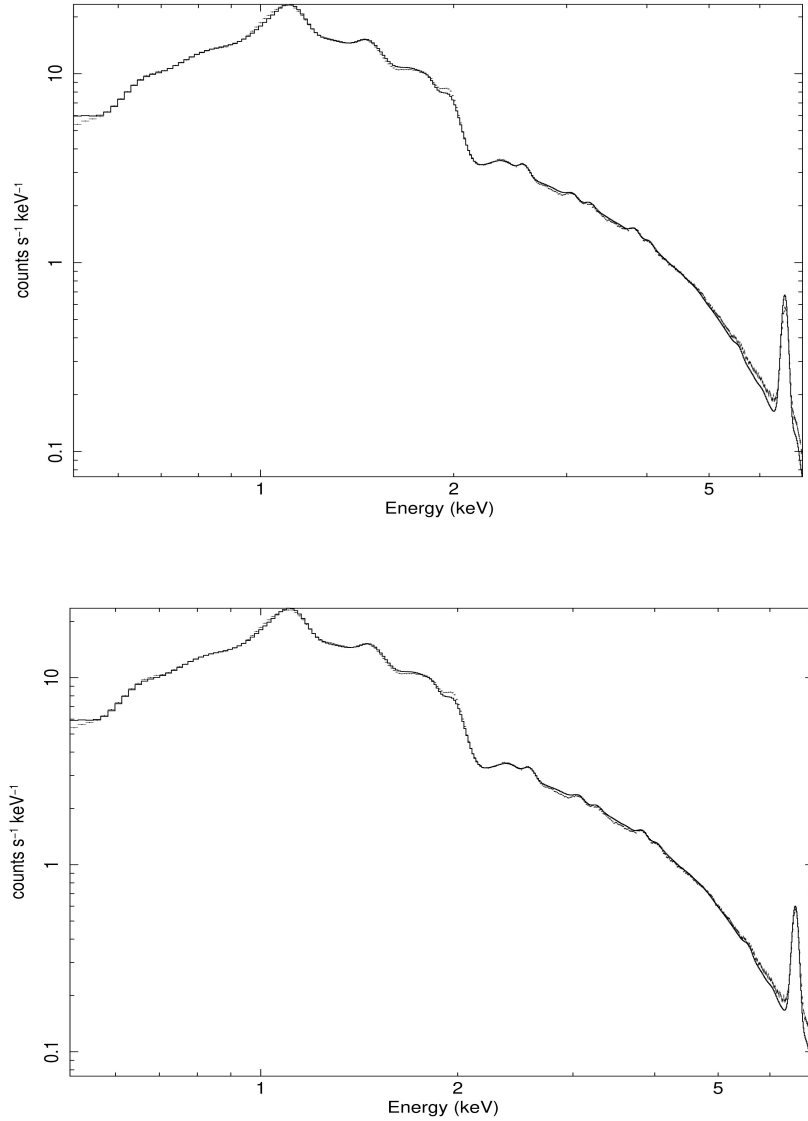


Figure 2.4: Spectra pulled from Abell 426, attempting to use two models **bapec** (upper) and **btapec** (lower), the data appears as points with error bars whilst the model is the black stepped line. As observed, the 2-temperature model is more accurate at matching the Iron-K data peak.

2.3.2 Model Outputs

Each cluster has extracted spectra from the annuli regions and a XRISM Resolve shaped region (2.9 x 2.9 arcmin square). Two models: `bapec` and `btapec`, are tested on these annular regions. Based upon the residuals between the data and the model, the lowest residual ratio selects the model. In many cases a two temperature model is not needed, but for clusters like Abell 426 as shown in Fig 2.4 `btapec` is used instead to align with the Fe-K complex. Once complete the models output 3 important values, radial metallicity, radial temperature and the photon counts over the entire continuum is produced.

This final value is important as it can calculate the flux in different energy bands, for example the continuum can be isolated around the Iron-K peak providing only Fe-K photon counts. This gives the capability of observations of other visible metals in the spectrum, but Fe-K is predominantly used as certain instruments in other missions (such as Hitomi and XRISM) cannot resolve data below 1.8 keV. The process of counting photons over the Fe-K complex cannot distinguish between photons from bremsstrahlung continuum and photons in the characteristic line. These continuum photons must be removed, a process that requires interpolation over the broadened characteristic line. This done by observing photon counts of two energy values near the broadened characteristic line, usually in a small bin (0.5 eV width), then extrapolating the slope between the two sides of the broadened line. Over small ranges this becomes sufficiently close to being a straight line. The amount of photons under this straight slope is calculated and then removed from total photon count in the observed metal line. To be thorough this process was done in regions surrounding the lines that do not contain a resolved characteristic line. This showed low photon counts which can be considered noise. This proves that assuming the background continuum under characteristic line is equivalent to a straight slope is justifiable and will not affect the overall photon count of a characteristic X-ray line.

The final product extracted from the model is the cooling time. Cooling time is produced by measuring the photon counts, temperature and radius of the region and using the cooling time equation below [29]:

$$t_{\text{cool}} = \frac{\frac{5}{2}nkT}{L} \frac{4\pi (r_{\text{outer}} - r_{\text{inner}})^3}{3}. \quad (2.3)$$

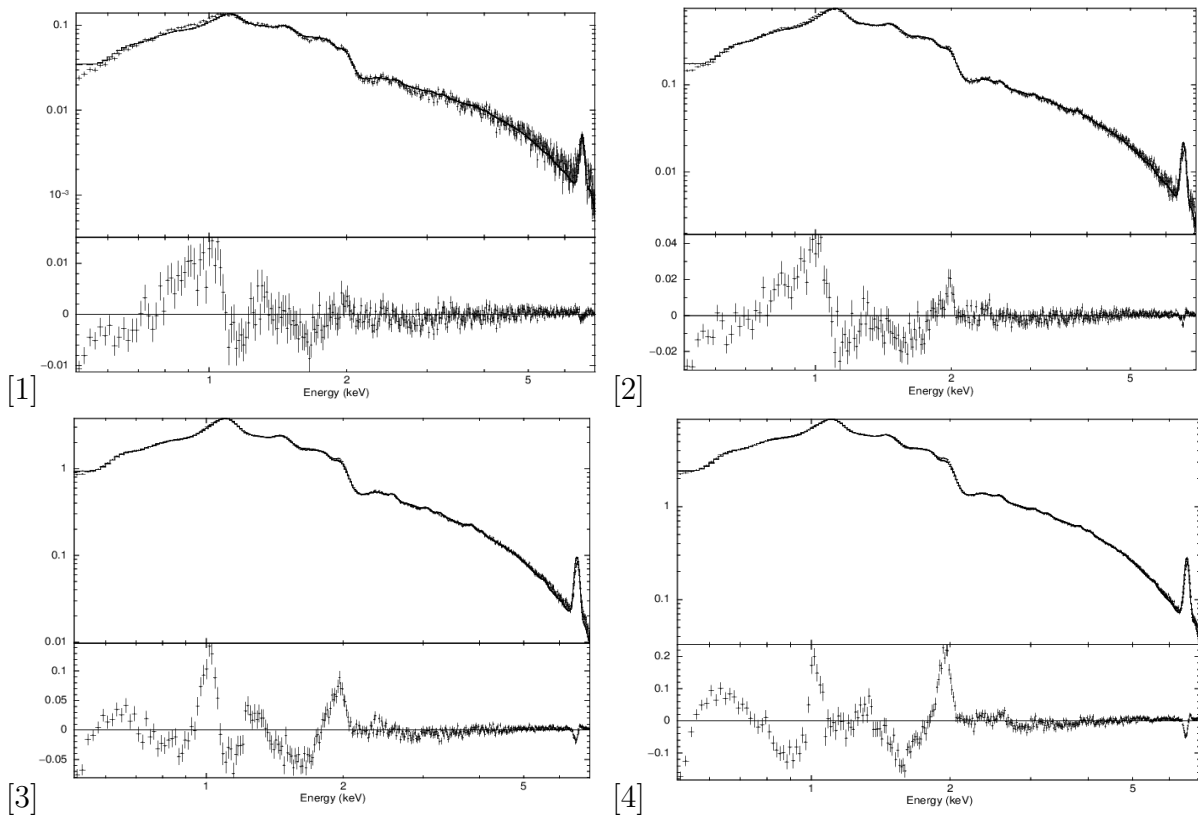


Figure 2.5: Four spectral annuli of A426, each consecutive annulus is at a higher radius. The lower graphs are the residuals between data and model.

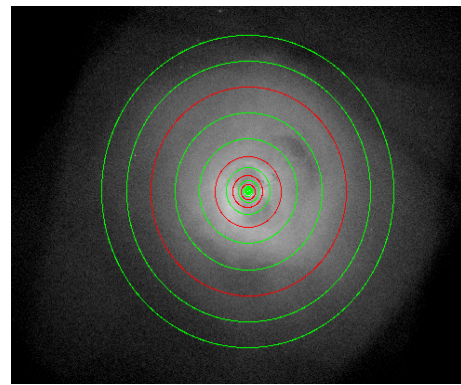


Figure 2.6: Radial Annuli around A426 marked, red annuli are related to spectra in [2.7](#)

2.4 Data Analysis: Radial Profiles

Obtaining this data in concentric annuli produces profiles of important values in galaxy clusters. Predominantly this is attributed to metallicity as this allows to trace increases and decreases throughout the cluster. Other radial components may be observed such as cooling time and the temperature of the hot plasma in collisional ionized equilibrium. Radial temperature trends should show a temperature drop in cool core clusters at the inner radii and no temperature changes in non-cool core clusters. The result of cooling time should provide expected values as it is proportional to temperature, volume and pressure of the system. For a cool core cluster temperature and volume decrease therefore the cooling time should decrease as well. This trend in cooling time should also occur in non-cool core clusters, as the volume dominates the equation, it would continue to decrease. This aspect implies that non-cool core clusters may have small cooling flows occurring near the central-most regions of the cluster but have yet to undergo a large cooling flow to turn into a cool core cluster. Cool core and non-cool core clusters should be able to be defined by eye. Cool core clusters have a higher density optically thin plasma near their centers, this dense core of plasma has a higher luminosity than the surrounding structure. Non-cool core clusters appear as large dim clouds in X-ray imaging.

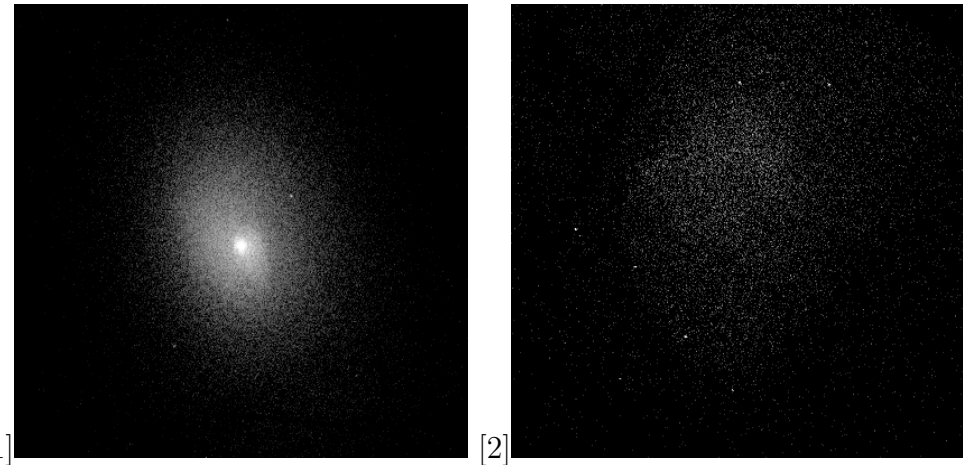


Figure 2.7: [1] A2029 - a cool core cluster. [2] Abell 2319 - a non-cool core cluster.

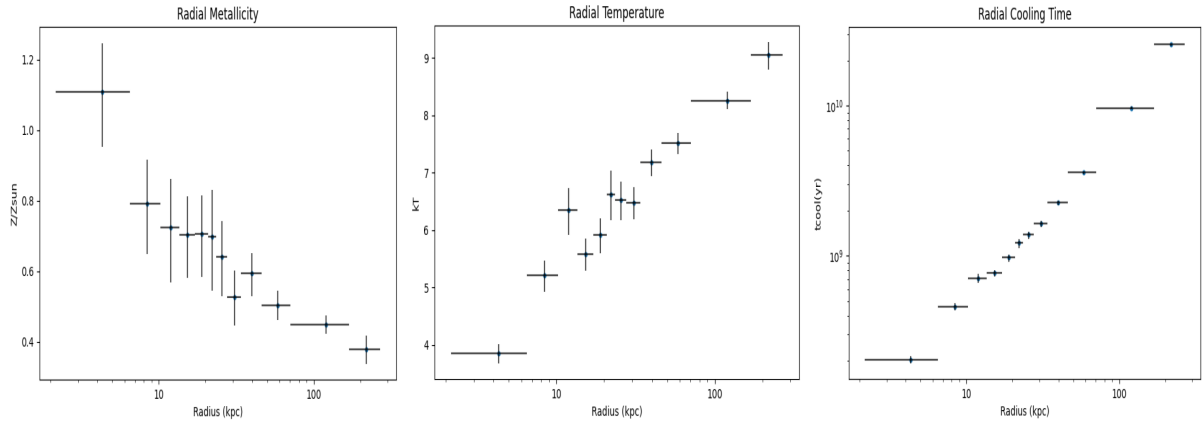


Figure 2.8: The metallicity, temperature and cooling time profiles of the cool core cluster: A2029

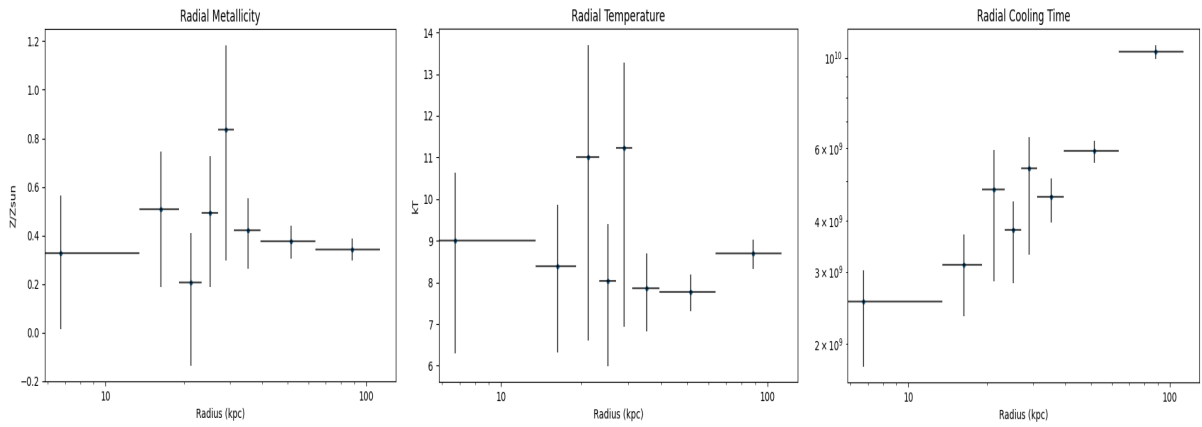


Figure 2.9: The metallicity, temperature and cooling time profiles of the non-cool core cluster: A2319

Types of Clusters in Dataset	
Cool core	Non-cool core
Abell 426*	Abell 754
Abell 478	Abell 2319
Abell 2199*	Abell 3571*
Abell 2029	Abell 3667
Abell 2142*	Coma
AWM7*	
Centaurus*	
CygnusA	
HydraA*	
MS0735	
Ophiuchus*	

Table 2.2: This is the total list of clusters that have had their radial data taken, the marked clusters with * have unexpected profiles for their classification.

Within Table 2.2 4/11 cool core clusters output radial profiles that are expected, wherein metallicities increase closer to the core of the cluster, the temperature towards the core is decreasing at a steady rate, and the cooling time of the clusters decrease towards the core. All clusters lower to a metallicity value of $0.3 Z_{\odot}$ in their outer regions. There are 6 cool core clusters in this dataset that are showing signs of a “dusty core” and one cool core cluster that is showing a flat metallicity gradient. Cool core clusters are defined by hot gas in collisional ionization equilibrium becoming cooler towards the center of the cluster, it is expected that each cool core cluster shows that the ICM temperature decreases at lower radii.

A426, A2199, AWM7, HydraA, Ophiuchus and Centaurus all show a trend in which the closest regions to the core of the cluster have a decrease in metallicity. This opposes the theorized trend wherein metallicity always increases towards the center of a cool core cluster. One theory suggests the possibility of dust particles in the centers of clusters taking cooled out ions in the gas and becoming compounds. These molecules do not emit light in x-ray as they do not undergo recombination radiation or standard photon emission, by definition there will be a decrease in characteristic x-ray lines as less ionized metals can be found [74, 86]. One method to track if this is occurring is through observing the abundance values of Ne and Ar. This is due to them being noble gases thus less likely to combine with dust particles and form cold molecular gas. There is a molecular gas variant of ArH^+ but it is uncertain if that can form in clusters [74]. Dusty cores would show an increase in Ne and Ar abundances while the rest of the metals will show their characteristic de-

crease in these cores. The characteristic lines of Ar and Ne are difficult to distinguish from the bremsstrahlung continuum in most clusters. With CHANDRA’s spectral resolution being incapable of defining several separate lines of the metals, attempting to measure their abundance profiles will only provide large errors. Future missions with XRISM (with the gate valve open) and ATHENA may improve confidence in this theory as the spectral resolution of the instruments on those missions should be lower than 7eV, making many noble gas lines resolvable. A second theory as to why a decrease in metallicity is observed in the central regions of cool core clusters may be attributed to the turbulent inner regions pushing gas outwards. A426, A2199, HydraA and Centaurus all show an extremely turbulent inner region where large cavities are forming near the core, these cavities may have dragged out the metals through their shock fronts and depositing them at a higher radii. The clusters that have this decrease in metallicity near the core also have a metal “peak” which may relate to the radius where these shocks may deposit the cooled out metals, beyond this the metallicity will drop rapidly towards $0.3 Z_{\odot}$ in the outer regions.

A2142 is a strange cool core cluster with a flat metallicity profile. There is one datapoint which spikes from 0.3 to 0.6 but the large error in the datapoint and the surrounding points being lower than average suggests that this is an outlier. A2142 appears to be a dim extended cluster with a flat metallicity profile, a common trait of a non-cool core cluster, and yet the temperature profiles show that there is a clear trend towards a cooled core. This cluster may be a link between cool core and non-cool core clusters. It may be that this flattened metallicity is caused by outside factors like sloshing as a large shock front may be observed within the cluster, or a recent merger event influencing the metallicity in the core [24, 23]. For a deeper examination on A2142 it is suggested to extract spectra specifically from the shock-front in the cluster, under the assumption that it contains the displaced gas in the system.

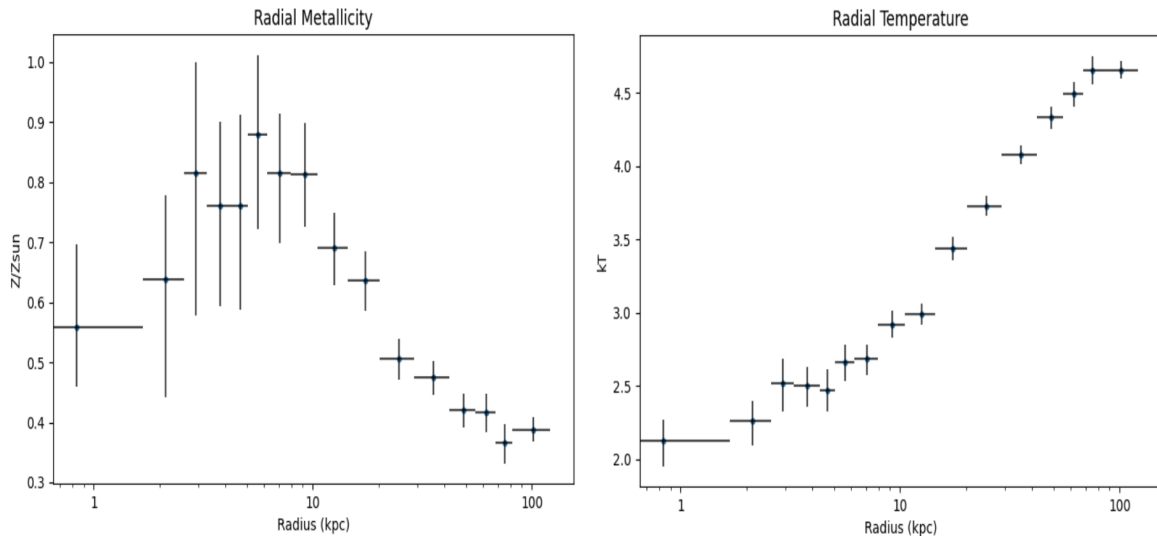


Figure 2.10: Cluster A2199, shows signs of metal depletion in its core, radial temperature acts like a cool core system.

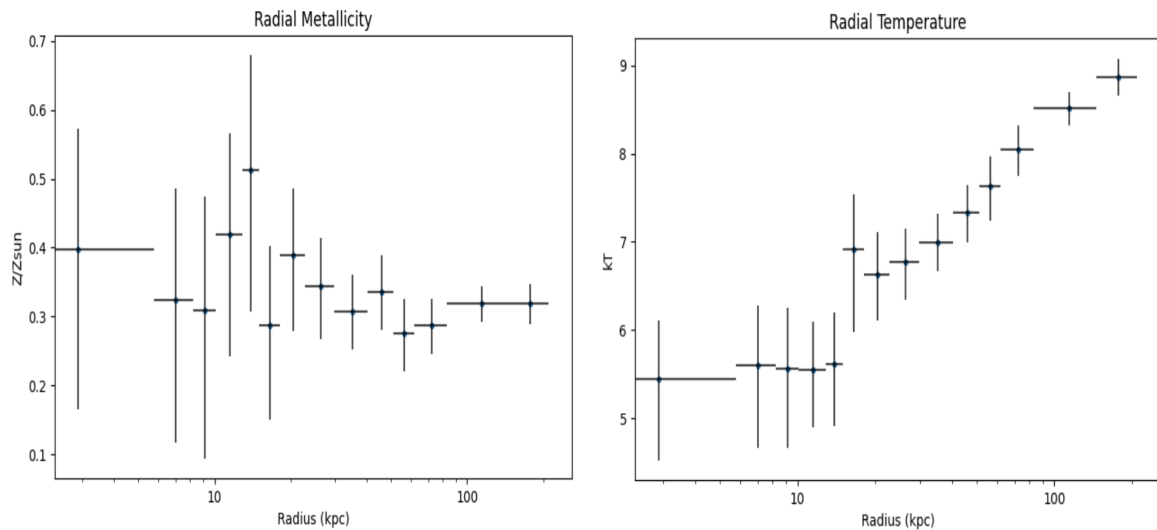


Figure 2.11: Cluster A2142, shows a flat metallicity trend, similar to a non-cool core system, but radial temperature decreases inwards like a cool core system.

There is also one non-cool core cluster that does not align with expected trends: Abell 3571. Abell 3571 seems to have a metallicity profile that slowly increases as it approaches the core of the cluster, a feature that only appears in cool core clusters, and yet the temperature profile appears to be nearly flat. This cluster has had multiple papers discuss its classification, some theories suggest that it is an “intermediate” cluster undergoing the process of converting into a cool core cluster containing a cool core remnant [52, 94, 110]. In the radio and optical bands the cluster appears to have an asymmetrical galaxy distribution, implying external effects such as a merger. Yet in the x-ray band the cluster appears to be quiescent, relaxed to the point that a cooling flow is forming [110]. This may correlate with the fact that there are two other clusters in close proximity on the night sky. These two clusters are Abell 3572 and Abell 3575, they appear so close together that they may spatially overlap in the sky this may cause observations of Abell 3571’s hot atmosphere to be influenced by them. This may explain why the cluster looks like it has a higher metallicity in its core. Overall Abell 3571 has a clear unique non-cool core cluster signature unlike the other 4 non-cool core clusters: an increasing metallicity towards the core showing cooling flows just barely starting to form.

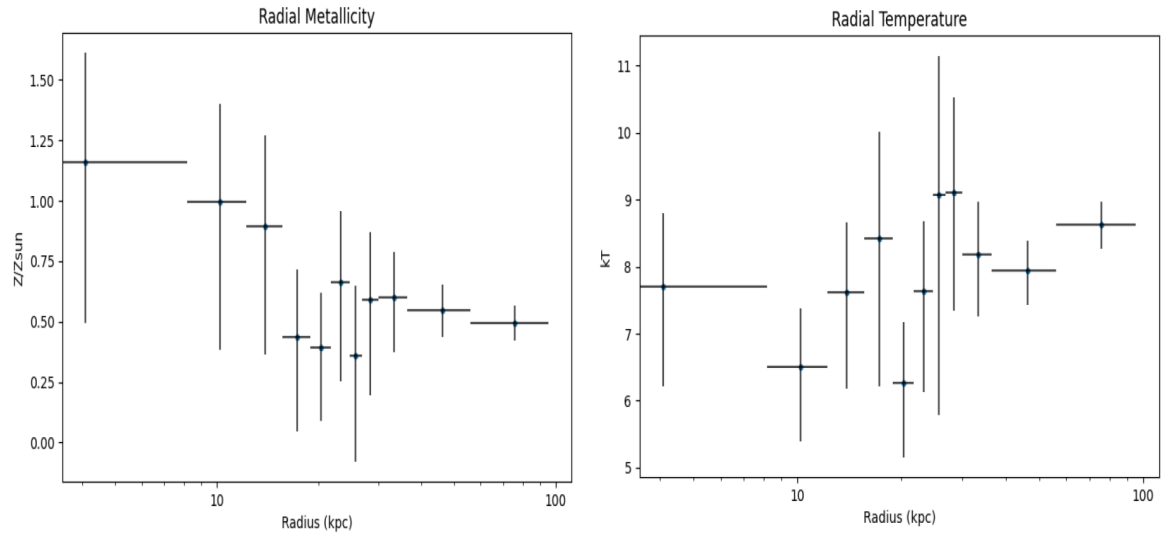


Figure 2.12: Cluster A3571 shows signs of metal accumulation in its core, radial temperature slightly decreases towards the center, between cool core and non-cool core.

While the difference in metallicity profiles between cool core and non cool core clusters are apparent there are similarities found in the outer regions of both cluster types. Both forms show an outer limit of $0.3 Z_{\odot}$, and thus plotting the metallicity profiles together may show other trends within cluster types. Some cool core clusters that have showcased a characteristic metal depletion near their cores. This depletion may actually be the common profile of a cool core cluster, seeing that at specific radii most clusters may have an abundance turnover. The clusters that do not have this feature appear may just be too dim (or distant) to resolve these features in the overall radial profile. This should be expected as galaxy clusters are self-similar, meaning that larger galaxy clusters are an extended scaled version of smaller galaxy clusters. Thus instead radial profiles may need to relate to the cluster's size. Since a cluster's edge is ill defined there is a problem in defining a cluster's "size". A cluster's surface brightness and gas density asymptote towards zero out at an infinite radius so instead like in a purely gravitationally bound system the virial radius is used. The virial radius is a defined radius in which the encapsulated region has a density equivalent to the critical density of the universe: $\sim 3 \times 10^{-26} \frac{kg}{m^3}$. This radius would encapsulate the entire visible cluster and much of the surrounding empty space. By definition the virial radius is not useful as a unit of measurement, so instead R_{2500} is used. R_{2500} is the radius that encapsulates an area of space that has an overdensity of 2500 times the critical density. The value for 2500 times the critical density is defined as:

$$\rho(< r_{2500}) = 2500\rho_{\text{crit}}(t) = 2500 \frac{3H^2(t)}{8\pi G} \quad (2.4)$$

To find the virial radius of each cluster a mass must be defined, this would have to be done by modelling masses with two components, an NFW model and an isothermal model. This process was already done by F. Pulido (2017), M. Hogan (2017) and B. Comis (2011) [20, 50, 91]. Their dataset were used to define R_{2500} of the clusters available. If a cluster's radial profile was obtained but an existing R_{2500} was not found then the cluster is not used in this data comparison. Clusters missing from these datasets are: A426, A754, and Coma and thus will not be available for structural comparisons. This lowers the available clusters to a total of 13 in R_{2500} comparisons. Future work should focus on expanding this dataset to all well-known clusters.

Pulling these trends together into radial profiles provides a clear view of what regions in a cluster are enriched with metals. One key finding shows throughout most of these clusters the metallicity will asymptote to $0.3 Z_{\odot}$ in the outermost regions. As the clusters chosen span from redshifts 0.01 - 0.54 and studies done by A. B. Mantz (2017) [68] which extend this range to $z = 1.2$ all still show this asymptotic approach to $0.3 Z_{\odot}$, it implies that clusters must have been formed with higher metallicity contents than expected.

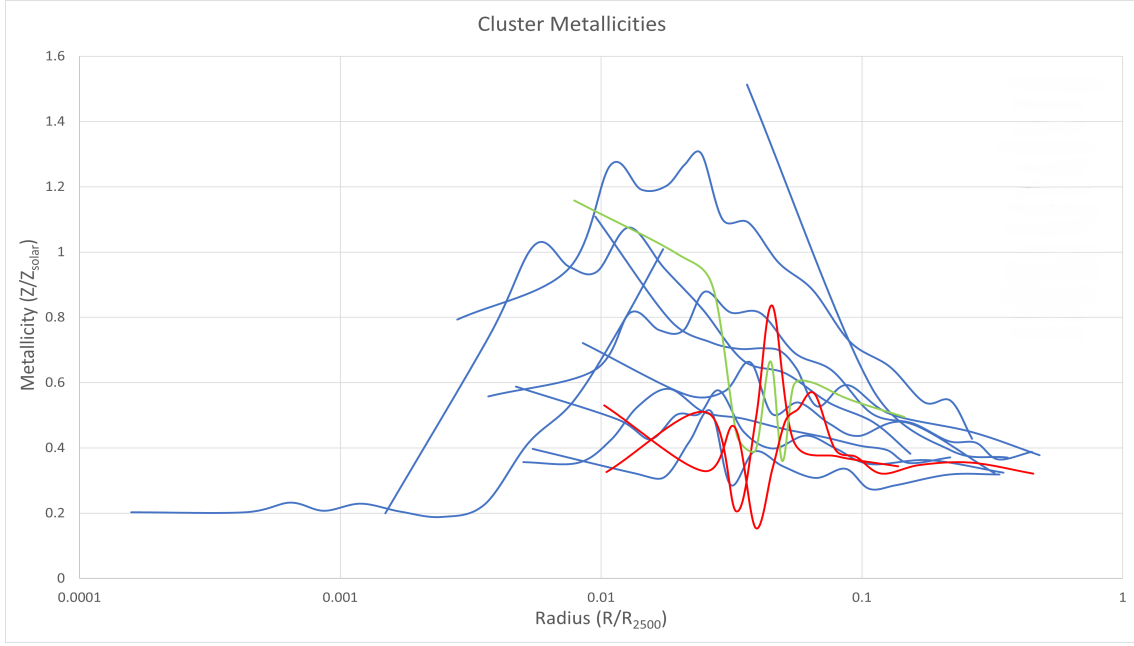


Figure 2.13: Cool core vs non-cool core radial metallicity comparisons, red lines are defined as non-cool core, blue is cool core and green is A3571.

Within Figure 2.13 the non-cool core clusters appear to fluctuate around $0.3 Z_{\odot}$ throughout the entire cluster which was expected, any increases in metallicity would bring into question the non-cool core classification. Cool core clusters appear to have a peak in metallicity around $0.01 R/R_{2500}$ and in their outermost radii it all approaches an abundance of ~ 0.3 . Some larger cool core clusters that have their innermost regions spatially resolved by CHANDRA appear to have a depletion in metallicity at the core of the cluster, with the largest showing values that fall below $0.3 Z_{\odot}$. The metallicities falling below 0.3 may hint to other sources of metal depletion like dust cores, or expulsion due to cavity uplift.

Other observations may be made by comparing the abundance radial profiles to other documented values such as the cluster's mass and star formation rate [50, 69]. As the datasets do not fully contain all of the clusters observed the missing clusters will be removed for these comparisons. There are no visible trends between the mass of the cluster (within R_{2500}) and metallicity. The non-cool core clusters are at opposite ends of the mass scale, whilst the cool core clusters appear to spread through the entirety of the scale, with a maximum mass of 5×10^{14} solar masses. The star formation rate, obtained by McDonald (2018) [69] is done by observing the optical line luminosity of H α , UV flux, and the 24 μ m flux, this data is an aggregate of multiple missions and SFR studies. The star formation

rate values are given in logarithmic format, with SFR being the total amount of solar mass produced per year. As seen in Fig. 2.14 the star formation rate rarely exceeds $1 M_{\odot}$ per year, with CygnusA being an extreme outlier containing a strong AGN. Centaurus appears to have the lowest star formation rate within the subset of clusters. The dataset should be extended to use more clusters from the McDonald (2018) paper [69] in future work. No trends may be found within this dataset, reinforcing the fact that more galaxy clusters must be added with published SFRs for more extensive research.

Errors may be found when observing the metallicity or temperature values in the central regions of certain clusters. The first error occurs with galaxy clusters that have very bright cores as the point source removal algorithm may fail to remove the AGN. This may cause a sudden shift in metallicity and temperature as AGN photons mix with the photons produced by the ICM. The other error occurs due to the physical locations of the pixels in ACIS-I mode. The location of the clusters imaged in this mode tend to be closer to the edge a chip, leading to a physical gap in photon information over 22 pixels. This occurs in extended non-cool core clusters like the Coma cluster, as all 4 ACIS-I chips are used to capture the full cluster in one image. The Coma cluster's central regions are located near the intersection of the four ACIS-I chips which is a large gap in the instrument. This causes the inner annulus to be larger than most clusters, which increases the radial error bars within both the temperature and metallicity radial profile graphs.

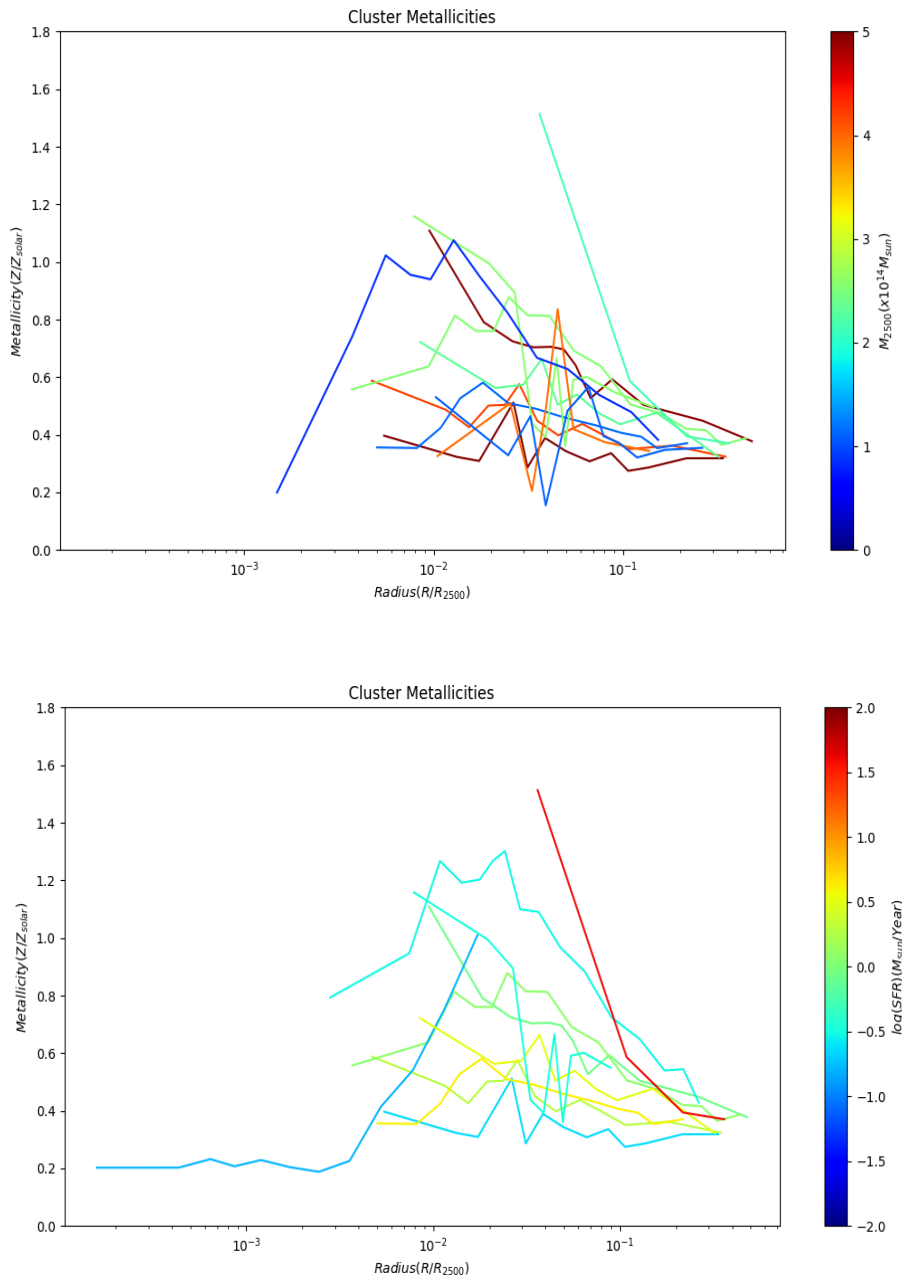


Figure 2.14: Galaxy cluster radial metallicity trends comparing between the cluster's mass (top image) and the cluster's star formation rate (bottom image). Data for these clusters were taken from Hogan (2017) and McDonald (2018) [50, 69].

2.5 Data Analysis: XRISM Region

This method of data collection can also obtain a spectrum of a cluster in the exact dimensions of XRISM's Resolve instrument. The field of view on Resolve is a square with dimensions of 2.9 x 2.9 arcminutes, therefore a square region centered on a cluster was added for each cluster in the dataset. This spectrum provides an overall temperature, turbulent velocity and metallicity which can be used to compare to values found by XRISM in the future. This does not measure structure within the cluster since it produces one spectrum of a large central region. Through this I find the expected total luminosity of the inner region and the total photons emitted by different metals visible in the spectrum.

The method of obtaining the photon counts of specific metals requires narrowbands over the model which defines key characteristic x-ray lines. Each metal appears as a wide Gaussian atop the bremsstrahlung continuum near its characteristic X-ray line energy. The metals observed (in addition to the Fe-K complex between 6-7keV) were the Mg-K alpha and beta complex spanning from 1.27 - 1.47 keV, the Si-K complex found at 1.82 - 1.88 keV, the S-K complex found at 2.42-2.48 keV, the Ar-K complex found between 3.08 - 3.18 keV and finally the Ca complex found between 3.82-3.93 keV. The Mn and Cr lines were too dim for any cluster to properly differentiate between their characteristic lines and the background continuum and were not measured. While observing photons from characteristic x-ray lines, the background bremsstrahlung continuum should be subtracted, otherwise the photon count emitted by the specific line transition will be overestimated. The data was partitioned to take photon counts in 0.5eV bins, therefore the value of counts within each 0.5eV bin on both edges of each complex was calculated and interpolated under the characteristic line as a straight line. This interpolated line is treated as the background continuum, thus the residual photon counts would represent photons produced purely by emission lines. These results are used for a selection process for clusters that should be observed by XRISM, which will be expanded on in Chapter 3.

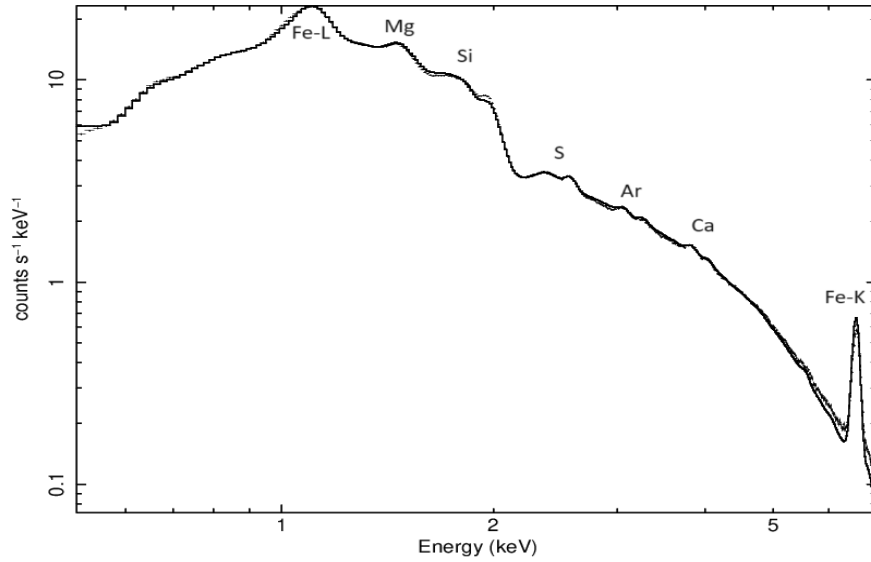


Figure 2.15: The locations of metals within the spectrum of A426 (Perseus), knowing the locations allows for the exact amount of photons emitted by each metal to be calculated.

This data is reformatted for ease of use for future work. Key cluster values are: temperature within the region, the total exposure time required to produce the spectrum, the total number of photon counts, the average metallicity within the region and the specific flux of the Iron-K complex. The data found from the XRISM Resolve region and the radial profiles of each cluster can be compiled into a datasheet. These datasheets can be used as resources to compare CHANDRA values (such as the temperature, metallicity and flux) to XRISM findings. They can also be used as a resource to highlight outlier clusters, such as clusters with high metallicity, high temperature or odd radial profiles. Having values like high metallicity may provide target clusters for studies of early enrichment scenarios. Each datasheet may be found within the appendix of this thesis.

Cluster Data					
Cluster	Exposure Time (ks)	Temp. (kT)	Metallicity (Solar)	Total Flux (erg/cm ² /s)	Iron-K Flux (erg/cm ² /s)
A426	768	3.64	0.558	2.68×10^{-10}	8.78×10^{-12}
A478	42	5.85	0.369	7.46×10^{-11}	2.02×10^{-12}
A754	138	7.31	0.338	1.21×10^{-11}	2.78×10^{-13}
A2029	77	7.19	0.539	6.80×10^{-11}	2.37×10^{-12}
A2142	155	7.94	0.318	4.51×10^{-11}	9.27×10^{-13}
A2199	158	3.74	0.532	4.17×10^{-11}	1.4×10^{-12}
A2319	90	8.46	0.367	3.12×10^{-11}	3.15×10^{-13}
A3571	34	8.11	0.53	3.37×10^{-11}	9.15×10^{-13}
A3667	494	6.59	0.352	1.08×10^{-11}	2.72×10^{-13}
AWM7	182	3.32	0.831	1.98×10^{-11}	8.61×10^{-13}
Centaurus	660	1.78	0.613	3.89×10^{-11}	4.66×10^{-13}
Coma	28	8.67	0.268	1.28×10^{-11}	1.42×10^{-13}
CygnusA	99	7.42	0.882	6.11×10^{-11}	3.14×10^{-12}
HydraA	215	3.59	0.419	3.42×10^{-11}	8.68×10^{-13}
MS07	434	5.20	0.376	6.05×10^{-12}	1.49×10^{-13}
Ophiuchus	279	7.73	0.478	9.39×10^{-11}	2.86×10^{-12}

Table 2.3: Data placed in cluster datasheets, used for quick comparisons, total flux in ergs/cm²/s and photons/cm²/s found on the datasheets themselves.

2.6 Conclusion

Through the use of Chandra's X-ray database containing multiple exposures of hundreds of galaxy clusters the overall structure of both non-cool core clusters and cool core clusters may be observed. In this dataset I studied 16 commonly known clusters and extracted metallicity and temperature radial profiles by using Xspec modelling on each cluster.

Through this process general trends were discovered for both cool core and non-cool core clusters. All non-cool core clusters oscillated around $0.3 Z_{\odot}$, with flattened temperature profiles. Meanwhile cool-core clusters appear to have their metallicity peak at a radius between 0.008-0.05 R_{2500} . The metallicity at this peak varies dependent on the cluster, between $0.5-2 Z_{\odot}$ within this dataset. Cool core clusters appear to have a steady decrease in metallicity starting at radii higher than $0.05 R_{2500}$, with the metallicity asymptotically reaching $0.3 Z_{\odot}$ at large radii. This implies that there has to be an early enrichment scenario as clusters found at varying redshifts ($z = 0.01 - 0.54$) all reach $0.3 Z_{\odot}$ at large radii. The edges of the cluster contain ICM gas that has not undergone cooling flows. Therefore this gas found at large radii should hint at the metallicity of the universe when these clusters were formed, yet values observed are higher than the rate of metal production by standard supernovae. At radii below $0.008 R_{2500}$ several cool core clusters appear to have quick drop in their metallicity, some going below the observed outer limit of 0.3. This change in trend implies that there is a component removing metal ions, such as dust combining with cooled out ions. This combination between dust and metal ion removes its capability of generating x-ray characteristic lines, causing metals to appear as if they have been removed from the cluster. Other possibilities for this sudden extinction in metallicity may be correlated to large cavities being located in these inner regions. These cavities may be pushing out the surrounding ICM, physically pushing the high metal concentration out of the core.

There are a few unique clusters that do not follow the trends in the dataset. The two clusters that do not fit in the standard cluster classification are Abell 3571 and Abell 2142. Abell 2142 is considered to be a cool core cluster, as the radial temperature of the cluster decreases going towards the core. Unlike the rest of the cool core clusters Abell 2142 appears to have a flat metallicity profile which is a characteristic of non-cool core clusters. Abell 3571's metallicity clearly increases towards the center of the cluster while the temperature profile of the cluster appears to be nearly flat. This is an abnormal non-cool core cluster, as it has a metallicity signature of active cooling flows but its temperature profile does not look like a cluster that is cooling.

Chapter 3

Simulating High Spectral Resolution Galaxy Clusters

The turbulent motions of the gas in the ICM should theoretically be proportional to the power of the AGN, but measuring the precise velocity dispersion proves to be difficult using low spectral resolution X-ray data. This leads X-ray astrophysics to turn to XRISM, a new X-ray mission that captures spectra at a spectral resolution of 5eV. Prior to the launch of this mission, galaxy cluster data is simulated and modelled to select viable candidates to propose for observation time with the new telescope. This process uses the datasheets produced in Chapter 2 as initial values, then clusters are converted into high spectral resolution simulations. These candidate clusters are then selected by observing the total photon counts and possible unique structures, as the usage time available on the telescope is limited. Through this process three clusters are selected and proposals for observing time have been submitted. These simulations are then tested to see the accuracy in which modelling can extract the simulated turbulent velocity dispersion.

This chapter includes original research, using data from the publicly available CHANDRA X-ray Observatory database, Hitomi data found publicly on NASA’s HEASARC website and XRISM tools available on HEASARC as well. All the X-ray data within this chapter was analyzed and produced by Neo Dizdar unless stated otherwise.

3.1 XRISM

XRISM is a soft X-ray mission done in collaboration with JAXA and NASA, this mission was successfully launched on September 7th 2023, with first light images taken late-October 2023. The payload contains two scientific instruments: Xtend and Resolve.

Xtend is an imager that has a 38 x 38 arcmin field of view, used for imaging X-ray data. Resolve is an X-ray spectrometer, having a smaller field of view at 2.9 arcmin but a high spectral resolution at 5eV at a bandpass of 0.3 - 12 keV [78]. This in comparison to CHANDRA's ACIS instrument (95 eV resolution) provides very precise spectral lines in smaller regions on the sky. Resolve also extends the bandpass beyond CHANDRA's upper limit of 8 keV. Resolve's detector is a 6x6 pixel microcalorimeter array, one pixel is turned off as an orientation pixel. X-ray microcalorimeters are thermal X-ray counting devices split into 3 components, an absorber, thermometer and heat sink, this absorbs an X-ray and accurately measures the temperature of the incident photon to a precision of up to 5eV [41]. This spectral resolution is important to glean information about velocity changes within the ICM, as the widening of thin spectral lines due to Doppler broadening may be measured. This increases the accuracy in models observing the motions of gas in clusters. Unfortunately the image resolution of Resolve is poor, as each pixel covers ~ 30 square arcseconds in the sky, this means that features smaller than this in the sky cannot be resolved. Using Xtend and Resolve in tandem can provide large high resolution X-ray images with smaller important regions being provided with a high resolution spectrum.

Xtend and Resolve are built to be similar to the soft X-ray spectrometer (SXS) and soft X-ray imager (SXI) on Hitomi, a previous mission that had lost contact in 2017 shortly after obtaining an image of Perseus. This image of Perseus is used as a template for simulations of XRISM, allowing simulated data to be generated before the launch of the mission. This is done through XSELECT, a tool to generate spectra provided by HEASARC. As a basis the spectrum of Perseus is used to test if precise metallicities and velocities may be obtained, focusing around the Fe-K complex as it has the highest signal-to-noise ratio of all visible lines in the spectrum. Importantly while the SXS (or Resolve) instrument is a high resolution spectrometer the SXI (or Xtend) instrument can also produce an X-ray spectrum, its resolution being 180eV [76]. SXI data is comparable to current CHANDRA data over larger regions. This allows for Xtend to compensate for Resolve if there are any issues with the high resolution spectrometer.

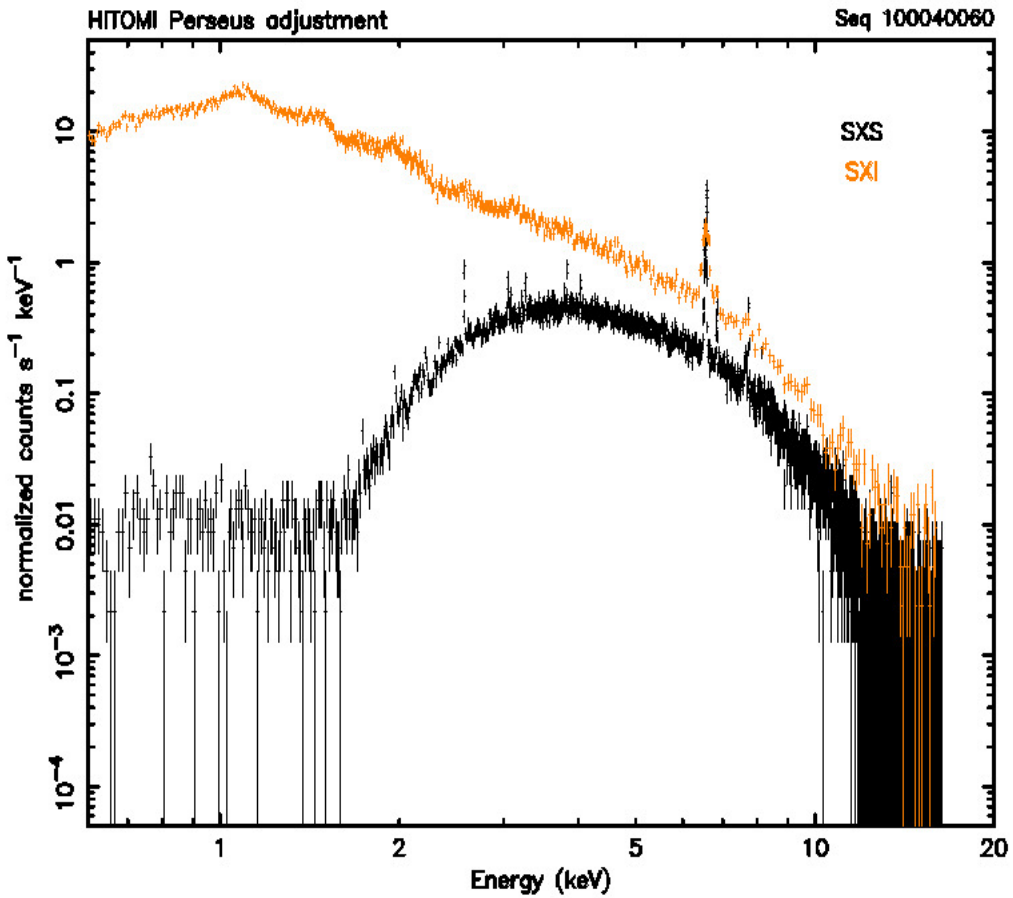


Figure 3.1: A spectrum of the Perseus cluster captured by Hitomi. The black datapoints represent the spectrum captured by the SXS instrument whilst the orange is the spectrum captured by the SXI. The SXI spectrum has an overall lower spectral resolution, while the SXS image has an attenuated spectrum due to gate valve issues.

3.1.1 Gate Valve

Gate valves are important components on any space telescope, as they are used to protect the instruments behind the valve. They protect the instruments from initial outgassing within the telescope on launch and the initial operation of the telescope, these valves may be considered as aperture doors within the telescope. Outgassing is where gas trapped within components is released, this may be done through evaporation or sublimation of components within the telescope [46]. The valve contains a $260\text{ }\mu\text{m}$ thick beryllium window, this window itself will attenuate the luminosity of any object it observes. This removes the soft X-ray photons, stopping their approach to the instrument at energies below 1.7 keV. There will be noise in this attenuated region, this noise is produced by the instrument. All data below this limit is considered to be obsolete while the gate valve continues to cover the instrument. This filtering effect persists throughout the entirety of the spectrum, lowering the total photon counts beyond 1.7 keV. At high energy key regions such as 6-7 keV (Fe-K complex) the attenuation of photons is minimal and should not affect abundance or velocity measurements within the visible metals. In Fig. 3.1 there are important characteristic X-ray lines attenuated below this 1.7 keV limit, some of which are N (0.5 keV), O (0.65 keV), Ne (1.02 keV), Fe-L complex (1.1 keV) and Mg (1.47 keV) [34]. As Si lines appear between 1.8 and 2.4 keV this is a component that is significantly affected by the attenuation of photons through a gate valve. Major Si lines (like Si XIV) will appear above the noise but the total photon counts will be diminished. Observing through a gate valve loses key information on cooler gases which may have different bulk motions in comparison to the warmer gases (at higher keV). Trends shown Si and S may be missing correlated values with cooler metals by only observing a spectrum with data over 1.7 keV.

The effect of a gate valve on X-ray spectra is important to observe as the Hitomi mission was lost before the gate valve could be opened. Thus the only data provided by Hitomi was data attenuated by a gate valve over the SXS instrument. The SXI instrument did not have a gate valve issue and thus it contains the full X-ray spectrum at a low spectral resolution. The gate valve has proven to be an issue for the XRISM mission as well, as the method of moving the gate valve has failed, with multiple attempts to open the valve door taken post mission launch. This means that Cycle 1 Resolve data will be provided with an attenuated spectrum, changing the expected energy range from 0.2 - 12 keV to 1.7 - 12 keV.

In this chapter most simulations were done with the gate valve closed, which means that the spectrum is attenuated to accurately match the expected early results of XRISM spectra. Initially simulations were generated with the gate valve open prior to the news that there were mechanical failures in opening the gate valve aboard the XRISM telescope. The gate valve open spectra were kept to visually compare the effect of the gate valve on the shape of the overall spectrum. Gate valve open simulations are not used for any further science. Limiting photon counts within characteristic X-ray lines to gate valve closed simulations will provide an overall minimum expected luminosity. In the event that the gate valve opens, by selecting clusters using gate valve closed simulations as a threshold for observation time most spectra will produce higher counts than anticipated. This means that XRISM will prioritize brighter clusters that require the use of the Resolve instrument first since scientific papers can still be produced with the gate valve closed. In the future if the gate valve successfully opens dimmer clusters may be observed with the Resolve instrument. While the gate valve removes important data, hot gas science may still be done on well known clusters.

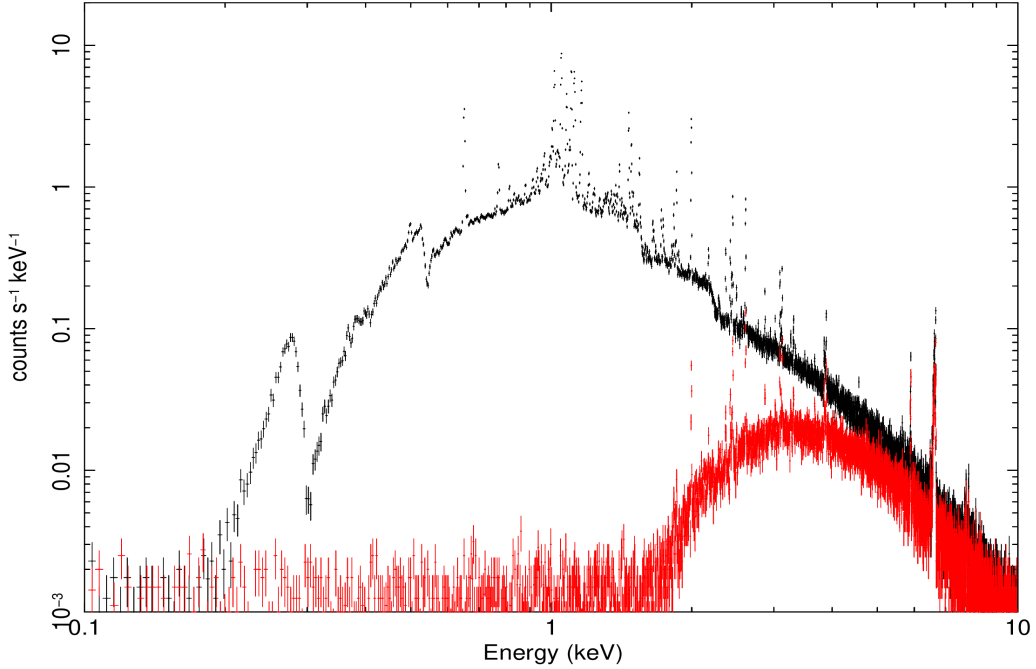


Figure 3.2: Simulation of M87 through XRISM’s Resolve instrument, with a 1 Ms exposure time. Red points represent a closed gate valve, black points represent it opened.

3.2 Simulating Spectra

Since each cluster contains unique ratios of metals and unique velocity broadening structure simulations of specific galaxy clusters require real data as a baseline. To properly simulate these clusters CHANDRA data was used as a baseline. The data provided in the datasheets produced in Chapter 2 was extracted and converted to the spectral (and image) resolution of Resolve. This data was generated through Xspec, using key datapoints found on the datasheets such as: the temperature, the overall abundance, the redshift, the photon normalization and the hydrogen column density. These 5 components are used to create a `phabs*apec` spectral model. As these simulations are made to also test the sensitivity of velocity broadening on high resolution X-ray characteristic lines a velocity broadening component was artificially added to the model, instead making these `phabs*bapec` models. This process is done several times on each selected cluster, with the velocity broadening value being the only variable that changes, the main turbulent velocities that were selected were $100 \frac{km}{s}$, $200 \frac{km}{s}$ and $300 \frac{km}{s}$. Certain clusters with known higher velocity broadening effects were simulated with higher values such as $600 \frac{km}{s}$, $1000 \frac{km}{s}$ and even $2000 \frac{km}{s}$ turbulent speeds.

This process produces a model for the photons to mimic, to actually get a full spectrum and image simulated it requires usage of HEASARC's Ftools. XSELECT is a tool used to assist in generating spectra. This process requires the image of a 2.9×2.9 arcmin field of view over the selected cluster and its spectrum, typically done by using CHANDRA images, this field of view is represented as the green box in the datasheets. Once provided the simulation tools require the proper WCS coordinates and the exposure time to be simulated. Both the exposure time and velocity broadening values become variables that can be adjusted to observe their effects on the spectra. Through XSELECT the mission (XRISM) and instrument (Resolve) must be selected, prior to the launch of XRISM the mission variables were based off of Hitomi's scientific instruments. This simulation software takes the spectral model provided by Xspec and characteristics of the selected instruments and convolves with the data. While generating this spectrum the simulation tools require a defined rmf and arf. These files may be found on the HEASARC website, as Hitomi's arf files that have the gate valve open and the gate valve closed, and rmf files with a range of spectral resolution (5-8eV) are available for use. As the data from XRISM appears to be captured at a resolution of 5eV, the 5eV rmf was used for every simulation. While some simulations also have a gate valve open arf tested this chapter will only use data with gate valve closed arfs.

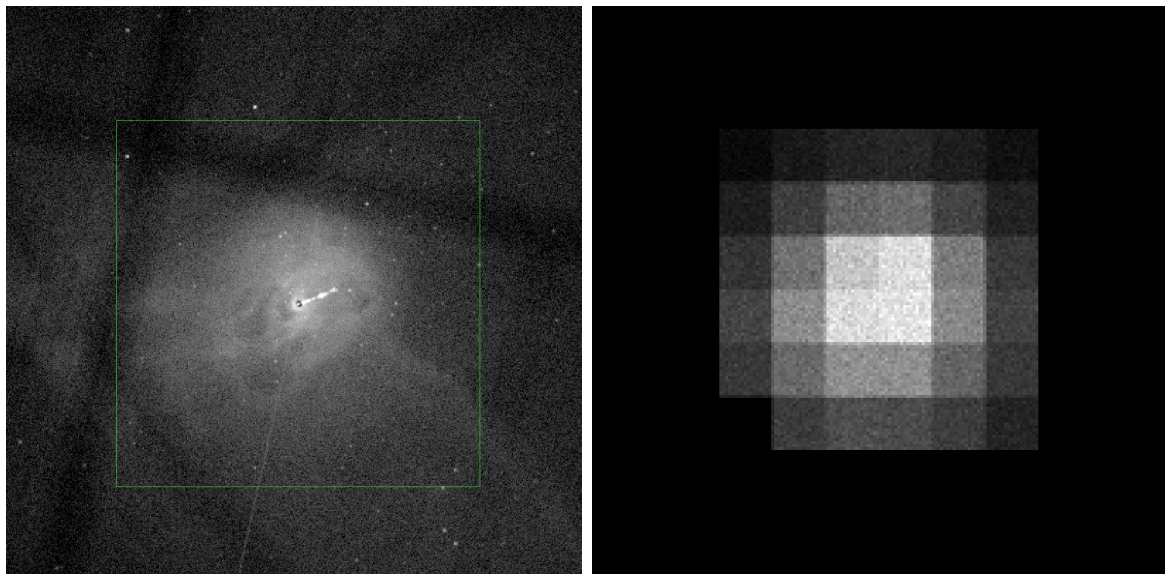


Figure 3.3: The image on the left is a summed image of M87 through CHANDRA data. The image on the right is the physical image produced by simulating a XRISM Resolve image of the M87 cluster. There are 6x6 major pixels shown with the orientation pixel (pixel 9) removed in the bottom left of the simulation.

Shown in Fig. 3.3 the image resolution of XRISM’s Resolve instrument is poor. Due to this XRISM data cannot be extracted in tight concentric annuli as was seen in the CHANDRA data. While you can partition the simulated image into 3 “circular” regions, this will lose the capability of observing smaller structures, including some structures found in the core. One method of obtaining full radial profiles would be to take multiple exposures with the telescope pointing being moved radially outwards from the core. This would create larger radial profiles but will continue to have large radial errors on points in the profile. Proposing multiple exposures, particularly into the dimmer non-core regions of the cluster will use a large amount of instrument time. This may lead to proposals being denied early into the launch cycle of a new telescope. Radial profiles will not be tested and created, only clusters with significant features outside of the core of the cluster will have simulations of extra regions to observe. Since these pointings will be offset from the core this is expected that they require a significantly longer exposure time. If a cluster’s core is too dim then it is unlikely that interesting offset structures may be observed within the allotted observation limits of the XRISM mission.

3.3 Selecting Clusters

The selection of clusters is controlled by the limitations of the instruments available on the XRISM mission. Early Cycle 1 proposals have observation time limited to 200ks. This limit was in place before the gate valve opening failure was known, therefore clusters must have clear characteristic X-ray lines within 200ks to be selected. Each simulation was produced with an exposure time of 200ks as the upper limit. Photon counts may then on average be linearly scaled by changes to exposure time, thus an image with 100ks exposure time should have half the counts of a 200ks simulated exposure.

There is a list of known clusters that have already been selected as early release data, some of the clusters that appear on this extensive list are: A426 (Perseus), A2029, Centaurus, Coma and M87. Therefore clusters that are already on this list do not need to be simulated as their early proposals have already gone through. This allows for any other cluster within the datasheets to be simulated and tested to see if it is a candidate for an observation proposal. The baseline for cluster candidates is to have enough Fe-K photons to observe Doppler broadening within the central pointing of a cluster. After testing, 150 non-continuum photons in the He- α Fe-K resonant scattering line is the lower limit to model the Fe-K line. Below 150 photons the signal-to-noise ratio drops significantly and errors in modelling the turbulent velocity broadening increase. If the cluster contains interesting physical features found in offset pointings they will be also tested as separate exposures. The Fe-K complex is selected since it has a high signal-to-noise ratio and stands out within the spectrum. This complex also is located at the least affected region through the gate valve, as the 6-7 keV range is at a high enough energy that it is only weakly attenuated. This creates flexibility in producing proposals as the criteria for selecting these clusters do not change significantly if the gate valve is opened in-between proposal submission and the time of observation. The Fe-K complex was also selected due to the Fe-K He- α w-line being a thin resonant scattering line, this line being bright and thin allows for a high accuracy results through modelling the turbulent velocity broadening. The process in counting photons is similar to the XRISM region data analysis done in Chapter 2. The total amount of photons taken on the smallest bin on either side of the Fe-K complex ($\sim 0.5\text{eV}$) was extracted then the slope between the two bins was interpolated, creating a background continuum photon count. This background continuum count was removed from the total Fe-K region, the residuals then represent the emitted photons from the Fe-K characteristic lines. The photon count errors are produced by Xspec.

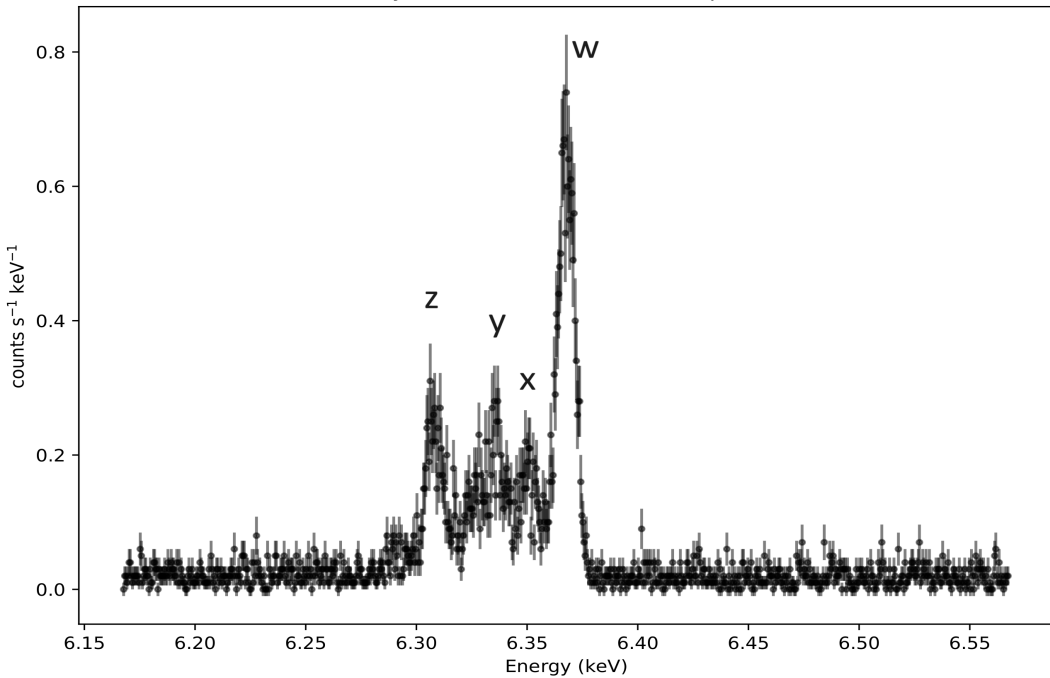


Figure 3.4: A snapshot of a simulated HydraA spectrum focused on the Fe-K complex. The major lines are labelled here from w to z, with w representing the bright He-alpha like resonant scattering line Fe XXV $7 \rightarrow 1$. The other major peaks labelled are also transitions in Fe XXV, $6 \rightarrow 1$, $5 \rightarrow 1$ and $2 \rightarrow 1$ respectively. There are other weaker lines found within this complex, such as high energy level H-like (Fe XXIV) lines that may broaden the brighter He-like lines. [6, 34]

Each selected cluster was tested w-line photon counts with different turbulent velocity values in each simulation, a range between $100 \frac{km}{s}$ to $2000 \frac{km}{s}$ dependent on the selected cluster. The reason these photon counts are recounted is due to the line broadening, the broadening characteristic lines lower the amount of counts per energy bin but increase the bins that the characteristic line represents. This broadening can lower the signal-to-noise ratio of the Fe-K complex and thus causes photons from the characteristic line to appear as background x-ray continuum photons. As it is difficult to disentangle these photons from the background continuum photons, the overall confident count within the Fe-K complex and He- α w-line will fluctuate. Initially the expected result would be a decrease in counts in the Fe-K complex, but properly outlining the complex could see gains from photons by other dim lines around the complex, or losses as a photon may appear as if it was from the background continuum.

When a cluster is found to fit the photon count requirement said it is then marked for study, and the datasheets from Chapter 2 are used to further assist in finding more clusters. This comes from the “Flux” and the “Iron Flux” values in the datasheets. Since these are values obtained from the Fe-K region in the spectrum of the CHANDRA image, using this as a baseline it was found that MS07 is a suitable dim candidate for a central pointing simulation. All clusters that produce photon counts in the Fe-K region that are greater than MS07 can also be used for simulation testing. The clusters that were selected that achieved this value were: A2199 and HydraA. These clusters, in addition to MS07, are candidate clusters to create XRISM A01 proposals. Each of these 3 clusters are tested for the ability to observe particular velocity broadening effects, with each testing multiple turbulent velocities in simulations. HydraA will be tested with two pointings, as dim outer shock fronts provides enough Fe-K photons to test in simulated observations. If HydraA’s offset pointing can produce more than 150 photon counts then it will be determined as usable pointing for the proposal. Future clusters that may be added in addition to this work can be HerculesA and A1835. These clusters were tested to see how many Fe-K photon counts can be found, which were near MS07 counts (HerculesA) or well beyond them (A1835).

CygnusA was a cluster that fit the criteria for being a XRISM A01 observation candidate, but it was known that another team under Timothy Heckman is attempting to produce their own proposal with this cluster. Thus CygnusA was simulated but instead used as a cluster to test velocity broadening modelling. CygnusA is a bright and powerful cluster, having the highest Fe-K flux count of clusters not already selected within the datasheets, as shown on Table 2.3. The Fe-K complex of CygnusA is more defined than dimmer clusters and can be used as a baseline for a high photon count cluster, it may also show the effects of altering exposure time when generating simulations of these clusters. As seen in Table 3.1 CygnusA exceeds beyond the proposal luminosity threshold by 16x the minimum photon counts with the maximum exposure time of 200ks. This cluster is a great candidate cluster as it will require less than 20ks to obtain enough information to extract the turbulent broadening component of its ICM.

Cluster Data				
Cluster	Simulated Vturb (km/s)	Temperature (kT)	Net He- α Fe-K Counts	He- α Bkg Counts
HydraA	100	3.64	1281	23
	200	3.64	1223	42
	300	3.64	1194	70
	600	3.64	1065	93
MS07	100	5.14	251	38
	200	5.14	289	24
	300	5.14	283	45
	600	5.14	332	60
CygnusA	100	6.84	4041	450
	200	6.84	4273	448
	300	6.84	4852	500
A2199	100	3.52	1375	209
	200	3.52	1369	271
	300	3.52	1637	297
<i>HydraA_N</i>	100	3.93	131	23
	200	3.93	152	39
	300	3.93	154	40
	600	3.93	184	70

Table 3.1: Each cluster was simulated with 200ks exposure time. Fluctuations in the He- α counts occur due to the line's edges convolving with the rest of the complex. Photon counts in simulations with lower Vturb have a higher confidence value.

3.3.1 HydraA

HydraA contains one of the strongest FR-1 radio sources found in a galaxy cluster. The classification FR-1 defines that the radio luminosity is brightest to the center of the emitting source with the jet lobes appearing as the dimmest portion of the structure. Due to this the jet has been measured thoroughly in radio, allowing for a precise measurement of jet power. The jet power is on the magnitude of $\sim 10^{61}$ ergs or $\sim 2 \times 10^{45} \frac{\text{ergs}}{\text{s}}$ [72, 83, 113]. These calculations were done by observing the shockfronts of the cavities produced by the AGN such as the large cavities found 200-300 kpc away from the center of the cluster.

The physical structure of this cluster is complex, driving another reason to observe HydraA, as there are 3 pairs of cavities being produced by the strong AGN. These cavities show an oscillation of the AGN, appearing as a chain of 3 cavities at different cluster radii and sizes. Due to the orientation in the sky and the brightness of the cluster this allows for the characteristics of the cavities to be easily quantifiable (energy, speed and volume). Through the size of the cavities, especially the outer pair, they may actually be spatially resolved through XRISM's Resolve instrument. Further science may be done by comparing the motion and metallicity within the cavity to the turbulence of the surrounding ICM atmosphere. This allows for a clearer comparison between jet kinetic energy and the surrounding atmospheric kinetic energy. By using an extended exposure through the 3 pairs of cavities within the cluster measurements of both bulk motion and turbulent velocity of hot and cool gas may be observed over large structures in HydraA. While the cluster is good candidate for XRISM observations it will need at least two different exposures taken at different regions. Initially the idea was to overlap the exposures over the center of the cluster while capturing the outer cavities, but this does not fully capture the edge of the outer cavities and created issues with photon mixing affecting the photon count criteria. Therefore the method that should be done is to have a central pointing of the cluster that can capture the central two pairs of cavities, and a northern pointing that can capture one of the larger cavities fully within its field of view. Due to the radial decrease in luminosity of cool core clusters the central pointing would be expected to contain more counts within the Fe-K w-line than the northern pointing. This prediction turns out to be true as the simulations of HydraA's center pointing on average have 1200 counts in the Fe-K w-line, while the north pointing barely fits the requirement, having ~ 150 counts in the Fe-K w-line. This means that the central pointing can have its exposure decreased from 200ks to 100ks with no issues, while the north must be 200ks or greater.

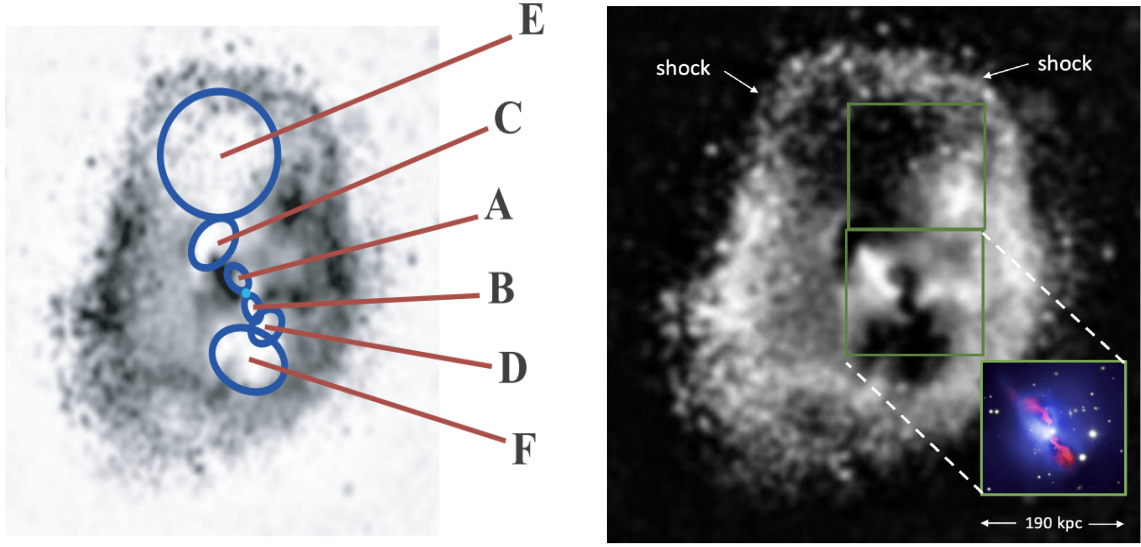


Figure 3.5: An example of HydraA’s cavity locations and the two proposed exposures of the galaxy cluster. This shows that the center pointing covers the pair of cavities labelled A, B and D fully, with C and F having a majority of their structure within the FoV. The second north pointing observes the surrounding shock of the largest cavity E. Image provided by [113].

Churned motion within the centers of galaxy clusters have been found to have an average turbulent velocity broadening of $\sim 150 \frac{\text{km}}{\text{s}}$, with most clusters having this range being between $100\text{-}300 \frac{\text{km}}{\text{s}}$ [38]. This value has been found to extend upwards to $800 \frac{\text{km}}{\text{s}}$, but only in a few rare cases. This implies that the cluster’s central pointing should be simulated with a turbulent broadening component between 100 and $300 \frac{\text{km}}{\text{s}}$ to output a spectrum that is as close as the expected spectrum from XRISM. A $600 \frac{\text{km}}{\text{s}}$ simulation is included in the case that this cluster has a higher broadening than expected. The northern pointing of the cluster contains a 210 kpc wide cavity, the radius and expansion speed of the cavity should correlate to the motion of the surrounding shock front through work being done on the surrounding environment. This predicts that the motion of the surrounding gas should be between $300\text{-}600 \frac{\text{km}}{\text{s}}$. With this range two simulations may be made, using the minimum and maximum values to observe the accuracy in which our models may observe turbulent velocity broadening on a spectrum.

3.3.2 MS07

MS07, much like HydraA, was selected due to the strength of the jets within the cluster, as it is considered to contain an incredibly strong FR-1 radio source. Being a strong jet allows for a refined look into the conversion between jet kinetic energy and churned kinetic energy in the atmosphere. The large inner cavities of the cluster have been measured to have injected a total of $\sim 10^{61}$ ergs [92]. MS07 was selected to be a candidate cluster due to these cavities, as they are large enough to possibly be spatially resolved using XRISM's Resolve instrument, and most importantly they have documented jet energies. These components will allow for a simple process of defining the rate at which jet kinetic energy affects the mixing of the surrounding atmosphere. Beyond turbulence of the ICM using XRISM to observe this cluster may lead to more information of the bulk velocities of hot and cold gas. This can be done through extracting multiple subsections of the cluster which could be used to observe cooling flows and other structural components within MS07.

As the angular size of the brighter core of the cluster fits nearly into the 2.9×2.9 arcminute footprint of XRISM's Resolve instrument, the only pointing that would produce enough photons would be centered on the cluster's core. This central pointing will contain a giant pair of 200 kpc wide cavities and will observe the strong shock front at the edges of the cool core. The cavity radius is expected to scale with this shock front, expanding the cavities at a rate of $\sim 500 \frac{km}{s}$. This would cause the surrounding atmosphere to show a similar turbulent broadening component. The expected max speed is around $600 \frac{km}{s}$ while the central regions are expected to show values around $300 \frac{km}{s}$. This means that simulations must be made by testing the photon counts and velocity dispersion between these two values. This is similar to HydraA's northern pointing which encapsulates a cavity of a similar physical size. Two simulations were made observing the maximum and minimum expected turbulent broadening values. MS07's central exposure was selected to have 200ks of exposure time as in both variants of the simulation the Fe-K w-line emits 300 ± 32 photon counts. This can be lowered to 100ks at the upper end of photon counts, but having a longer exposure time lowers the noise surrounding the Fe-K line, thus providing a clearer measurement of velocity dispersion.

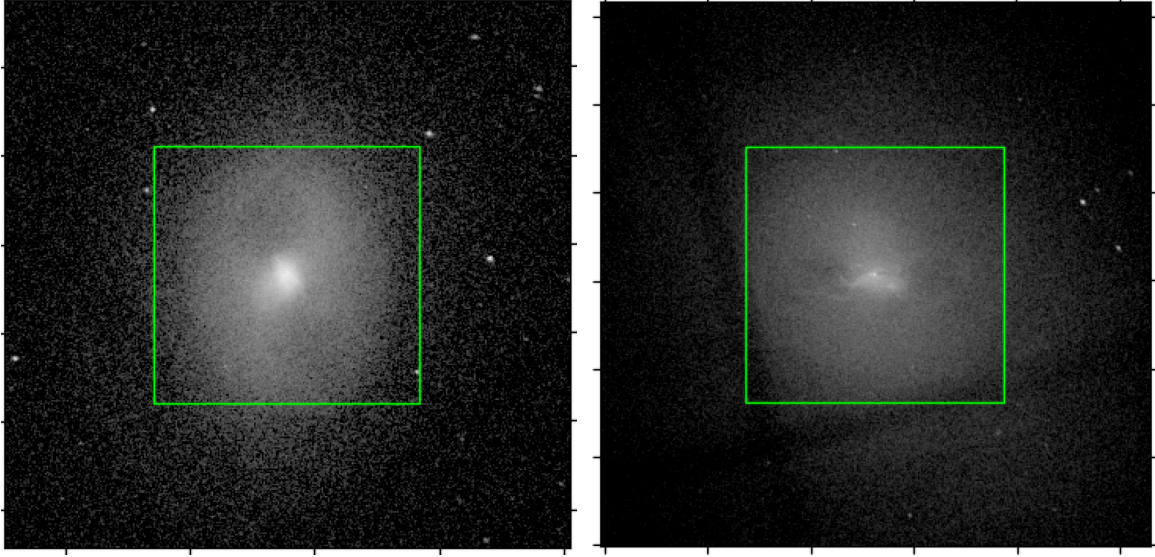


Figure 3.6: Unsmoothed CHANDRA images representing the suggested pointings of XRISM for both MS07 and A2199. Both have central single pointings with a pair of large cavities located within each pointing. MS07 is pictured on the left, A2199 is pictured on the right.

3.3.3 A2199

A2199 is a cluster with a medium power radio source in the center, and with it being one of the brightest clusters in X-ray emissions it is a good candidate cluster to observe with XRISM. A2199's AGN is considered a medium strength radio source as in comparison to MS07's jet power of $\sim 10^{46} \frac{\text{ergs}}{\text{s}}$ its jet power is $\sim 10^{42} \frac{\text{ergs}}{\text{s}}$ [92, 84]. Observing a weaker jet is important as MS07 and HydraA are outliers, having extremely strong jets, meanwhile observing A2199 may provide data akin to a common galaxy cluster. A2199 was selected to have 1 pointing centered at the core of the cluster, as surrounding structures are too dim to obtain useful data. Within this center pointing the large pair of cavities are both fully encapsulated, through this the expected turbulence should be similar to the centers most common clusters, the range being from $100 - 300 \frac{\text{km}}{\text{s}}$ [38]. Simulations were made using the minimum and maximum value within this range, and on average ~ 1400 counts within the Fe-K w-line were observed with 200ks of exposure. The exposure time can be lowered to 50ks and still observe over 300 photon counts in the Fe-K w-line. This lowered exposure time can obtain the proper turbulent velocity broadening component within the spectral line.

3.4 Modelling Broadening

The goal of this chapter is to observe the kinetic energy being injected into the surrounding ICM by radio jets; this means that simulations must be produced with injected turbulent velocity broadening. This injected velocity is considered the true value of the spectrum, models are tested to see how accurate they are in extracting this value. This process can be done over the broadband spectrum but may cause larger errors and add extra inaccuracies produced by low strength spectral lines. To mitigate this source of error modelling was only done on the narrowband Fe-K complex located between 6-7 keV. It must be noted that different redshifts will shift the Fe-K complex to be less than 6.7 keV. As seen in Fig. 3.4 the Fe-K complex is comprised of multiple different He-like Fe (Fe XXV) lines: the w-line, a resonance line, the z-line, a forbidden line and the x and y lines, two intercombination lines [6]. There are photons from other lines under this complex which do affect the lines above, but their emissivity is substantially weaker than the w-line. This may cause the other three major lines to appear broadened, which can overestimate the effect of turbulent broadening. This leads to the w-line driving the model's calculation of turbulent broadening.

Observations over the 6-7 keV band may include photons from the H-like Fe lines (Fe XXVI), as there is a doublet located near 6.9 keV. This doublet is cropped out of the narrowband to further remove inaccuracies to the modelling software. This cropping process is done initially on the simulation with the highest injected turbulence as this would broaden the H-like Fe the most, this limit was then kept for each simulation of the same exposure to not alter models.

This leads to a system where only the w-line in the Fe-K complex is modelled with the nearby doublet removed. To model the effect of turbulent broadening the width of the spectral line must be broken down into components. There are three Gaussian broadening components, thermal Doppler broadening, instrumental broadening and turbulent broadening. To calculate the turbulent broadening component the other two components must be calculated, this is easily done as thermal broadening requires the temperature off the gas and the mass of the ion whilst the instrument broadening is equivalent to the spectral resolution limits of the instrument used. As such the full linewidths of each component may be calculated and subtracted from the full linewidth of the Fe-K w-line. Since this is equivalent to three stacked Gaussians the turbulent broadening component should equate to the residual linewidth, which is then converted into a velocity value. As such the equations for obtaining each component is shown below:

$$\sigma_{\text{therm}} = \sqrt{\frac{kT}{m_{\text{ion}}}} \quad (3.1)$$

$$\sigma_{\text{inst}} = \frac{5eV}{2\sqrt{2 \ln 2}} \quad (3.2)$$

$$\sigma_{\text{turb}} = \sqrt{\sigma_{\text{total}}^2 - \sigma_{\text{therm}}^2 - \sigma_{\text{inst}}^2} \quad (3.3)$$

kT is defined as the temperature of the cluster, for simulations this value is provided by the datasheets of the cluster itself and m_{ion} is the mass of an electron. In the instrumental standard deviation the estimated FWHM of XRISM is considered to be 5eV and thus is used for the instrumental broadening calculation. Thus by editing a script produced by a previous graduate student within the research team, Prathamesh Tamhane, this calculation was done upon the Fe-K w-line. The w-line is automatically centered near a given energy and the turbulent velocity broadening is calculated by subtracting the other modelled components off of the linewidth. This modelling process was attempted in two different methods, the first being only modelling the Fe-K w-line while ignoring the rest of the complex, the other was applying similar models onto each spectral line within the complex and extracting the average velocity width of those. The latter contains multiple issues as there are 4 main Fe XXV lines in the complex, 6 total high emissivity lines spanning from Fe XXIII to Fe XXV and over 110 total characteristic spectral lines, many with low emissivities that can still affect the shape of the Fe-K complex [34]. This causes issues as a model with too many components may fail to fit, and provide unrealistic velocities in the other characteristic lines. Therefore only the He-like w-line was fitted and observed to define the turbulent broadening of a cluster.

There is a fourth component, the natural line width, is a broadening feature caused by the uncertainty principle, in which the transition between photon states is not perfectly at one energy and may shift up or down by a small offset. This component appears as a Lorentzian function, this fact caused errors within the modelling software and was removed. As it is expected to be the weakest component within the model it should have little impact on the turbulent broadening calculation due to its inclusion or removal. Future work may require another look into natural line widths to test if their impact on broadening calculations is significant, especially if instrumental spectral resolution reaches ~ 1 eV.

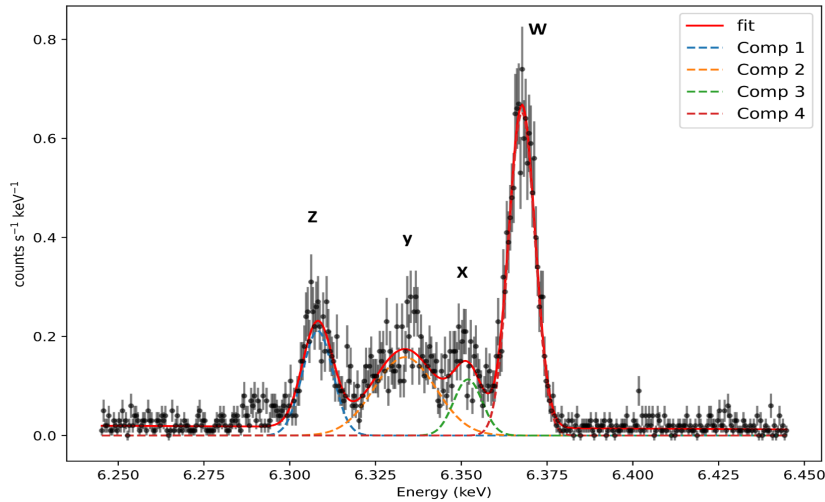


Figure 3.7: A model of HydraA with 200ks exposure time and 100 km/s turbulent velocity. The model contains the Fe-K complex with 4 components that relate to the 4 main He-like Fe spectral lines. This and another model with 6 lines were attempted. This model provides broadening velocities on each line, producing unphysical results for the y and x-line.

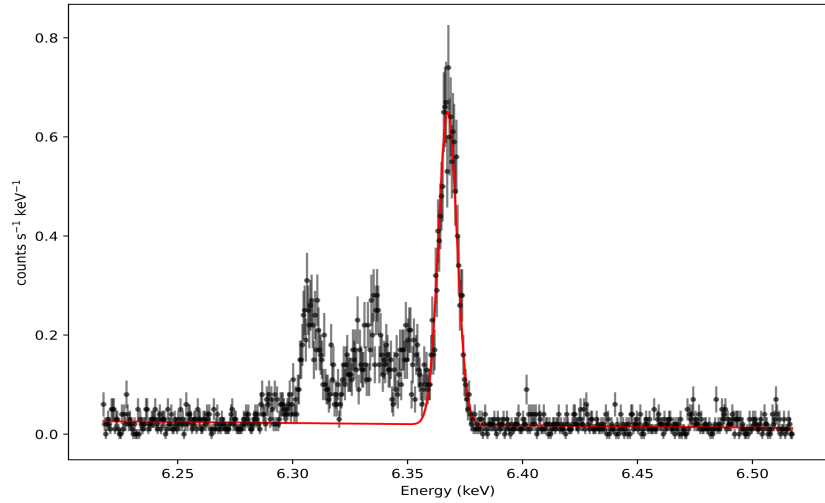


Figure 3.8: A single fit model on the same simulation, the bounds on the x-axis have changed to include more continuum. This will be used as the standard for fitting the w-line for future simulations.

These self made models were also tested with Xspec models, a `TBabs*bapec` model was selected. It uses the given hydrogen density, redshift and temperature found from the datasheets produced in Chapter 2. This means that the abundance, normalization and velocity broadening are left as free parameters for the model. This was done to observe the differences between the two models, as `TBabs*bapec` uses the entirety of AtomDB on the spectrum, counting all of the different lines within the Fe-K complex. It is expected that models would be more accurate on systems with higher photon counts as this increases the signal-to-noise ratio, allowing the model to properly define a spectral line. SPEX was considered to be used as a method of testing this broadening effect, but early XRISM work appears to be standardizing the usage of Xspec for modelling.

Modelled Velocity Broadening Features						
Cluster	Simulated Vturb (km/s)	Modelled Vturb (km/s)	Modelled Vturb Error	Xspec Vturb (km/s)	Xspec Vturb Error	Fe-K w-line Counts
HydraA	100	99	7	101	9	640
	300	268	16	280	16	597
	600	609	52	584	33	532
HydraA _N	300	337	30	259	29	154
	600	1080	135	482	63	184
MS07	100	97	19	107	16	283
	300	366	32	303	25	324
A2199	100	104	7	120	6	687
	300	279	13	289	9	742

Table 3.2: A comparison between the injected turbulent velocity and the values that different models obtain from simulated data. The two models used were a scripted model, labelled as ‘Modelled’ in the table, and Xspec’s `TBabs*apc` model. The w-line counts were calculated by observing the photon counts within a narrowband where there was a clear drop in emissivity on both ends.

The data shows that both models appear to be close to the true value in lower velocity systems, with the scripted model being within 1σ for most $100 \frac{km}{s}$ systems. Clusters with lower w-line photon counts cause the models to struggle with obtaining the true velocity broadening value, as can be seen in all of HydraA's north pointing models. It is expected that the model would struggle to obtain the correct value with a high velocity low photon count spectrum such as the HydraA North pointing with $600 \frac{km}{s}$. This occurs because the Fe-K complex contains multiple spectral lines with similar energies causing the lines to broaden into each other, deforming the shape of the complex, and causing photons from other Fe-K XXIII-XXVI transitions to appear as w-line photons (and vice versa). At greater velocities it is expected that the single Gaussian model will overestimate the velocity broadening component as it begins to include the x and y-line into the single Gaussian, this explains the $\sim 400 \frac{km}{s}$ overestimation with larger error bars than the Xspec model. The Xspec model should account for multiple lines within the complex and thus should be accurate in obtaining the initial injected turbulent velocity. Yet it appears that Xspec slightly underestimates the velocity broadening of most of the high velocity simulations. This table shows that both models appear to be accurate ($1 - 2\sigma$) at gauging the proper turbulent velocity broadening within a spectrum. As was expected the 150 photon limit in the Fe-K w-line proves as a good requirement to extract a clear value but this requires a more relaxed cluster to use the non-Xspec model. This also shows that early XRISM data, as long as the gate valve is closed and the exposure time is limited, will have to be biased towards big bright sources or slow moving dim clusters, as longer exposures may be needed for dimmer faster objects.

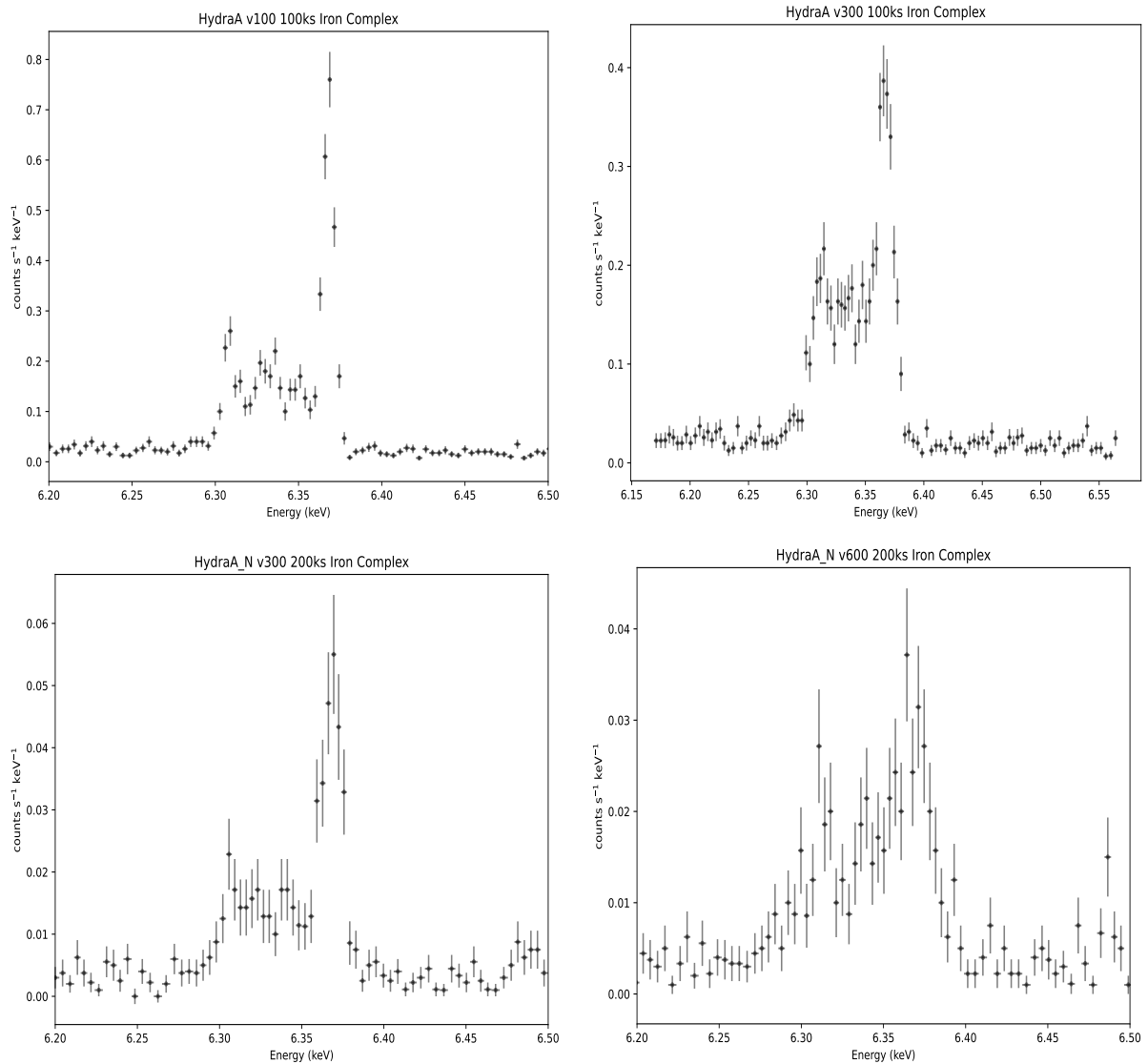


Figure 3.9: Four out of five binned HydraA simulations referenced in 3.4, the upper two figures are central pointing simulations, the lower two are the north pointing. The y-axis represents the counts per second and does change between the figures, thus higher turbulent figures have broader lines and dimmer totals. This showcases the difficulty in obtaining a proper broadening value at higher velocities as the w-line becomes less and less distinct.

3.5 Conclusions & Proposal Outcomes

The rate in which AGN radio jet energy converts into the kinetic energy of the surrounding ICM is still considered unsolved. As such XRISM's high spectral resolution instrument (Resolve) will be used to observe the motions of the X-ray emitting gas. To be able to find a relationship between these two components a large dataset of multiple clusters must be made with accurate velocity measurements in the surrounding ICM. To achieve this with a new instrument the cluster selection must go through a proposal process to obtain any instrument time. As expected a proposal with a large dataset of clusters would take too much instrument time, therefore three specific clusters were selected as an initial batch for the first open cycle of proposals.

These three clusters: HydraA, MS07 and A2199, were selected due to their known jet power and X-ray luminosity. The bright luminosity allows for a lower instrument time required to obtain enough photons to observe the effects of turbulent velocity broadening on spectral lines. HydraA emits enough in X-ray photons that an offset northern pointing was added to the proposal. To prove that these are useful clusters to observe they must be simulated and modelled. This process was done by upscaling the spectral resolution of CHANDRA data (from 95eV to 5eV) and producing a simulation of the data with different exposure times and different turbulent broadening speeds. The Fe-K complex of the simulated spectra is then modelled to observe if the models can accurately extract the injected turbulent broadening component. Two different models were used to test if this value can be extracted, the first model being an Xspec `TBabs*apec` model while the second being an internal `lm_fit` model extracting the three major broadening components of a spectral line. The `lm_fit` model only observed the bright resonant scattering Fe-K line due to its emissivity in comparison to the other spectral lines in the complex.

The models were tested on at least two simulations per cluster pointing, each simulation was defined by the expected range of turbulent motion within the ICM, with the simulations representing the maximum and minimum expected turbulent broadening. With HydraA having two pointings, central and north, separate sets of simulations were done for each. Prior to modelling these clusters it was expected that pointings with an overall lower photon count (HydraA north and MS07) and simulations with a higher injected broadening would both cause the accuracy of the models to decrease. This is because the Fe-K resonance line would be less defined in both cases, and as it is the main line in the complex that both models obtain the linewidth from the measured turbulent velocity component decreases in accuracy. Between these two models a trend seems to appear, wherein the `lm_fit` model appears more accurate than the Xspec model at low simulated velocities. This is seen in A2199's $100 \frac{km}{s}$ and HydraA_N's $300 \frac{km}{s}$ models where the `lm_fit` model extracted $104 \pm 7 \frac{km}{s}$

and $337 \pm 30 \frac{km}{s}$ respectively. Using Xspec both measurements were well out of range of the 1σ error given by the model. When observing systems with the maximum expected turbulent velocity the Xspec model is consistently within 1 or 2σ of the true value while the lm_fit model is not. The inaccuracies of both models appear to increase as the total number of photons decrease, as seen on the HydraA_N pointing. Even so it consistently shows that using the lm_fit model is better for low velocity regions in clusters while Xspec should be used for high velocity regions in clusters. Since most of the injected values have been extracted within $1-2\sigma$ error we have showcased the ability for models to be accurate in obtaining this data.

Each cluster is packaged in a separate proposal, each with different exposure times for differing pointings: MS07 at 200ks, HydraA at 100ks, HydraA_N at 200ks and A2199 at 50ks. Each proposal is under the total limit of 600ks per cluster and 300ks per pointing, which was done to increase the success rate of the proposal. These proposals were observed and graded in a rate of priority, with A2199 approved with an A rank under a different principle investigator, HydraA's central pointing was approved with a B rank and its north pointing was given a C rank with both having Brian McNamara as the principle investigator. Unfortunately MS07 was not put in the A01 Cycle approval list and will require another proposal in the next cycle. The HydraA proposal was successful in showing that important data can be extracted from its pointings as it was approved and will be expected to produce data in the first quarter of 2025. Other researchers within the team may join the A2199 team being lead by Francois Mernier. The priority ranking system defines if an observation will be completed, with A and B priority targets being eligible for funding immediately while the C rank priority has a 20% chance of being completed. By definition HydraA will get its central pointing completed, and with the chance of the north pointing being taken as well. This was beyond expectations since modelling high speed turbulence in the north pointing was beyond a 1σ error.

Both HydraA and A2199 will be observed and added to the database of clusters. This database will be used to calculate the conversion of energy between radio jet power to the turbulent gas motions in the hot atmospheres of galaxy clusters. These clusters will be added to the data obtained from early XRISM target clusters such as M87, Perseus and A2029.

3.6 Future Work

As XRISM's mission length is targeted to be 3 years this process of finding good candidate clusters must be repeated throughout the mission's lifespan. These simulations must be made to observe if the luminosity of the Fe-K complex in clusters will be able to accurately measure the turbulent velocity broadening. If the gate valve opens this will increase the photon count in the Fe-K complex and can allow the usage other major lines, like the Fe-L complex or bright Si lines, as another method calculating the turbulent broadening within the cluster.

The lm_fit model itself may require an update, the time constraints of the A01 cycle of proposals the model did not account for the natural line width of each Fe-K line. This needs to be studied to observe if there is a substantial effect adding the natural line width to the final turbulent velocity. Finally the lm_fit model requires adjustments to map out the other Fe-K lines within the complex, as previous iterations showed failures when attempting to model the complex in high turbulent velocity systems. This may be the reason as to why it lost accuracy in systems with higher speeds in comparison to the Xspec model.

Chapter 4

XRISM: A Study of M87's Intracluster Medium

To get a clearer view of the motions and composition of M87's intracluster medium XRISM's early performance verification data was used. XRISM is a telescope at the forefront of X-ray astronomy. The spectrum produced by M87 reveals emission lines of different metals with high spectral resolution through XRISM's microcalorimeter. This process provides the abundance, turbulent extrathermal velocities and bulk motion of each separate metal. Through this separation in metals key observations in the motions of hot and cool gas may be made. Hot and cool gas have different motions in the cluster, hinting at a different relationship between them and the injected kinetic energy of AGN jets. Due to the multiple available exposures of M87, radial and structural information may be extracted from this data. The exposures do not only focus on the center of the cluster, but extended arms, cavities and shock fronts too. Each component leads to uncovering the formation and evolution history of this galaxy cluster.

This chapter includes original research, using early access data from XRISM's first light, in particular from the M87 team headed by Aurora Simionescu. All the X-ray data within this chapter was analyzed and produced by Neo Dizdar unless stated otherwise. As this chapter discusses data that is a current work in progress within internal teams results may change before the paper is published.

4.1 M87

M87 is the brightest central galaxy found within the Virgo Cluster, located in the Virgo A subclump. The Virgo Cluster and M87 are objects that have caught the eye of the public in recent years due to the imaging of M87’s central black hole by the Event Horizon Telescope Collaboration [1]. M87 itself has been continually under the eye of multiple research teams, being one of the first extragalactic objects observed emitting X-rays, its close proximity with a redshift of 0.004283, and its large and distinct radio jets [100, 112, 47]. As such many different telescopes have observed M87 with different bandpasses, this includes CHANDRA, XMM-Newton and the Einstein Observatory.

M87 hosts a Fanaroff-Riley 1 (FR-1) radio source. The centermost portion of the jet contains synchrotron “knots”. These knots appear as brighter X-ray regions next to the AGN, all extending radially away from the center. This unfortunately cannot be resolved structurally in XRISM’s microcalorimeter as this structure is smaller than the pixels of the instrument (below 30 arcsec or 2.6 kpc). This means that XRISM has to observe larger structures in the ICM, such as the two extended arms following the extended radio jets that appear structurally different in the X-ray spectrum, these are considered to be the south-west and east arms. Four pointings were observed in with their footprints shown in Figure 4.1, centered on the core of the cluster, the south-west and east arms containing bright metal-rich outflows and the fourth centered on a shock front in the north-west. This fourth exposure should show a region with the lowest turbulent velocity but in tandem has the lowest luminosity which can cause issues with modelling the broadening components as was shown in Chapter 3.

Similarly to the selection criteria of the proposals in the previous chapter, M87 was selected due to its jet power, which is $8 \times 10^{42} \frac{\text{ergs}}{\text{s}}$ [33]. This jet power is expected to be comparable to the kinetic energy of the surrounding ICM.

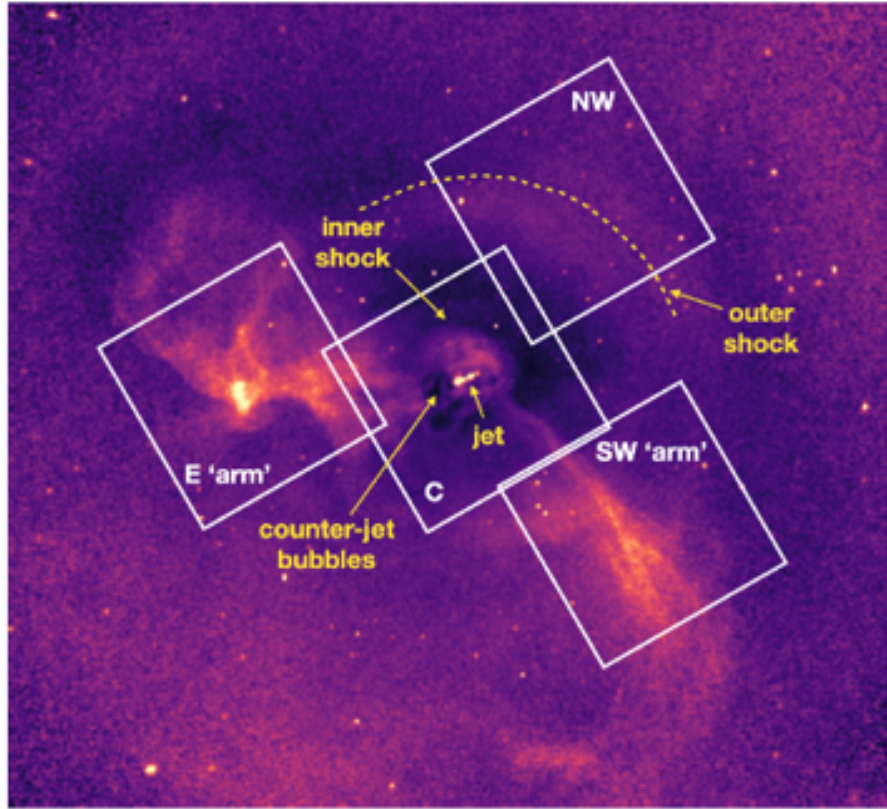


Figure 4.1: The four separate pointings of the early access data in for M87. Each pointing was selected to observe different components within the cluster: two dense arms in the surrounding ICM, a slow moving shock front and the central region of the cluster. As is expected the exposure time will vary between pointings, and some pointings will take multiple exposures which will be stacked to produce a long exposure shot. The south-west arm is currently missing an exposure, the second is slotted for early 2025 and thus only has a single 70ks spectrum taken. Image shown is produced by CHANDRA.

4.2 Data Extraction

The XRISM data is composed of 5 separate exposures ranging from 80 - 180ks. Two exposures of the north-west shockfront were added together and reformatted in a single file. The extracted spectral data relates counts to energy channels. These energy channels are converted to electron volts by using a provided response matrix function (rmf) which translates a channel to a unit of energy. Each pointing has a separate rmf and arf associated with the data.

The ancillary response file (arf) defines the weighting of photons on each pixel, accounting for vignetting and failing pixels. Pixels may be removed to removing regions in an exposure to focus on specific extended structures. For example, on the north-west pointing it can roughly separate the inner and outer shock, allowing each component to be studied separately. Arfs must be defined before reading in and calculating the data, as issues with gain histories on pixels may create artifacts.

Pixel 12, the orientation pixel, is turned off. As the XRISM teams study more data over the year more exposures are showing failures in other pixels. For example, Pixel 27 has been known to have issues with its gain history, as such it has been suggested to be removed from all observations. This lowers the available pixels for observation from 36 to 34 which removes $\sim 6\%$ of the instrument's effective area. It is expected that this trend will continue over longer periods of use creating an urgency to get data from the telescope early in the mission. Future proposals must take into account which pixels are faulty and adjust their roll angles to observe key structures. Once the rmf and arf have been convolved with the initial unprocessed data then modelling may be done on the spectrum. The M87 team has created a set of rmfs, arfs and spectral data files to be used mitigating possible sources of error between team members.

4.3 Observing Metals

As the spectral resolution is high in XRISM's Resolve data, unlike previous CHANDRA data, separate observations of different metals within the cluster can be produced. The metals that have visible spectral lines between 1.7 - 10 keV are Si, S, Ca, Ar, Fe and Ni. These can be split into hotter or cooler metals, depending on where a majority of their spectral lines are located, with lower energies representing cooler gas. The cool gas is defined by a narrow bandpass of 2-3 keV, this includes mainly Si and S, while the hot gas is in a narrow bandpass of 6-7 keV which is mainly Fe with some Ni. This means that if there is a clear difference in velocity, turbulent motion or abundance between the

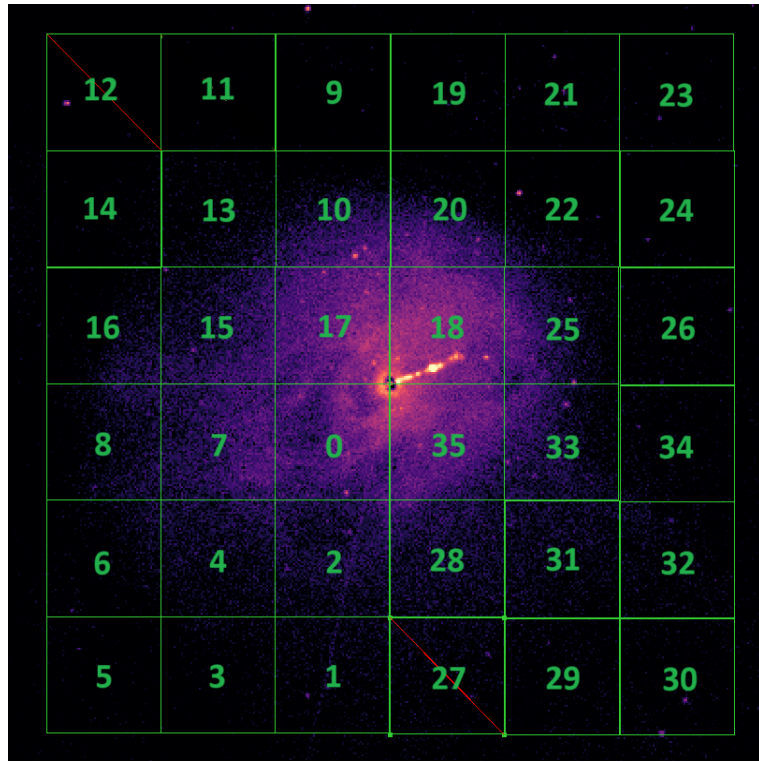


Figure 4.2: This is the format of the pixel names in Resolve, pixel 12 is taken out as an orientation pixel, while 27 is crossed out due to gain history issues. As this is over the centered pointing of a dimmed M87 it can be seen that small structures cannot be resolved with this instrument.

metals representing the two bandpasses it represents differences in the motion of gasses at different temperatures.

Ar is also an important metal to observe as it is the only visible noble gas in Resolve's full bandpass. A noble gas is an important tool to test if the depletion of metals in the cores of certain clusters is a real effect, or that other metals are simply combining with dust particles and not emitting photons. Since noble gasses are inert and will not combine with other particles the Ar abundance should continue increasing towards the core while the rest show a sudden extinction.

While modelling has the capability to obtain separate abundances per metal over a broadband fit applying broadband fits loses information of the motion of metals. Models like `bvape` produce one velocity broadening value and one redshift for the entirety of the single pointing. To observe the motions of specific metals separate models must be made

that cover narrowbands only containing characteristic lines of that metal. Singular metal models are prone to overfitting or adjusting the rest of the cluster’s components (like photon normalization) to unphysical levels. To mitigate overfitting like this an initial broadband fit is done with all abundances, photon normalization, temperature, velocity broadening and redshift left free. Once an initial broadband model is produced then narrowband models are built off of these values, freezing the normalization and other abundances not found in the narrowband. This process is repeated for each metal, leaving their redshift, broadening and specific abundance free to extract a subset of values for each metal. Each narrowband must be defined by a range where characteristic lines of a metal are found, these bounds are found using AtomDB’s database of lines, extending past the characteristic line by 100-150 eV [34]. This extension is to account for clusters with high turbulent velocities or bulk velocity changes, it also assists defining the exact shape of the characteristic line if there is empty “padding” around it. Narrowband limits are shifted by the given redshift of the cluster, and thus the broadband redshift must be calculated by the model first prior to producing the narrowband models. This is done by converting the redshift into a difference in wavelength, then using the photoelectric effect to convert this difference in wavelength to a shift in the eV limits. Repeating over each of the defined metals provides 7 different models, one broadband model and one for each metal: Si, S, Ar, Ca, Fe and Ni. Each model defines 3 important datapoints, the velocity broadening, the bulk velocity and the abundance.

Narrowband Limits ($z = 0$)		
Element	Minimum keV	Maximum keV
S	1.8	2.4
Si	2.4	3.0
Ar	3.0	3.7
Ca	3.7	4.7
Fe	6	7
Ni	7.4	8.2

Table 4.1: Selected narrowband limits that focus on major characteristic lines of each specified metal. Each limit is defined at a redshift of 0, these values scale with redshift changes.

4.4 Model Selection

A single method of modelling clusters should be used as a baseline for all members of the internal M87 research team. Different modelling tools were tested, with the self made `lm_fit` model from Chapter 3 not discussed as it has yet to be used on a full spectrum. The two tools are Xspec, an X-ray fitting package that is developed by NASA’s Heasarc team and SPEX, an X-ray fitting package that is developed by SRON. Both are used for high resolution spectral modelling, but due to differences in models available and databases available it is expected that values between the two packages will differ.

For Xspec the selected model type is the `TBabs*(bvapc+powerlaw)` model, this was done to have separate abundances for each metal and to measure the total broadening of the spectrum. As the AGN adds a non-apec component onto the model, a powerlaw must be added to account for its additional photons. The powerlaw component is scaled by two variables, the photon index and the normalization. Due to known modelling issues between the two components the photon index is fixed at a known value of 2.38, with the normalization left free. As for the `TBabs` model it only requires a hydrogen density value, which is provided by HEASARC’s H column density tool. Most components are dependent on the AGN normalization and `bvapc`’s abundances and velocities. The `bvapc` model has the most free parameters, with the 6 metals, the turbulent broadening, the temperature, the normalization and the redshift of the cluster. One broadband fit was done between 1.7-10 keV, then using the values produced by the broadband and Table 4.1 narrowband limits the narrowband models were produced. For each narrowband the other abundances were frozen, so the model can provide values for the turbulence, temperature and redshift of that metal. The redshift can be used to extrapolate a bulk velocity, obtaining the bulk velocity of the entire cluster and the bulk velocity of specific metals through this process. This model does not yet contain a non-X-ray background component, this should appear as a dim flat model with sporadic peaks, this is not expected to alter the broadening components.

For the SPEX model, the selected model was `reds hot cie` with a powerlaw component to account for AGN emission. The `reds` component defines the redshift of the model and scales the other 3 components. With the initial redshift being defined by the NASA Extragalactic Database’s value of the BCG, the component would be left free to oscillate around 0.004283 [47]. The `hot` component defines the collisional ionization equilibrium absorption model, similar to TBabs wherein a hydrogen column density must be defined and left frozen. The `cie` component defines the emission of gas at collisional ionization equilibrium, similar to the `bvapc` component in the Xspec model. The difference between the two models is that `cie` can define the temperature broadening of a line and can pro-

duce a 2-temperature model. For preliminary testing the models have been constrained to 1-temperature models, this means that the `cie` model must combine the two temperature variables, transforming the 2-T model into a 1-T model. There are multiple abundance tables available to relate the metals to solar values, as a standard within the team the Lodders (2009) abundance table will be used [63]. With the same tables it is still expected that there will be differences output the two models due to the spectral line databases used: AtomDB for Xspec and SPEX's internal database.

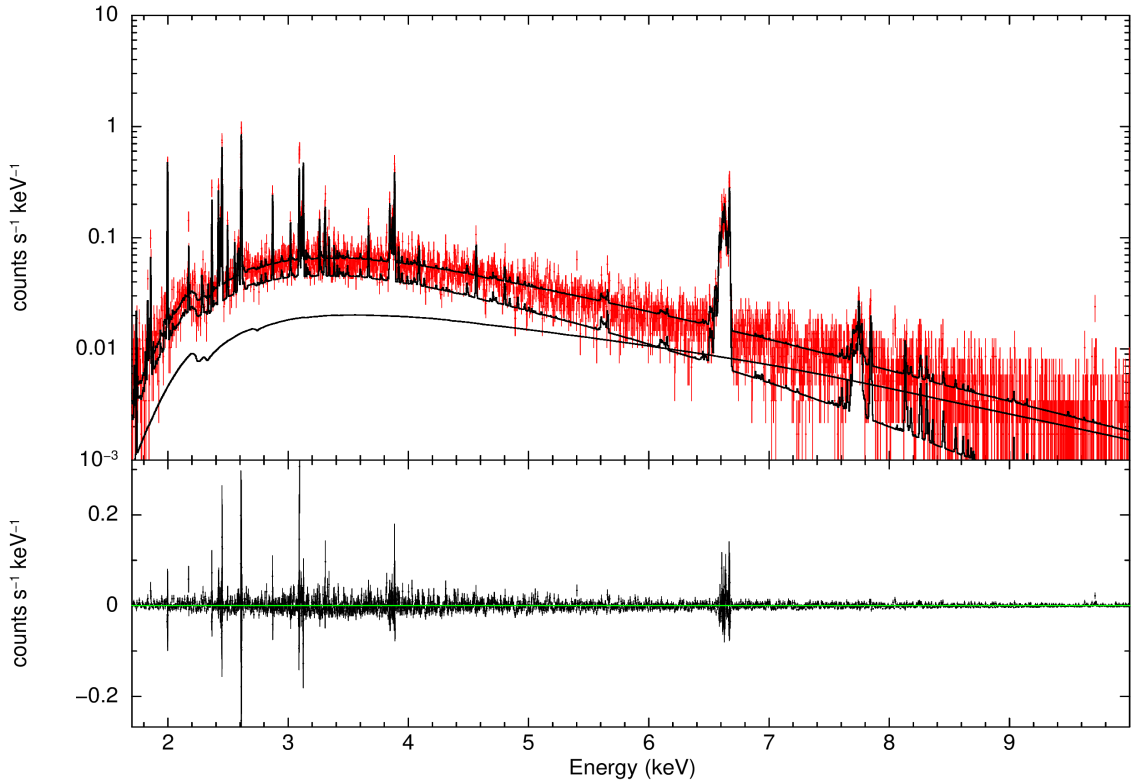


Figure 4.3: The model components of Xspec onto the central pointing of M87. The upper black line is the combination of both components, the lower line with now line features represents the powerlaw component and the `TBabs*bvape` component is the middle black line. The lower graph shows the residual between the model and the spectral data.

4.5 Data Analysis

Post processing data is provided as 5 different exposures, 2 exposures for the north-west pointing and 1 exposure for each other pointing. Each pointing was taken with a different exposure time: 120ks central, 160ks eastern arm, 180ks north-west pointing, and 80ks south-west arm. The south-west arm was expected to have a 150ks exposure but time constraints required a second exposure to be taken in early 2025. The northwestern pointing contains a combination of 2 different exposures, totaling 180ks.

For each pointing several iterations of Xspec and SPEX models were produced. Both created a broadband model containing values for metal abundances, total turbulent broadening, temperature and redshift. This process is repeated using broadband model values as initial conditions and used only on the narrowband limits defined in Table 4.1. The narrowband spectra then would provide data on the motions and abundance of specific metals. Each model is produced by observing the spectrum of the full pointing. Smaller regions within the pointings are not used due to flux limitations and unknown rates of spatial spectral mixing on the new instrument.

The models use Poisson statistics (cstat) to define goodness of fit, producing $1-\sigma$ error bars for: metal abundance, turbulent velocity broadening, temperature, redshift and photon normalization of both the AGN and the gas. Initial tests freed the AGN photon index parameter, but with the freed AGN photon normalization the metal abundances provided were unphysical and removed. Other tests included freeing the temperature in the narrowband fits or freezing it to the broadband fit. This was done to test if freeing the thermal broadening would remove several unphysical values for turbulent broadening in the SPEX model. It was found that both methods provide unphysical turbulence for specific metals with low photon counts, therefore all tests are run with freed temperature and frozen AGN photon index.

Redshift is used to define the bulk velocity of the cluster. This is done through using the known redshift of the BCG in the cluster: $0.004283 \pm 1.7 \times 10^{-5}$, and calculating the difference between the observed value. Comparing redshifts in broadbands and narrowbands provides the bulk motion of the entirety of the pointing and specific motions between different metals. This method can be used to observe if the motion of cooler gas is decoupled from the motion of warmer gas in the 4 different pointings.

4.5.1 SPEX or Xspec

Prior to defining final values of the cluster's metallicity and motion a modelling package must be chosen. While both Xspec and SPEX provide individual values for the cluster, and the model types are similar, there are distinct differences in their outputs. Comparing the Fe narrowband values of the central pointings shows this difference best:

M87 Center Pointing (Fe Narrowband)			
Model	Redshift ($\times 10^{-3}$)	Fe Z_{\odot}	σ_{turb} (km/s)
SPEX	4.32 ± 0.04	0.68 ± 0.03	163 ± 15
Xspec	4.32 ± 0.04	1.49 ± 0.04	125 ± 13

Table 4.2: Output parameters for SPEX and Xspec Fe narrowband models. Shown above is the redshift, metallicity and turbulent velocity observed between 6-7 keV in the center pointing. Note the differences in abundance and turbulence.

The two models output values that do not show an overlap within $1-\sigma$ and in many cases $3-\sigma$ as can be seen in Table 4.2 and Fig 4.4. Selecting a model is important as they define the future metallicity and velocity values of the cluster. Modelling the spectrum produced by CHANDRA data of M87 provides an abundance between 1.5-1.7. This is expected as the central 8 kpc of M87 is a metal rich region, thus super solar values from Xspec ($1.49 Z_{\odot}$) should be trusted over the SPEX value ($0.68 Z_{\odot}$). This in conjunction with the M87 team presenting findings that the central pointing has a broadband turbulent velocity of $130 \pm 14 \frac{\text{km}}{\text{s}}$ suggests errors in the SPEX build. This difference is unexpected as a SPEX `hot cie` model should be very similar to an Xspec `TBabs*bvape`c model, especially since they both start with the same initial conditions. SPEX data will not be used due to these differences, all future models will be produced by Xspec until a new SPEX build is released.

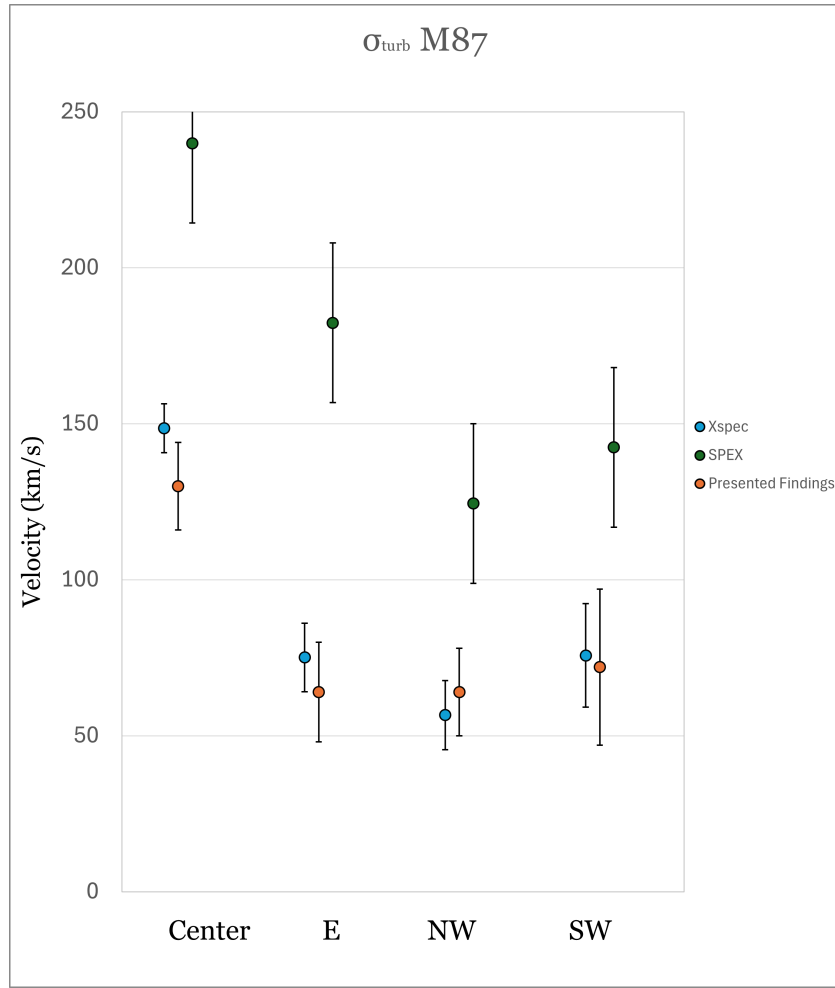


Figure 4.4: Broadband turbulent velocities in each pointing. The orange points are presented findings from other members in the M87 XRISM team. Both SPEX and Xspec models should reproduce these values, but it appears that the SPEX model is not within 1σ of these findings.

4.5.2 Metallicities

Each exposure produces a separate spectrum, with each spectrum containing abundance values for S, Si, Ar, Ca, Fe and Ni. The Xspec model uses the Lodders 2009 abundance table to compare photon counts to solar values. By producing a model for a broadband and a narrowband spectrum the output provides two sets of metallicities for each element.

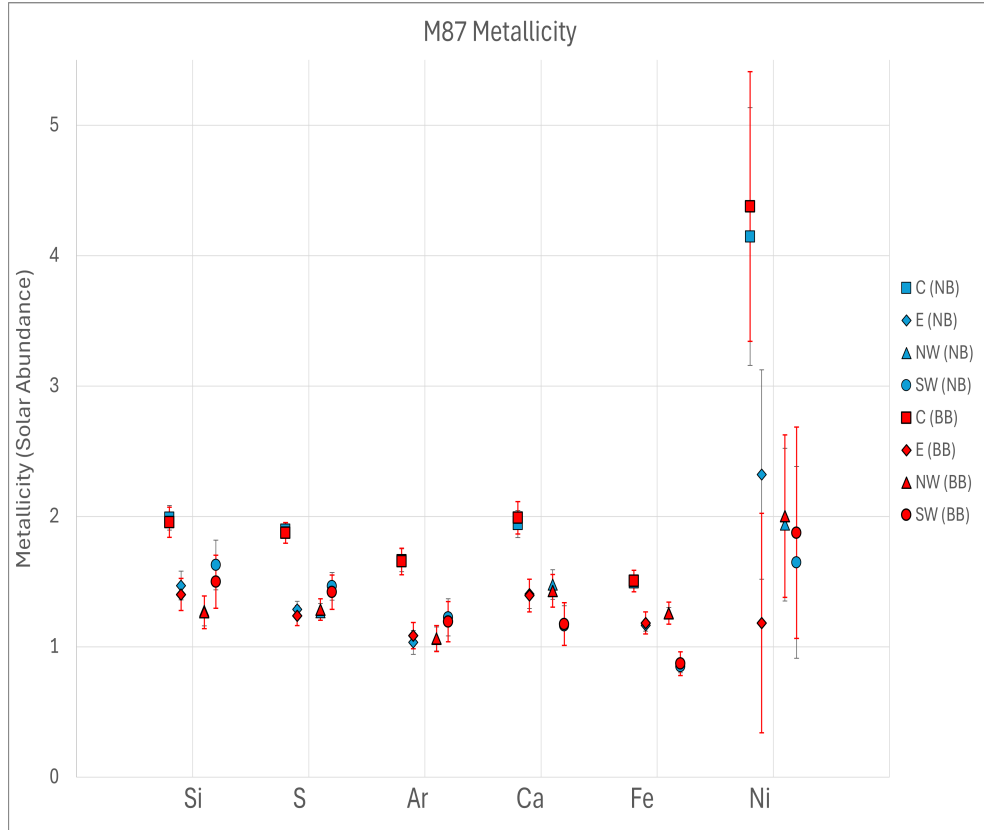


Figure 4.5: The metallicities of the 4 pointings with 6 different abundances. The pointings go in order from left to right: Center (C), East arm (E), North-west (NW) and south-west arm (SW). The blue datapoints represent the narrowband values, while the red represent the broadband values.

The central pointing has a higher metallicity than the other pointings for each metal. This is consistent with clusters that have cooling flows, as the core contains a higher density of cooled gas that feeds into the AGN. This higher density of cooled out gas increases the density of metals in the region, thus increasing the observed abundance. Fig 4.5 shows the effects of using narrowbands for abundances, as most values are found within 1σ of the broadband, but the errors are smaller since it does not observe weak lines beyond the narrowband limits. The only points in which the narrowband and broadband abundances diverge beyond 1σ are regions that have lower total photon counts, such as Ni. This systematic effect on Ni will consistently cause unrealistic values to be produced from models, therefore Ni values such as $4.3 Z_{\odot}$ in the center of the cluster can be ignored. All observed metals have super solar values, this is expected in the center pointing but in the outer pointings there should be a greater decline towards $0.3 Z_{\odot}$. This a steeper decrease towards $0.3 Z_{\odot}$ should be seen if more pointings were proposed further from the center.

Observations of the south-west arm show a trend between the metals. The cooler metals, such as Si, S and Ar appear to be in a higher abundance than the East arm and North-west shock, two features found at the same radial distance as the south-west arm. The hotter metals, such as Ca and Fe appear to be diminished within this region in relation to the other pointings. This implies that the south-west arm is a separate structure that has a higher ratio of cooler metals than the rest of the cluster.

Argon's abundance ratio is used as a probe to test if a dusty core may be the cause of the extinction of metals in the core of a cluster. As Ar cannot create a compound with dust, due to its inert properties, it is expected that Ar would increase in abundance while other metals attenuate. Since the central pointing shows that all of the metals increase towards the core, it defines that a dusty core cannot be seen at this spatial resolution. This is expected as the central pointing observes the inner 8kpc of the cluster, observations of a dusty core would require a spectrum within the inner 3kpc. Future subdivisions in the central pointing may show a dusty core. Decreasing the footprint observed does increase the error on abundances due to spatial spectral mixing between the regions.

4.5.3 Turbulent Broadening

M87 Turbulent Velocity							
Pointing	Broadband (km/s)	Si (km/s)	S (km/s)	Ar (km/s)	Ca (km/s)	Fe (km/s)	Ni (km/s)
Center	149 ± 8	148 ± 29	166 ± 14	166 ± 19	124 ± 21	126 ± 13	149 ± 50
E arm	75 ± 11	149 ± 49	153 ± 25	N/A	68 ± 37	59 ± 14	N/A
NW	57 ± 11	64 ± 100	N/A	N/A	120 ± 30	56 ± 12	N/A
SW arm	76 ± 17	127 ± 85	109 ± 46	41 ± 98	86 ± 53	62 ± 20	N/A

Table 4.3: Turbulent velocity values produced by a TBabs*bvape Xspec model. Each value is a separate model, showing the turbulent velocity broadening on each separate metal. N/A is attributed to unphysical values and can be ignored.

The central pointing has a higher turbulent velocity in both broadband and narrowband values in comparison to the other pointings. This increase correlates to the injection of kinetic energy from the AGN and is consistent with data of clusters from other XRISM teams. The turbulent speeds of the central region is $149 \pm 8 \frac{\text{km}}{\text{s}}$. The outer arms have the atmospheric turbulent motion lower to $\sim 75 \frac{\text{km}}{\text{s}}$, a value expected from a cluster with a jet power of $8 \times 10^{42} \frac{\text{ergs}}{\text{s}}$. The north-west pointing shows the least amount of turbulence, with an average velocity of $57 \pm 11 \frac{\text{km}}{\text{s}}$. This test also shows that Ni is a poor probe for both metallicity and motion, as for the outer pointings there are not enough photons to provide a successful fit. The N/A values define low velocities with unphysical error bars. This can occur either due to low photon counts or very low turbulent velocities, as thermal broadening may fit over the low Doppler broadening component. This implies weak lines or low velocities for S, Ar and Ni in the outer pointings.

There is a contrast between the hot and cold gas metals when observing their turbulent motions. Si and S, the cooler softband metals, both having similar turbulent velocities in all 4 pointings. Ca and Fe, the warmer metals appear to have similar separate turbulent velocities. The broadening value of Fe is consistently within 1σ of Ca for all pointings except the north-west shock. This further implies that the motions of cooler and hotter gas are separate, as the hotter gas is showing a slower turbulent velocity.

4.5.4 Bulk Motions

The bulk velocity defines the flow of the gas in the intracluster medium. To find the bulk velocity of M87's ICM the speed of different regions of gas must be related to the redshift of the center of the cluster's gravitational well. This process is done by fitting a model upon the spectra of different pointings and extracting the model's calculated redshift. XRISM's high spectral resolution is unique to this calculation, as it can also obtain the redshifts of the separate metals in a spectrum. This provides an insight onto the total motion of gas and the motions of specific metals within the cluster. As there may be bulk velocity in the central X-ray gas the baseline of the proper motion of the cluster is at a heliocentric redshift of 0.004283 ± 0.000017 [47], the redshift of the BCG.

M87 Observed Bulk Motion							
Pointing	Broadband (km/s)	Si (km/s)	S (km/s)	Ar (km/s)	Ca (km/s)	Fe (km/s)	Ni (km/s)
Center	-8 ± 7	-20 ± 18	-18 ± 11	-31 ± 14	15 ± 15	10 ± 12	77 ± 39
E arm	4 ± 8	46 ± 28	11 ± 17	11 ± 18	41 ± 18	-15 ± 10	-36 ± 25
NW	-23 ± 8	-55 ± 30	-40 ± 16	7 ± 17	-24 ± 21	-16 ± 9	-76 ± 24
SW arm	-56 ± 11	-141 ± 41	-58 ± 23	-70 ± 24	-18 ± 30	-46 ± 15	-63 ± 39

Table 4.4: Velocity speeds produced by converting the fitted redshifts of the cluster's spectra. This was produced by a `TBabs*bvapecl` model on broadband and narrowband data. The errors are c-stat 1σ model errors convolved with the redshift error found in the NASA Extragalactic Database.

The calculated bulk motions do not take into account the orbital speed of the telescope. A heliocentric correction must be made to offset the effects of the orbit of Earth and the orbit of the telescope. Using the orbital equation: $v = \sqrt{\frac{GM}{r}}$ and XRISM's orbital altitude of 575km [115] the correction range is between $\pm 37.4 \frac{\text{km}}{\text{s}}$. Inputting the observation times tied to the exposures into astropy's velocity correction tool provides a heliocentric correction from -28.4 to $-24.9 \frac{\text{km}}{\text{s}}$. Since a spectrum (the north-west pointing) is made of two combined exposures on different days the correction was averaged between the two dates.

M87 Heliocentric Bulk Motion							
Pointing	Broadband (km/s)	Si (km/s)	S (km/s)	Ar (km/s)	Ca (km/s)	Fe (km/s)	Ni (km/s)
Center	-37 ± 7	-48 ± 18	-46 ± 11	-60 ± 14	-13 ± 15	-18 ± 12	48 ± 39
E arm	-22 ± 8	19 ± 28	-15 ± 17	-15 ± 18	15 ± 18	-41 ± 10	-61 ± 25
NW	-48 ± 10	-80 ± 32	-65 ± 18	-18 ± 19	-49 ± 23	-40 ± 11	-99 ± 26
SW arm	-83 ± 11	-168 ± 41	-85 ± 23	-96 ± 24	-45 ± 30	-72 ± 15	-89 ± 39

Table 4.5: Heliocentric corrected bulk velocities of the ICM in different pointings. The correction was between -28 and -24 depending on the observation time. The north-west pointing is a combination of two exposures, increasing the error in the velocity correction.

$$v_{\text{bulk}} = (z_{\text{obs}} - z)c + v_{\text{corr}} \quad (4.1)$$

Using the heliocentric velocity correction shows that a majority of the gas in all 4 pointings is blueshifted in relation to the known position of the BCG. The arms of the cluster show that they were fired in opposing directions in the plane of the sky. This is shown by the south-west arm being the most blueshifted ($-83 \pm 11 \frac{\text{km}}{\text{s}}$) while the east arm is the least blueshifted ($-22 \pm 8 \frac{\text{km}}{\text{s}}$) with some narrowband values like Si and Ca showing slight redshifts. It appears that the cooler softband metals (Si and S) are moving at a higher bulk velocity than the warmer metals (Fe and Ca). This trend can be seen in the central and north-west pointing, but also appears in the south-west arm at a lesser extent.

Nickel proves to be a poor probe for obtaining bulk velocity information as well. This is expected as the model failed to fit its turbulent velocities in most pointings. The only fit that was successful is in the central pointing, yet the bulk motion of Ni is the only heavily redshifted value ($48 \pm 39 \frac{\text{km}}{\text{s}}$). Being an outlier suggests that the values found for Nickel should be removed.

4.6 Conclusion

Utilizing XRISM's IFU over four major structures in M87 provides higher resolution data to extrapolate the metallicity and motions of the gas within the cluster. The four pointings are aligned to the center of the cluster, the two offset x-ray arms, and a shock front. With XRISM's high spectral resolution of 5 eV, the abundances and motions of separate metals can be observed. The metals above the gate valve filtering limit of 1.7 keV are S, Si, Ar, Ca, Fe and Ni. Each spectrum is modelled with a single temperature TBabs*(bvapc + powerlaw) model to account for both the emissions of the ICM and the photons produced by the AGN. Nickel does not have enough photons to properly fit its characteristic x-ray emission lines and will not be discussed.

All pointings show that the metallicity is above solar values, with the center of the cluster having the highest abundance of metals. This is consistent with previous observations of cool core clusters, wherein the metallicity rises towards the core and may drop within the inner 1-3 kpc of some clusters. The east arm and north-west pointing show similar abundances in every metal. The south-west arm shows a change in the metallicity trend, it has a higher abundance of cooler metals: Si, S and Ar, while the hotter metals have a lower abundance than the other pointings. This shows that south-west arm is comprised of a higher ratio of cooler metals than the rest of the cluster. Observations of Ar do not show the signature of a dusty core, this may be due to the footprint of XRISM's pointings being too large to observe the central drop in the abundances of the other metals.

The broadband turbulent broadening velocity shows higher speeds in the center pointing at $\sim 149 \frac{\text{km}}{\text{s}}$. The outer pointings have a lower turbulent velocity, with the arms of the cluster both being at $\sim 75 \frac{\text{km}}{\text{s}}$ and the outer shock being the most relaxed at $\sim 57 \frac{\text{km}}{\text{s}}$. The extrathermal velocity of the gas in M87 is very low in comparison to other clusters, such as CyngusA with its expected turbulent broadening velocity of $2000 \frac{\text{km}}{\text{s}}$. The narrowband values show that the cooler softband metals are more turbulent than Ca and Fe in the center, north-west and south-west pointings. This difference is consistently between $20-40 \frac{\text{km}}{\text{s}}$, implying a systematic difference between the motions of hotter and cooler gas in the ICM.

The bulk velocity of the ICM is obtained by relating the difference between redshift of the gas and the known redshift of the BCG. The ICM is completely blueshifted as it has a negative bulk velocity in all 4 pointings. The south-west arm is the most blueshifted with a bulk velocity of $-83 \pm 11 \frac{\text{km}}{\text{s}}$ and the east arm is the least blueshifted with a bulk velocity of $-22 \pm 9 \frac{\text{km}}{\text{s}}$. The central and north-west pointing appear to have a similar bulk velocity around $-40 \frac{\text{km}}{\text{s}}$, suggesting that the arms are not fully parallel to the plane of the sky. The small bulk velocities also imply that the BCG might be oscillating around the

center of the gravitational well, causing the atmosphere to be blueshifted in comparison to its position. Again there is a distinction between the cool softband metals and the warmer metals, the softband metals appear to be moving at a higher speed. This can be seen in the center, north-west and south-west pointings, where the softband metals flow 15 - 30 $\frac{km}{s}$ faster than the hotter metals.

The south-west arm is a unique structure with a higher ratio of softband metals flowing at a higher bulk velocity than the rest of the cluster. The data also shows that in most pointings, aside from the east arm, the cooler metals and hotter metals must be grouped separately. This is due to their differences in motion as the cooler softband metals (Si, S and Ar) have higher turbulent speeds and higher bulk velocities than the hotter metals (Fe and Ca). This further suggests a need for two temperature modelling to account for changes in metallicity between the two groups of metals observed. An open gate valve may further highlight this difference as cooler gases with higher emissivity will assist in modelling lower energies, unfortunately they have been attenuated.

Chapter 5

Conclusion

In this thesis I studied the abundances of metals and flows of X-ray photon emitting gas in galaxy clusters. This thesis focuses on the transition from Chandra data to XRISM, allowing for a deeper analysis of X-ray spectra through its high spectral resolution. I show the process of extracting Chandra data, converting to simulated XRISM data and doing a analysis of early XRISM images. In each instance the spectra produced is studied and modelled using different fitting programs (Xspec, SPEX and lm_fit) to obtain metal abundance values and turbulent gas velocities. By understanding the metallicities and flows of the intracluster medium we begin producing data that can glean information on the evolution of clusters.

Using Chandra a subset of 16 clusters were studied using radial spectral extraction. Annular rings were made around clusters, each producing a spectrum that was fitted using Xspec. Each spectrum provides metallicity, temperature and flux, creating radial trends per cluster. The cool core clusters in the dataset have metallicities peaking at a radius between 0.008-0.05 R_{2500} , while the metallicity asymptotes to $0.3 Z_{\odot}$ in the outer regions of all clusters. This result is consistent and independent to the redshift of the clusters (between $z = 0.01 - 0.54$), bolstering early enrichment theories as the metallicity is higher than expected from supernova metal production rates. 6 out of 11 cool core clusters show a significant depletion of metals in their cores. This result suggests that there is dust in the central regions of the cluster that combines with the cooled out gas. These particles would not emit high energy photons, removing the metals from being detected by Chandra. This dataset also showed no clear trends between metallicity and star formation rates of clusters. With this small subset of clusters it was also discovered that A3571 and A2142 show radial metallicity trends that do not align with their core temperature classification. Cluster A3571 shows an increase of metal abundance towards the core with a temperature

profile similar to most non-cool core clusters, while A2142 shows the opposite, a cool core cluster with no increase in metallicity.

Using XRISM's 2.9 x 2.9 arcmin footprint on the 16 clusters I obtained the expected amount of flux and metallicity that would be observed by Resolve. Simulations of HydraA, MS07 and A2199 were produced by upscaling the spectra extracted from this footprint, improving the spectral resolution from 95 eV to 5 eV. The three clusters were selected due to their flux, known jet energies and theoretical turbulent motions. Using a limit of ≥ 150 photons in simulations under 200ks it was found that HydraA outputs enough photons in an additional offset pointing (centered on a large cavity) to propose two pointings. The modelling software was tested by injecting a known turbulent velocity into the simulation, fitting the model on the simulated Fe-K complex and comparing the model's turbulent velocity output. These simulations found that the lm_fit model can extract within 1σ the turbulent velocity at lower speeds ($\sim 100 \frac{km}{s}$) in all 3 clusters, while Xspec is a better tool for simulations at higher speeds ($300+ \frac{km}{s}$). These findings were reformatted into proposals for the A01 cycle of the XRISM mission. Both HydraA pointings were proposed and accepted with a higher priority on the central pointing, A2199 was accepted under a different principle investigator, and MS07 will need to go through the next cycle of proposals.

Finally I provided a deep analysis of early release XRISM data of the Virgo cluster (M87). There are 4 pointings in the cluster, a central pointing, and 3 pointings radially equidistant from the center observing different structures in the cluster. The inner pointing showed an increase of metallicity for all 6 observed metals (Si, S, Ar, Ca, Fe, and Ni), which is consistent with expected results for a cool core cluster. The metallicity in the outer pointings were mostly super solar, with only the south-west arm showing sub-solar values for non-softband metals (Ca and Fe). There were no results showing a depletion of metals in the core of the cluster, this suggests that there is no dust blocking X-ray emissions. The image resolution limits the preliminary results to observing the entirety of the inner 8kpc. The signature depletion of metals in the inner 1-3 kpc for a dusty core may be drowned out by the surrounding metal rich environment.

The turbulent velocity of the center of M87 is $146 \pm 8 \frac{km}{s}$, which is produced by a jet with a power of $8 \times 10^{42} \frac{ergs}{s}$. Beyond the central churned regions the ICM's turbulent motions lower to $\sim 75 \frac{km}{s}$ in the arms and $57 \pm 11 \frac{km}{s}$ in the shock front. These speeds are very low in comparison to the simulated clusters, as is expected due to its weaker jet power. The narrowband broadening values show in the center and the arms that the cooler softband metals (Si, S and Ar) are moving at a higher turbulent velocity than the hotter metals: a 20 - 90 $\frac{km}{s}$ difference.

This separation between hot and cold metals appears in the bulk velocity of the gas, as

the softband metals appear to be more blueshifted (by 15 - 30 $\frac{km}{s}$) than the hotter gasses in the center, southwest arm and northwest shock. The cluster has a small blueshifted bulk flow in comparison to the position of the BCG, implying that the BCG is oscillating around the center of the cluster's gravitational potential well. The south-west arm is the most blueshifted ($\sim -80 \frac{km}{s}$) while the east arm is the least ($\sim -20 \frac{km}{s}$) suggesting they were fired in opposing directions into the plane of the sky.

These observations of the Virgo cluster show that it is necessary to separate the motions of hot and cool gas in the cluster. The observations of M87's turbulent speed and many more preliminary clusters will prove to be the first datapoints in observing the relation of jet energy ($8 \times 10^{42} \frac{ergs}{s}$) and kinetic atmospheric motions ($149 \pm 8 \frac{km}{s}$).

References

- [1] Kazunori Akiyama, Antxon Alberdi, Walter Alef, Juan Carlos Algaba, Richard Anantua, Keiichi Asada, Rebecca Azulay, Uwe Bach, Anne-Kathrin Bacsko, David Ball, et al. The persistent shadow of the supermassive black hole of m 87-i. observations, calibration, imaging, and analysis. *Astronomy & Astrophysics*, 681:A79, 2024.
- [2] Edward Anders and Nicolas Grevesse. Abundances of the elements: Meteoritic and solar. *Geochimica et Cosmochimica acta*, 53(1):197–214, 1989.
- [3] Keith Arnaud, Ben Dorman, and Craig Gordon. An x-ray spectral fitting package, 2003.
- [4] M Arnaud, R Rothenflug, O Boulade, L Vigroux, and E Vangioni-Flam. Some constraints on the origin of the iron enriched intracluster medium. *Astronomy and Astrophysics, Vol. 254, NO. FEB (I), P. 49*, 1992, 254:49, 1992.
- [5] Michel Baranger. General impact theory of pressure broadening. *Physical Review*, 112(3):855, 1958.
- [6] Stefano Bianchi, Giorgio Matt, Fabrizio Nicastro, Delphine Porquet, and Jacques Dubau. Fe xxv and fe xxvi lines from low-velocity, photoionized gas in the x-ray spectra of active galactic nuclei. *Monthly Notices of the Royal Astronomical Society*, 357(2):599–607, 2005.
- [7] L Bîrzan, David A Rafferty, BR McNamara, Michael W Wise, and Paul EJ Nulsen. A systematic study of radio-induced x-ray cavities in clusters, groups, and galaxies. *The Astrophysical Journal*, 607(2):800, 2004.
- [8] Roger D Blandford and Roman L Znajek. Electromagnetic extraction of energy from kerr black holes. *Monthly Notices of the Royal Astronomical Society*, 179(3):433–456, 1977.

- [9] Hans Böhringer, Gayoung Chon, and Masataka Fukugita. The extended rosat-eso flux-limited x-ray galaxy cluster survey (reflex ii)-vii. the mass function of galaxy clusters. *Astronomy & Astrophysics*, 608:A65, 2017.
- [10] Massimiliano Bonamente, Marshall K Joy, Samuel J LaRoque, John E Carlstrom, Erik D Reese, and Kyle S Dawson. Determination of the cosmic distance scale from sunyaev-zel'dovich effect and chandra x-ray measurements of high-redshift galaxy clusters. *The Astrophysical Journal*, 647(1):25, 2006.
- [11] Marcus Brüggen, Evan Scannapieco, and Sebastian Heinz. Evolution of x-ray cavities. *Monthly Notices of the Royal Astronomical Society*, 395(4):2210–2220, 2009.
- [12] AG Butkevich, AV Berdyugin, and P Teerikorpi. Statistical biases in stellar astronomy: the malmquist bias revisited. *Monthly Notices of the Royal Astronomical Society*, 362(1):321–330, 2005.
- [13] CL Carilli, DE Harris, L Pentericci, HJA Röttgering, GK Miley, JD Kurk, and Wil van Breugel. The x-ray-radio alignment in the $z=2.2$ radio galaxy pks 1138–262. *The Astrophysical Journal*, 567(2):781, 2002.
- [14] Subrahmanyan Chandrasekhar. *Hydrodynamic and hydromagnetic stability*. Courier Corporation, 2013.
- [15] Yi-Hao Chen, Sebastian Heinz, and Torsten A Enßlin. Jets, bubbles, and heat pumps in galaxy clusters. *Monthly Notices of the Royal Astronomical Society*, 489(2):1939–1949, 2019.
- [16] Baolian Cheng, Bowen Jing, Paul Andrew Bradley, Joshua Paul Sauppe, and Rebecca R Roycroft. Evolution of highly multimodal rayleigh–taylor instabilities. *High Energy Density Physics*, 52:101131, 2024.
- [17] J Chluba and RA Sunyaev. Two-photon transitions in hydrogen and cosmological recombination. *Astronomy & Astrophysics*, 480(3):629–645, 2008.
- [18] Aline Chu, Florence Durret, and Isabel Márquez. Physical properties of brightest cluster galaxies up to redshift 1.80 based on hst data. *Astronomy & Astrophysics*, 649:A42, 2021.
- [19] Renato Colle, S Simonucci, et al. Deep level spectroscopy and auger spectra. In *Encyclopedia of Condensed Matter Physics Volume One*,, pages 369–378. ELSEVIER, Academic Press, 2005.

- [20] Barbara Comis, Marco De Petris, Andrea Conte, Luca Lamagna, and Simone De Gregori. X-ray calibration of sunyaev–zel'dovich scaling relations with the accept catalogue of galaxy clusters observed by chandra. *Monthly Notices of the Royal Astronomical Society*, 418(2):1089–1101, 2011.
- [21] John E Davis. The formal underpinnings of the response functions used in x-ray spectral analysis. *The Astrophysical Journal*, 548(2):1010, 2001.
- [22] Miguel A de Avillez, Gervásio J Anela, and Dieter Breitschwerdt. Variability of the adiabatic parameter in monoatomic thermal and non-thermal plasmas. *Astronomy & Astrophysics*, 616:A58, 2018.
- [23] Sabrina De Grandi, Stefano Ettori, Marcella Longhetti, and Silvano Molendi. On the iron content in rich nearby clusters of galaxies. *Astronomy & Astrophysics*, 419(1):7–18, 2004.
- [24] Sabrina De Grandi and Silvano Molendi. Metallicity gradients in x-ray clusters of galaxies. *The Astrophysical Journal*, 551(1):153, 2001.
- [25] R Di Stefano, Julia Berndtsson, Ryan Urquhart, Roberto Soria, Vinay L Kashyap, Theron W Carmichael, and Nia Imara. M51-uls-1b: The first candidate for a planet in an external galaxy. *arXiv preprint arXiv:2009.08987*, 2020.
- [26] Steven Diehl, Hui Li, Christopher L Fryer, and David Rafferty. Constraining the nature of x-ray cavities in clusters and galaxies. *The Astrophysical Journal*, 687(1):173, 2008.
- [27] VI Dokuchaev. Self-similar spherical shock solution with sustained energy injection. *Astronomy & Astrophysics*, 395(3):1023–1029, 2002.
- [28] Xiaodong Duan and Fulai Guo. Metal-rich trailing outflows uplifted by agn bubbles in galaxy clusters. *The Astrophysical Journal*, 861(2):106, 2018.
- [29] A. C. Fabian. Cooling flows in clusters of galaxies, 1994.
- [30] AC Fabian, Jeremy S Sanders, S Ettori, GB Taylor, SW Allen, CS Crawford, K Iwasawa, RM Johnstone, and PM Ogle. Chandra imaging of the complex x-ray core of the perseus cluster. *Monthly Notices of the Royal Astronomical Society*, 318(4):L65–L68, 2000.

- [31] AC Fabian, JS Sanders, CS Crawford, CJ Conselice, JS Gallagher III, and RFG Wyse. The relationship between the optical $\text{H}\alpha$ filaments and the x-ray emission in the core of the perseus cluster. *Monthly Notices of the Royal Astronomical Society*, 344(3):L48–L52, 2003.
- [32] AC Fabian, JS Sanders, GJ Ferland, BR McNamara, C Pinto, and SA Walker. Hidden cooling flows in clusters of galaxies–iii. accretion on to the central black hole. *Monthly Notices of the Royal Astronomical Society*, 524(1):716–730, 2023.
- [33] Jianchao Feng and Qingwen Wu. Constraint on the black hole spin of m87 from the accretion-jet model. *Monthly Notices of the Royal Astronomical Society*, 470(1):612–616, 2017.
- [34] Adam Foster, Randall Smith, Nancy S Brickhouse, Patrick D Mullen, Renata S Cumbee, Phillip C Stancil, and Xiaohong Cui. Atomdb 3.1-atomic data and new models for x-ray spectroscopy. In *American Astronomical Society Meeting Abstracts #231*, volume 231, pages 253–03, 2018.
- [35] Fabio Gastaldello, Aurora Simionescu, Francois Mernier, Veronica Biffi, Massimo Gaspari, Kosuke Sato, and Kyoko Matsushita. The metal content of the hot atmospheres of galaxy groups. *Universe*, 7(7):208, 2021.
- [36] M Gendron-Marsolais, RP Kraft, A Bogdan, J Hlavacek-Larrondo, WR Forman, C Jones, Y Su, P Nulsen, SW Randall, and E Roediger. Uplift, feedback, and buoyancy: Radio lobe dynamics in ngc 4472. *The Astrophysical Journal*, 848(1):26, 2017.
- [37] Ian M George and Rehana Yusaf. The ogip format for radial point spread function datasets. 1995.
- [38] Marie-Joëlle Gingras, Alison L Coil, BR McNamara, Serena Perrotta, Fabrizio Brighenti, HR Russell, and S Peng Oh. Complex velocity structure of nebular gas in active galaxies centred in cooling x-ray atmospheres. *arXiv preprint arXiv:2404.02212*, 2024.
- [39] Vitaly Lazarevich Ginzburg and SI Syrovatskii. Cosmic magnetobremssstrahlung (synchrotron radiation). *Annual Review of Astronomy and Astrophysics*, vol. 3, p. 297, 3:297, 1965.
- [40] TA Gomez, T Nagayama, PB Cho, David Parker Kilcrease, Christopher John Fontes, and Mark Christian Zammit. Introduction to spectral line shape theory. *Journal of Physics B: Atomic, Molecular and Optical Physics*, 55(3):034002, 2022.

- [41] Luciano Gottardi and Kenichiro Nagayashi. A review of x-ray microcalorimeters based on superconducting transition edge sensors for astrophysics and particle physics. *Applied Sciences*, 11(9):3793, 2021.
- [42] Daniel Greenberger, Klaus Hentschel, and Friedel Weinert, editors. *Compendium of Quantum Physics: Concepts, Experiments, History and Philosophy*. Springer, 2009.
- [43] James E Gunn and J Richard Gott III. On the infall of matter into clusters of galaxies and some effects on their evolution. *Astrophysical Journal*, vol. 176, p. 1, 176:1, 1972.
- [44] Fulai Guo. The shape of x-ray cavities in galaxy clusters: probing jet properties and viscosity. *The Astrophysical Journal*, 803(1):48, 2015.
- [45] Fulai Guo and S Peng Oh. Feedback heating by cosmic rays in clusters of galaxies. *Monthly Notices of the Royal Astronomical Society*, 384(1):251–266, 2008.
- [46] H Hamacher. The effectiveness of gas purging to reduce contamination under thermal vacuum conditions. *Vacuum*, 35(4-5):189–194, 1985.
- [47] George Helou, BF Madore, M Schmitz, MD Bicay, X Wu, and J Bennett. The nasa/ipac extragalactic database. *Databases & On-Line Data in Astronomy*, pages 89–106, 1991.
- [48] Susanne Höfner and Bernd Freytag. Explaining the winds of agb stars: Recent progress. *Proceedings of the International Astronomical Union*, 16(S366):165–172, 2020.
- [49] MT Hogan, BR McNamara, F Pulido, PEJ Nulsen, HR Russell, AN Vantyghem, AC Edge, and RA Main. Mass distribution in galaxy cluster cores. *The Astrophysical Journal*, 837(1):51, 2017.
- [50] MT Hogan, BR McNamara, FA Pulido, PEJ Nulsen, AN Vantyghem, HR Russell, AC Edge, Iu Babyk, RA Main, and M McDonald. The onset of thermally unstable cooling from the hot atmospheres of giant galaxies in clusters: constraints on feedback models. *The Astrophysical Journal*, 851(1):66, 2017.
- [51] Philip F Hopkins, Paul Torrey, Claude-André Faucher-Giguère, Eliot Quataert, and Norman Murray. Stellar and quasar feedback in concert: effects on agn accretion, obscuration, and outflows. *Monthly Notices of the Royal Astronomical Society*, 458(1):816–831, 2016.

- [52] Murat Hudaverdi, Kunieda Yamashita, and Akihiro Furuzawa. Study of the structure of abell 3571: An xmm-newton view. *Advances in Space Research*, 36(4):643–649, 2005.
- [53] Daniel S Hudson, Rupal Mittal, Thomas H Reiprich, Paul EJ Nulsen, Heinz Andernach, and Craig L Sarazin. What is a cool-core cluster? a detailed analysis of the cores of the x-ray flux-limited hiflugs cluster sample. *Astronomy & Astrophysics*, 513:A37, 2010.
- [54] H-Th Janka, K Langanke, Andreas Marek, G Martínez-Pinedo, and B Müller. Theory of core-collapse supernovae. *Physics Reports*, 442(1-6):38–74, 2007.
- [55] Thomas W Jones and DS De Young. Magnetohydrodynamic simulations of relic radio bubbles in clusters. *The Astrophysical Journal*, 624(2):586, 2005.
- [56] Christian R Kaiser, Georgi Pavlovski, Edward CD Pope, and Hans Fangohr. The stability of buoyant bubbles in the atmospheres of galaxy clusters. *Monthly Notices of the Royal Astronomical Society*, 359(2):493–503, 2005.
- [57] Roy Kilgard. Acis back-illuminated ccds, Dec 1997.
- [58] Chiaki Kobayashi, Amanda I Karakas, and Maria Lugaro. The origin of elements from carbon to uranium. *The Astrophysical Journal*, 900(2):179, 2020.
- [59] Anuradha Koratkar and Omer Blaes. The ultraviolet and optical continuum emission in active galactic nuclei: the status of accretion disks. *Publications of the Astronomical Society of the Pacific*, 111(755):1, 1999.
- [60] Daniel Lecoanet, Ian J Parrish, and Eliot Quataert. The dynamics of rayleigh–taylor stable and unstable contact discontinuities with anisotropic thermal conduction. *Monthly Notices of the Royal Astronomical Society*, 423(2):1866–1882, 2012.
- [61] Hui Li, Giovanni Lapenta, John M Finn, Shengtai Li, and Stirling A Colgate. Modeling the large-scale structures of astrophysical jets in the magnetically dominated limit. *The Astrophysical Journal*, 643(1):92, 2006.
- [62] Elliott H Lieb and Horng-Tzer Yau. A rigorous examination of the chandrasekhar theory of stellar collapse. *Astrophysical Journal, Part 1 (ISSN 0004-637X)*, vol. 323, Dec. 1, 1987, p. 140-144., 323:140–144, 1987.
- [63] K Lodders, H Palme, and H-P Gail. 4.4 abundances of the elements in the solar system: 4 the solar system. *Solar system*, pages 712–770, 2009.

- [64] Katharina Lodders. Solar system abundances and condensation temperatures of the elements. *The Astrophysical Journal*, 591(2):1220, 2003.
- [65] Michael Loewenstein. On iron enrichment, star formation, and type ia supernovae in galaxy clusters. *The Astrophysical Journal*, 648(1):230, 2006.
- [66] Maxim Lyutikov. Magnetic draping of merging cores and radio bubbles in clusters of galaxies. *Monthly Notices of the Royal Astronomical Society*, 373(1):73–78, 2006.
- [67] Greg Madejski. Recent and future observations in the x-ray and gamma-ray bands: chandra, suzaku, glast, and nustar. *arXiv preprint astro-ph/0512012*, 2005.
- [68] Adam B Mantz, Steven W Allen, R Glenn Morris, Aurora Simionescu, Ondrej Urban, Norbert Werner, and Irina Zhuravleva. The metallicity of the intracluster medium over cosmic time: further evidence for early enrichment. *Monthly Notices of the Royal Astronomical Society*, 472(3):2877–2888, 2017.
- [69] Michael McDonald, Massimo Gaspari, BR McNamara, and GR Tremblay. Revisiting the cooling flow problem in galaxies, groups, and clusters of galaxies. *The Astrophysical Journal*, 858(1):45, 2018.
- [70] BR McNamara, F Kazemzadeh, DA Rafferty, L Bîrzan, PEJ Nulsen, CC Kirkpatrick, and MW Wise. An energetic agn outburst powered by a rapidly spinning supermassive black hole or an accreting ultramassive black hole. *The Astrophysical Journal*, 698(1):594, 2009.
- [71] BR McNamara and PEJ Nulsen. Heating hot atmospheres with active galactic nuclei. *Annu. Rev. Astron. Astrophys.*, 45(1):117–175, 2007.
- [72] BR McNamara, M Wise, PEJ Nulsen, LP David, CL Sarazin, M Bautz, M Markevitch, A Vikhlinin, WR Forman, C Jones, et al. Chandra x-ray observations of the hydra a cluster: an interaction between the radio source and the x-ray-emitting gas. *The Astrophysical Journal*, 534(2):L135, 2000.
- [73] Riddhi Mehta. *Magnetohydrodynamics of magnetars' high-energy and radio emissions: A simulation study*. PhD thesis, Purdue University, 2021.
- [74] François Mernier, Jelle de Plaa, Jelle S Kaastra, Y-Y Zhang, Hiroki Akamatsu, Liyi Gu, Peter Kosec, Junjie Mao, Ciro Pinto, Thomas H Reiprich, et al. Radial metal abundance profiles in the intra-cluster medium of cool-core galaxy clusters, groups, and ellipticals. *Astronomy & Astrophysics*, 603:A80, 2017.

- [75] François Mernier, Jelle de Plaa, Norbert Werner, Jelle S Kaastra, Anton JJ Raassen, Liyi Gu, Junjie Mao, Igone Urdampilleta, Nhut Truong, and Aurora Simionescu. Mass-invariance of the iron enrichment in the hot haloes of massive ellipticals, groups, and clusters of galaxies. *Monthly Notices of the Royal Astronomical Society: Letters*, 478(1):L116–L121, 2018.
- [76] Koji Mori, Hiroshi Tomida, Hiroshi Nakajima, Takashi Okajima, Hiroyumi Noda, Hiroyuki Uchida, Hiromasa Suzuki, Shogo Benjamin Kobayashi, Tomokage Yoneyama, Kouichi Hagino, et al. Status of xtend telescope onboard x-ray imaging and spectroscopy mission (xrism). In *Space Telescopes and Instrumentation 2024: Ultraviolet to Gamma Ray*, volume 13093, pages 434–443. SPIE, 2024.
- [77] RF Mushotzky and Michael Loewenstein. Lack of evolution in the iron abundance in clusters of galaxies and implications for the global star formation rate at high redshift. *The Astrophysical Journal*, 481(2):L63, 1997.
- [78] J. D. Myers. X-ray imaging and spectroscopy mission (xrism), Jul 2023.
- [79] J. D. Myers. Nicer data analysis threads - nicer responses (arfs and rmfs), Feb 2024.
- [80] Masanori Nakamura, Hui Li, and Shengtai Li. Structure of magnetic tower jets in stratified atmospheres. *The Astrophysical Journal*, 652(2):1059, 2006.
- [81] DC Nicholls, MA Dopita, RS Sutherland, and LJ Kewley. Electron kappa distributions in astrophysical nebulae. In *Kappa Distributions*, pages 633–655. Elsevier, 2017.
- [82] John Nousek. Science instrument (si) operations handbook for the axaf ccd imaging spectrometer (acis), Nov 1997.
- [83] Paul EJ Nulsen, BR McNamara, Michael W Wise, and LP David. The cluster-scale agn outburst in hydra a. *The Astrophysical Journal*, 628(2):629, 2005.
- [84] FN Owen and JA Eilek. The complex core of abell 2199: The x-ray and radio interaction. *The Astrophysical Journal*, 493(1):73, 1998.
- [85] EK Panagoulia, AC Fabian, and JS Sanders. Searching for the missing iron mass in the core of the centaurus cluster. *Monthly Notices of the Royal Astronomical Society*, 433(4):3290–3296, 2013.
- [86] Electra K Panagoulia, Jeremy S Sanders, and Andy C Fabian. A volume-limited sample of x-ray galaxy groups and clusters–iii. central abundance drops. *Monthly Notices of the Royal Astronomical Society*, 447(1):417–436, 2015.

- [87] William Parrish. Escape peaks in x-ray diffractometry. *Advances in X-Ray Analysis*, 8:118–133, 1964.
- [88] G Peach. Theory of the pressure broadening and shift of spectral lines. *Advances in Physics*, 30(3):367–474, 1981.
- [89] Fabio Pizzolato and Noam Soker. On the rayleigh–taylor instability of radio bubbles in galaxy clusters. *Monthly Notices of the Royal Astronomical Society*, 371(4):1835–1848, 2006.
- [90] Deovrat Prasad, Prateek Sharma, and Arif Babul. Cool-core clusters: The role of bcg, star formation, and agn-driven turbulence. *The Astrophysical Journal*, 863(1):62, 2018.
- [91] Faerlin Pulido. On the origin of cold molecular gas in giant elliptical galaxies. Master’s thesis, University of Waterloo, 2017.
- [92] David A Rafferty, BR McNamara, PEJ Nulsen, and MW Wise. The feedback-regulated growth of black holes and bulges through gas accretion and starbursts in cluster central dominant galaxies. *The Astrophysical Journal*, 652(1):216, 2006.
- [93] Christopher S Reynolds, Barry McKernan, Andrew C Fabian, James M Stone, and John C Vernaleo. Buoyant radio lobes in a viscous intracluster medium. *Monthly Notices of the Royal Astronomical Society*, 357(1):242–250, 2005.
- [94] Mariachiara Rossetti and Silvano Molendi. Cool core remnants in galaxy clusters. *Astronomy & Astrophysics*, 510:A83, 2010.
- [95] Ashley J Ruiter. Type ia supernova sub-classes and progenitor origin. *Proceedings of the International Astronomical Union*, 15(S357):1–15, 2019.
- [96] Mateusz Ruszkowski, TA Enßlin, M Brüggen, S Heinz, and C Pfrommer. Impact of tangled magnetic fields on fossil radio bubbles. *Monthly Notices of the Royal Astronomical Society*, 378(2):662–672, 2007.
- [97] George B Rybicki and Alan P Lightman. *Radiative processes in astrophysics*. John Wiley & Sons, 1991.
- [98] Joana S Santos, Paolo Tozzi, Piero Rosati, and Hans Böhringer. The evolution of cool-core clusters. *Astronomy & Astrophysics*, 521:A64, 2010.
- [99] Craig L Sarazin. X-ray emission from clusters of galaxies. 1988.

- [100] Ethan J Schreier, PAUL Gorenstein, and ERIC D Feigelson. High-resolution x-ray observations of m87-nucleus, jet and radio halo. *Astrophysical Journal, Part 1, vol. 261, Oct. 1, 1982, p. 42-50.*, 261:42–50, 1982.
- [101] A Simionescu, N Werner, H Böhringer, JS Kaastra, A Finoguenov, M Brüggen, and PEJ Nulsen. Chemical enrichment in the cluster of galaxies hydra a. *Astronomy & Astrophysics*, 493(2):409–424, 2009.
- [102] Randall K Smith, Nancy S Brickhouse, Duane A Liedahl, and John C Raymond. Collisional plasma models with apec/aped: emission-line diagnostics of hydrogen-like and helium-like ions. *The Astrophysical Journal*, 556(2):L91, 2001.
- [103] Lyman Spitzer Jr and Jesse L Greenstein. Continuous emission from planetary nebulae. *Astrophysical Journal, vol. 114, p. 407*, 114:407, 1951.
- [104] Yuanyuan Su, Francoise Combes, Valeria Olivares, Gianluca Castignani, Pablo Torne, and Reinout van Weeren. The composition and thermal properties of a cool core lacking a brightest cluster galaxy. *Monthly Notices of the Royal Astronomical Society*, 526(4):6052–6058, 2023.
- [105] Rosie Y Talbot, Martin A Bourne, and Debora Sijacki. Blandford–znajek jets in galaxy formation simulations: method and implementation. *Monthly Notices of the Royal Astronomical Society*, 504(3):3619–3650, 2021.
- [106] Roland Timmerman, Reinout J van Weeren, Andrea Botteon, HJA Röttgering, BR McNamara, Frits Sweijen, Laura Birzan, and Leah K Morabito. Measuring cavity powers of active galactic nuclei in clusters using a hybrid x-ray–radio method—a new window on feedback opened by subarcsecond lofar-vlbi observations. *Astronomy & Astrophysics*, 668:A65, 2022.
- [107] Ondrej Urban, Norbert Werner, SW Allen, Aurora Simionescu, and A Mantz. A uniform metallicity in the outskirts of massive, nearby galaxy clusters. *Monthly Notices of the Royal Astronomical Society*, 470(4):4583–4599, 2017.
- [108] Boy van Minderhout, RJE Jaspers, and JW Oosterbeek. Photon radiation produced by the fusor. 2014.
- [109] Sylvain Veilleux, Roberto Maiolino, Alberto D Bolatto, and Susanne Aalto. Cool outflows in galaxies and their implications. *The Astronomy and Astrophysics Review*, 28:1–173, 2020.

- [110] T Venturi, S Bardelli, M Zagaria, I Prandoni, and R Morganti. Radio emission from the a3571 cluster complex: The final stage of a cluster merger? *Astronomy & Astrophysics*, 385(1):39–54, 2002.
- [111] Yanghua Wang. The ricker wavelet and the lambert w function. *Geophysical Journal International*, 200(1):111–115, 2015.
- [112] AS Wilson and Y Yang. Chandra x-ray imaging and spectroscopy of the m87 jet and nucleus. *The Astrophysical Journal*, 568(1):133, 2002.
- [113] Michael W Wise, BR McNamara, PEJ Nulsen, JC Houck, and LP David. X-ray supercavities in the hydra a cluster and the outburst history of the central galaxy’s active nucleus. *The Astrophysical Journal*, 659(2):1153, 2007.
- [114] SE Woosley and Robert D Hoffman. The alpha-process and the r-process. *Astrophysical Journal, Part 1 (ISSN 0004-637X)*, vol. 395, no. 1, p. 202-239., 395:202–239, 1992.
- [115] Team XRISM. The xrism proposers’ observatory guide - heasarc, Feb 2024.
- [116] H Xu, H Li, D Collins, S Li, and ML Norman. Formation of x-ray cavities by the magnetically dominated jet-lobe system in a galaxy cluster. *The Astrophysical Journal*, 681(2):L61, 2008.
- [117] Robert M Yates, Guinevere Kauffmann, and Qi Guo. The relation between metallicity, stellar mass and star formation in galaxies: an analysis of observational and model data. *Monthly Notices of the Royal Astronomical Society*, 422(1):215–231, 2012.
- [118] Feng Yuan, Zhaoming Gan, Ramesh Narayan, Aleksander Sadowski, Defu Bu, and Xue-Ning Bai. Numerical simulation of hot accretion flows. iii. revisiting wind properties using the trajectory approach. *The Astrophysical Journal*, 804(2):101, 2015.
- [119] Feng Yuan and Ramesh Narayan. Hot accretion flows around black holes. *Annual Review of Astronomy and Astrophysics*, 52(1):529–588, 2014.
- [120] Claudio Zanni, Giuseppe Murante, Gianluigi Bodo, Silvano Massaglia, Paola Rossi, and Attilio Ferrari. Heating groups and clusters of galaxies: the role of agn jets. *Astronomy & Astrophysics*, 429(2):399–415, 2005.

- [121] Congyao Zhang, Irina Zhuravleva, Marie-Lou Gendron-Marsolais, Eugene Churazov, Alexander A Schekochihin, and William R Forman. Bubble-driven gas uplift in galaxy clusters and its velocity features. *Monthly Notices of the Royal Astronomical Society*, 517(1):616–631, 2022.

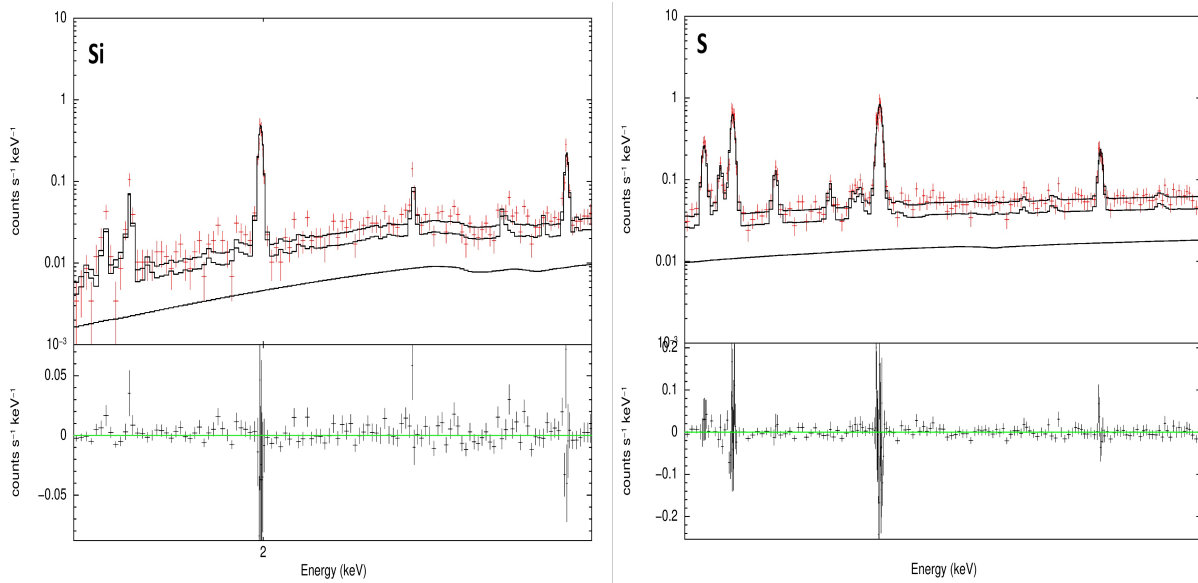
APPENDICES

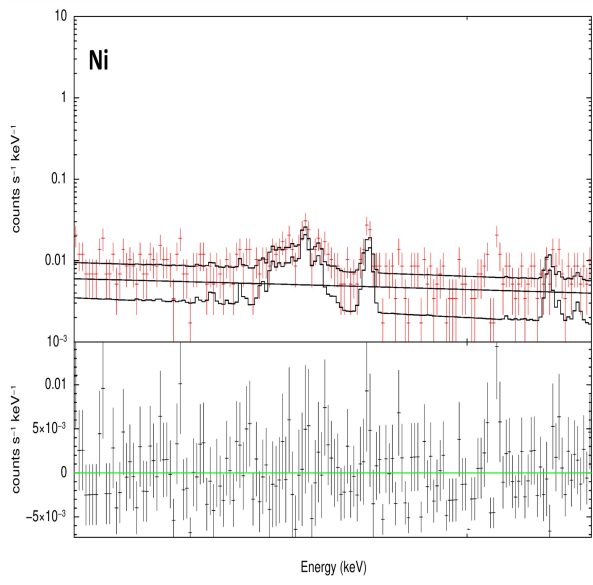
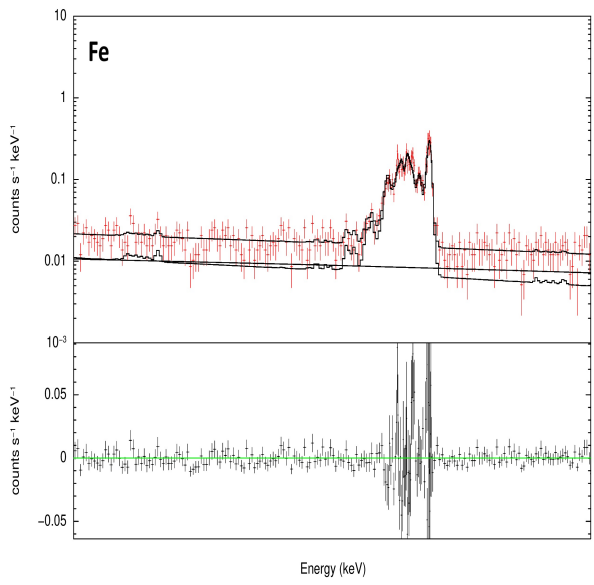
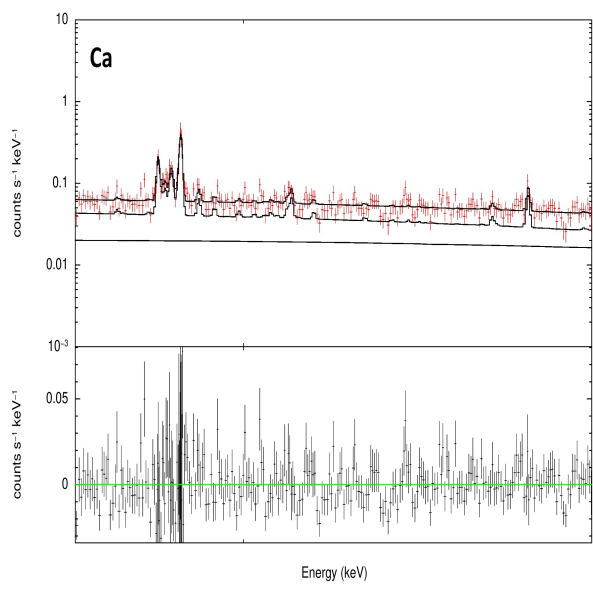
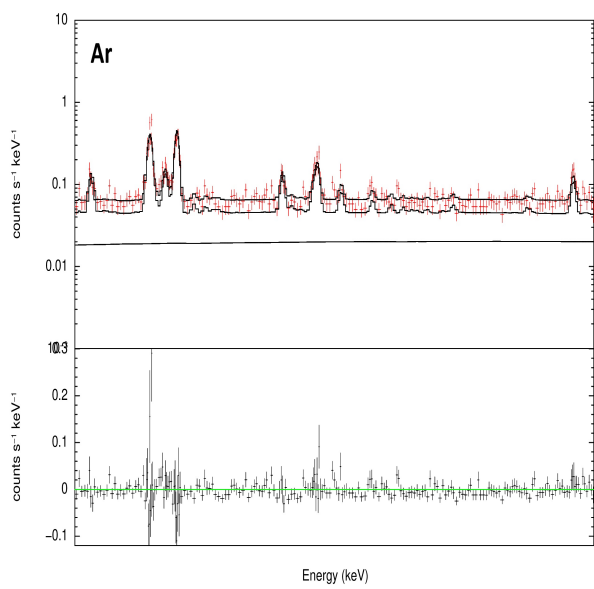
Appendix A

Chandra Cluster Datasheets

A.1 XRISM Narrowbands

Narrowband spectra used in M87 observations. The selected images are from the central pointing, using a TBabs*(bapec+powerlaw) model. The residuals between the model and data are shown in the bottom graph.



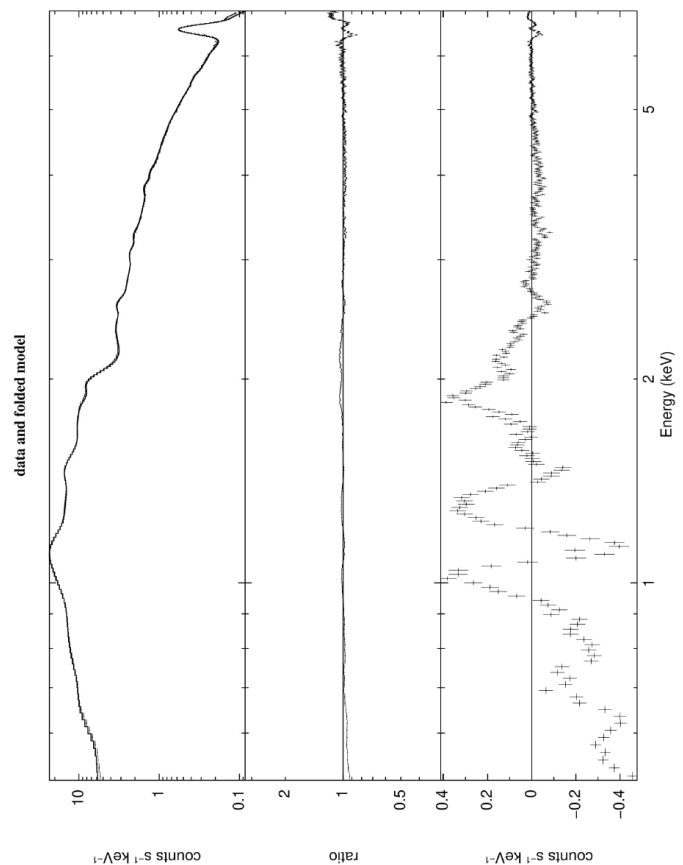
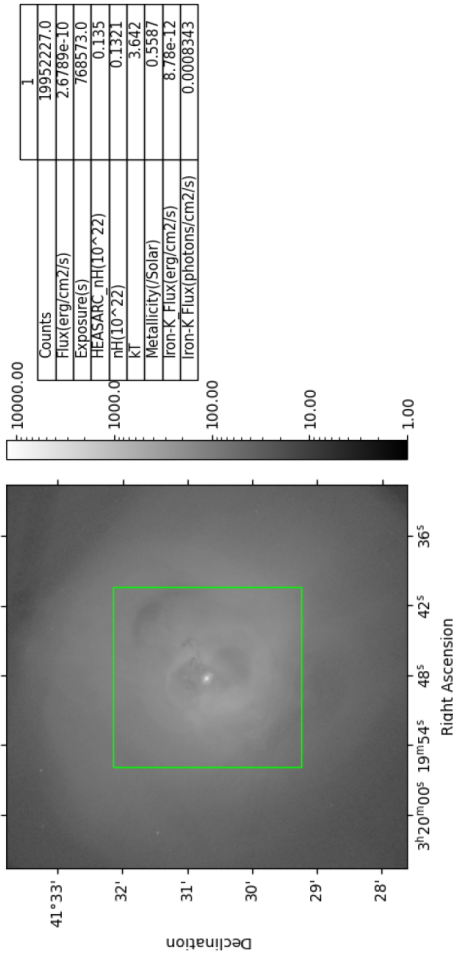
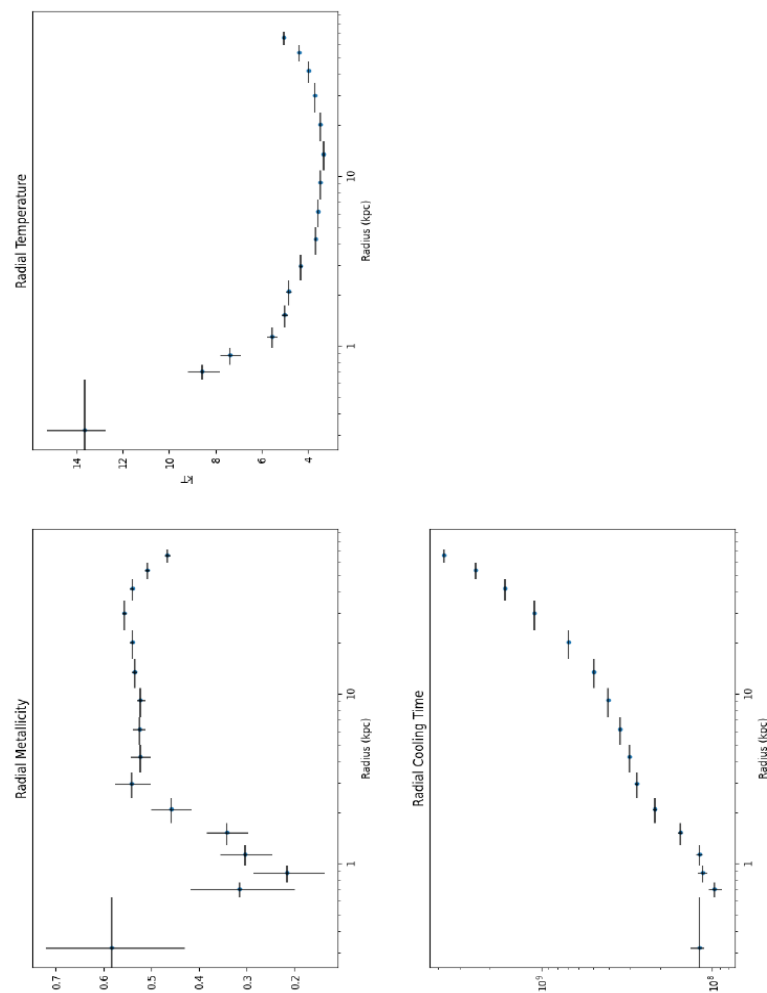
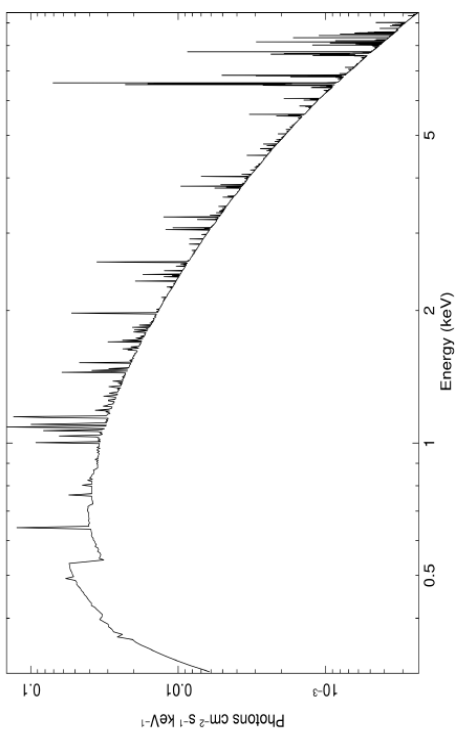


A.2 The Datasheets

The datasheets are produced by extracting a spectrum from a Chandra image. The datasheets consist of an image of the cluster, centered on the core of the cluster, with a green box showing the 2.9 x 2.9 arcmin footprint of XRISM. It contains a table of data extracted from the XRISM sized region, including flux, exposure time, hydrogen column density, temperature, metallicity and the flux produced by the Iron-K complex. Below there is a graph showing the XRISM footprint spectrum with an Xspec model on top of the data, the second and third portions of the graph are the residuals between the model and the data. The second page contains the raw model without data attributed to it and the radial profiles of the cluster. The radial profiles are not produced using the XRISM footprint, rather using concentric annular regions beginning from the center. Each region produces a spectrum and is modelled to obtain metallicity and temperature values. The cooling time graph is produced by using the inner and outer radii of the annulus, the flux and the temperature of the annular region through Eq 2.3 in Chapter 2.

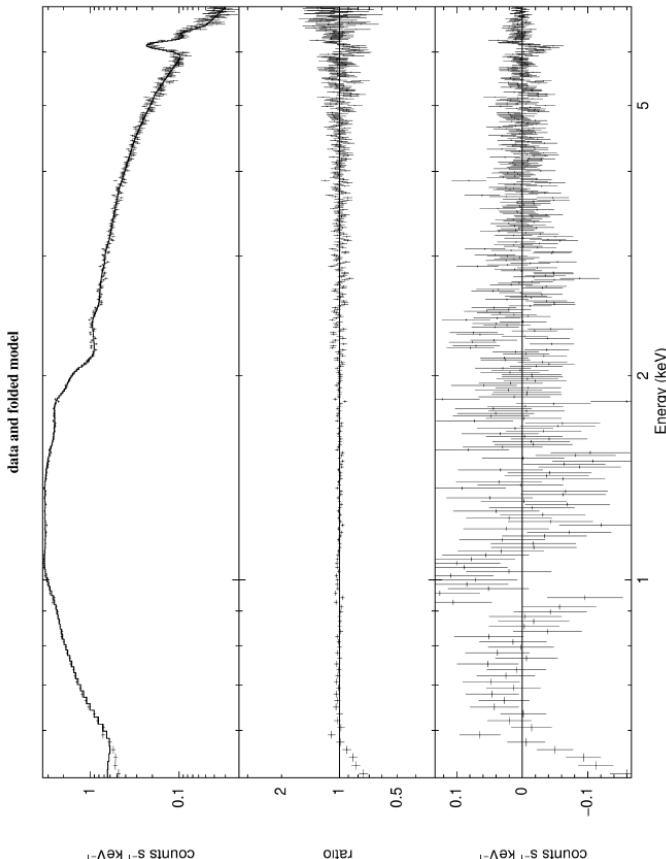
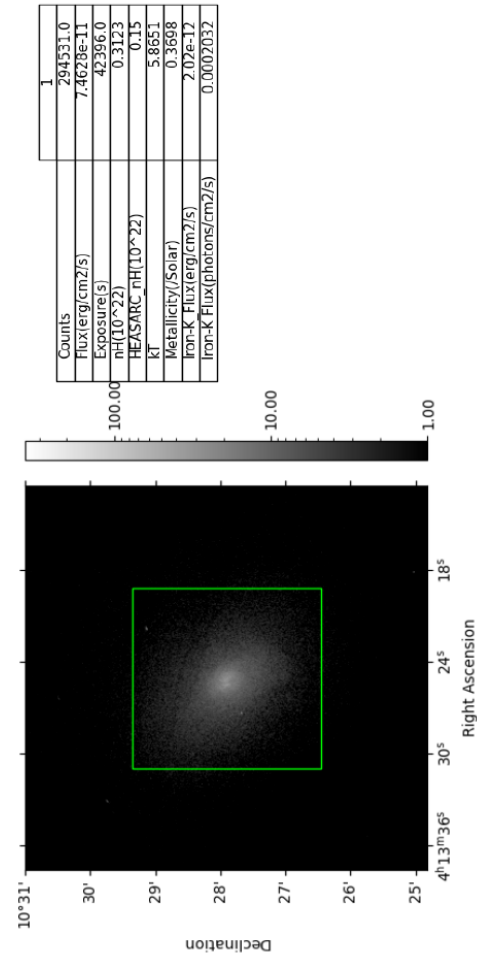
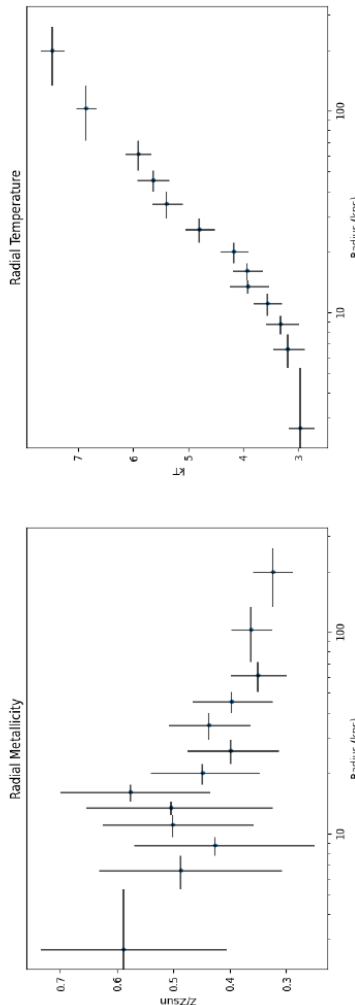
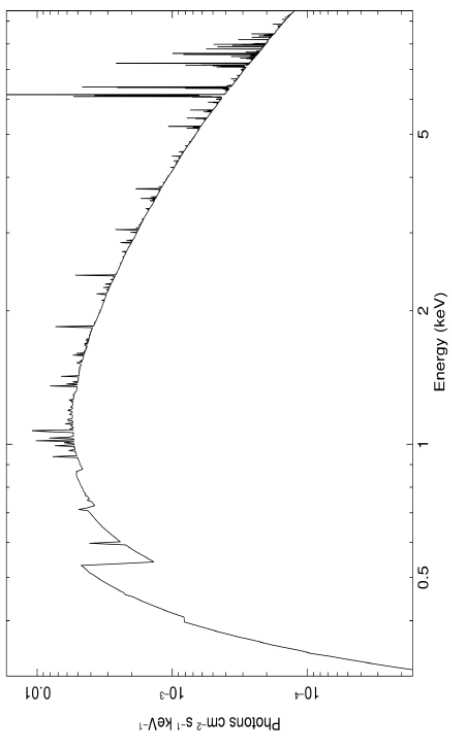
Galaxy Cluster: A426

Current Theoretical Model



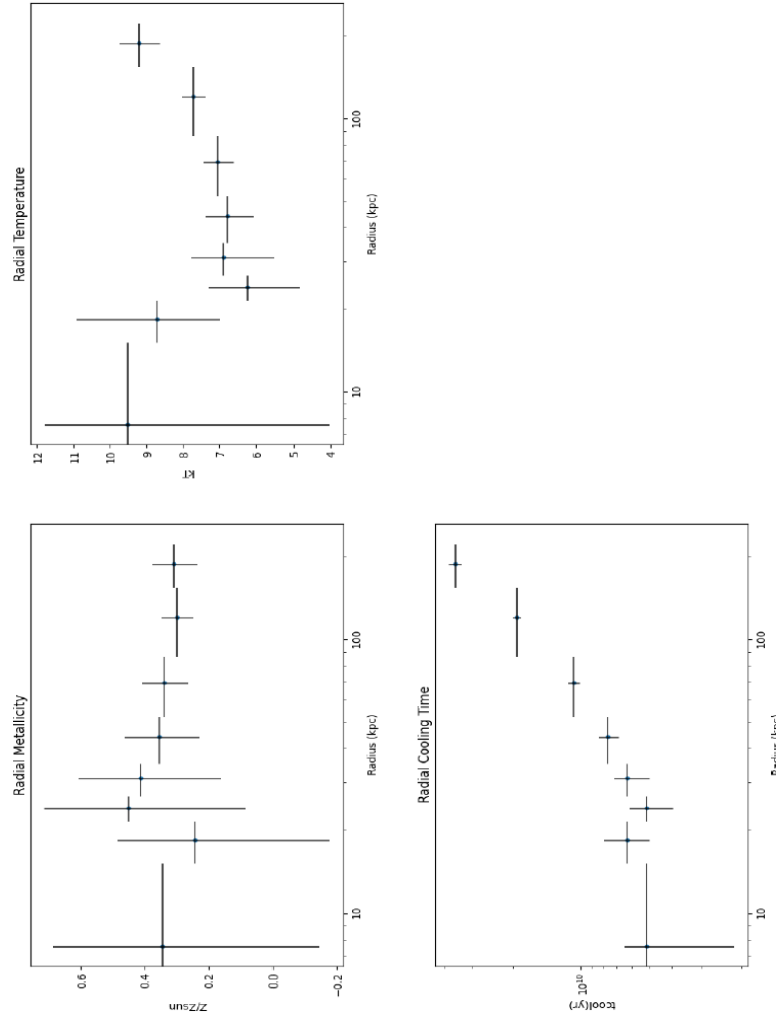
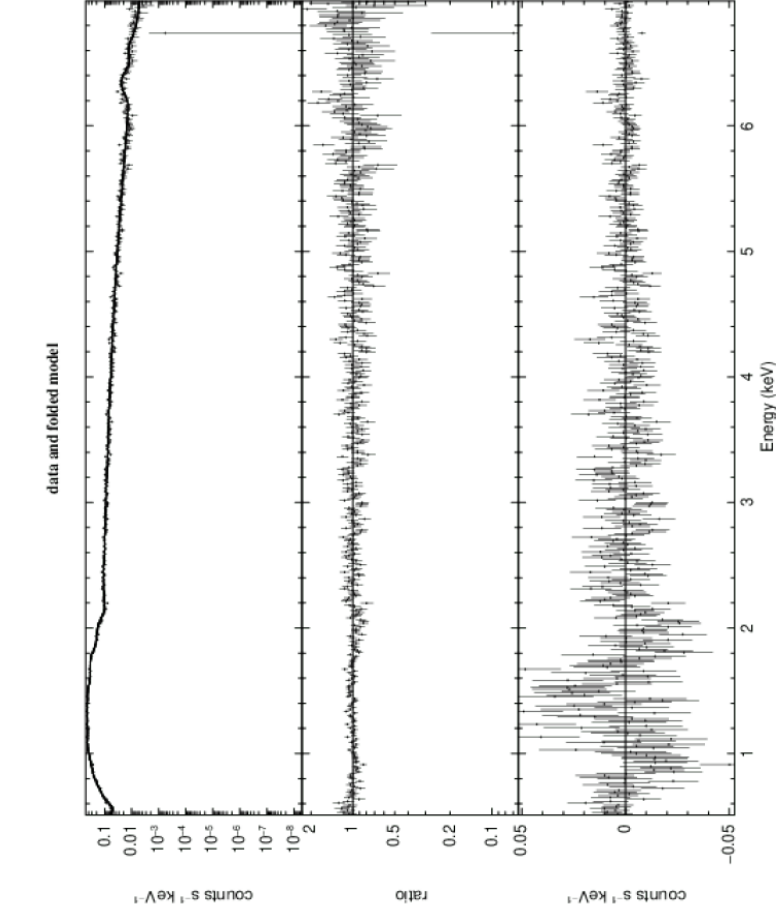
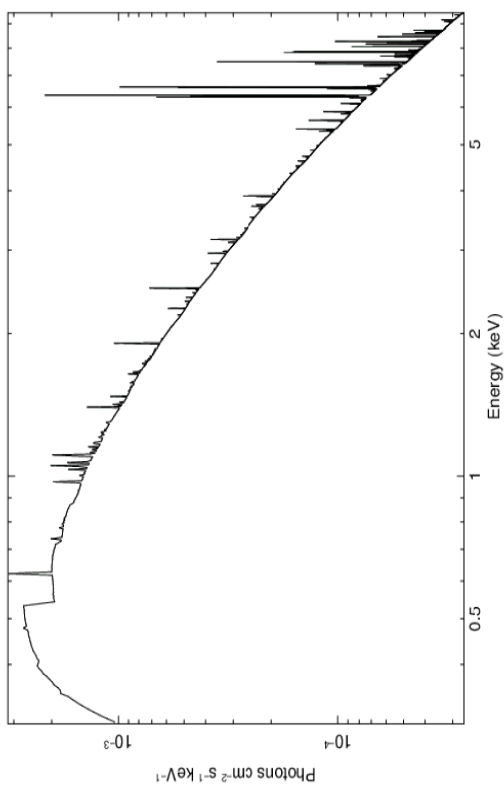
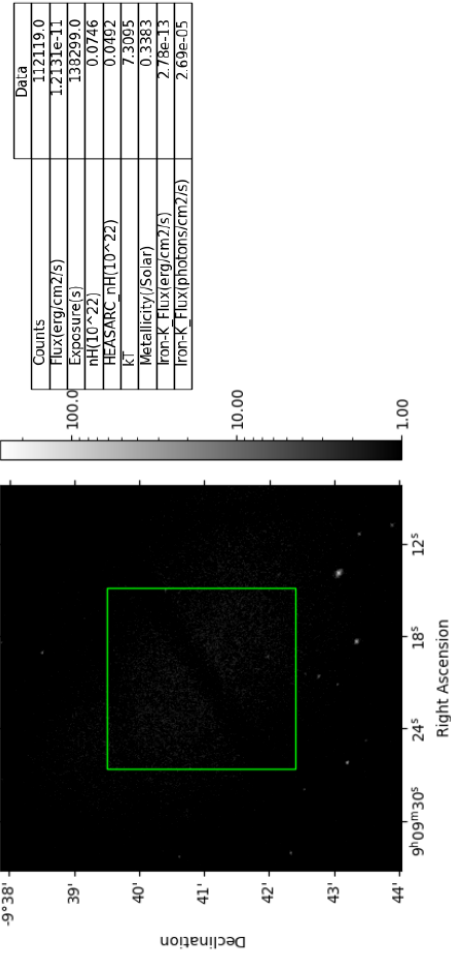
Galaxy Cluster: A478

Current Theoretical Model



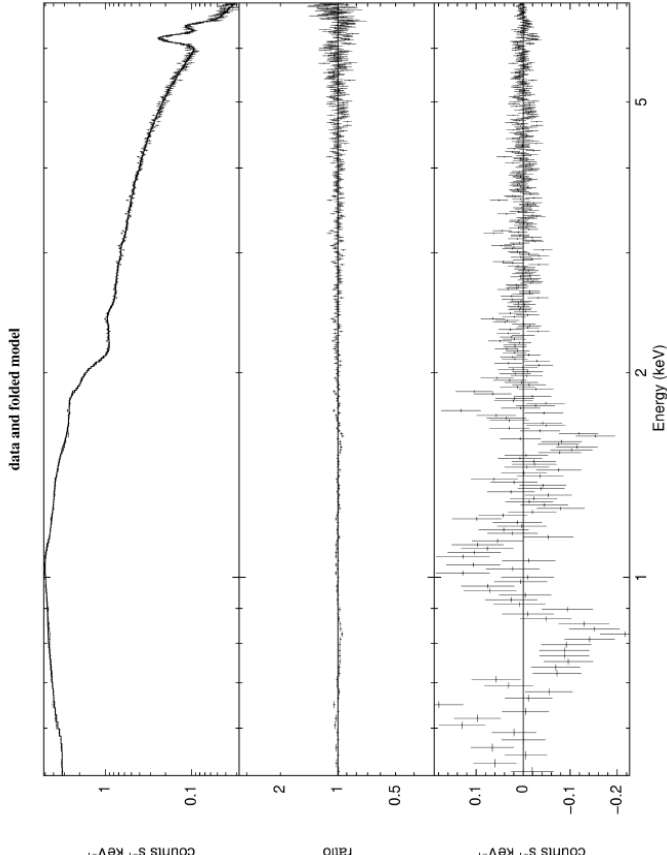
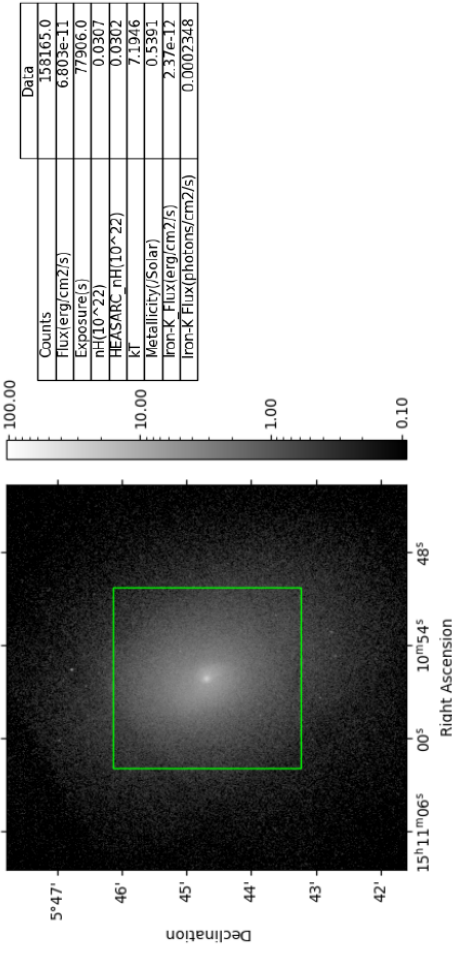
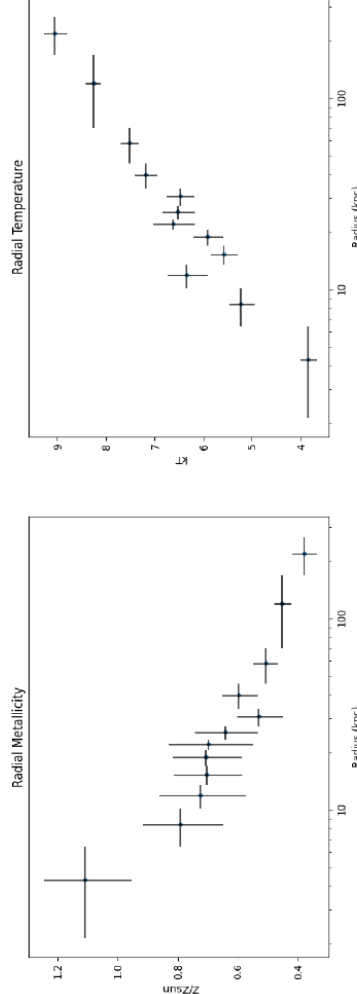
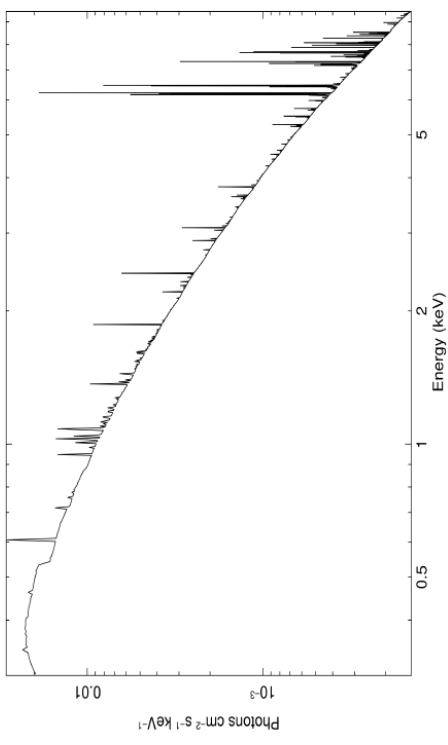
neolinx 15-Jun-2023 13:52

Galaxy Cluster: A754



Galaxy Cluster: A2029

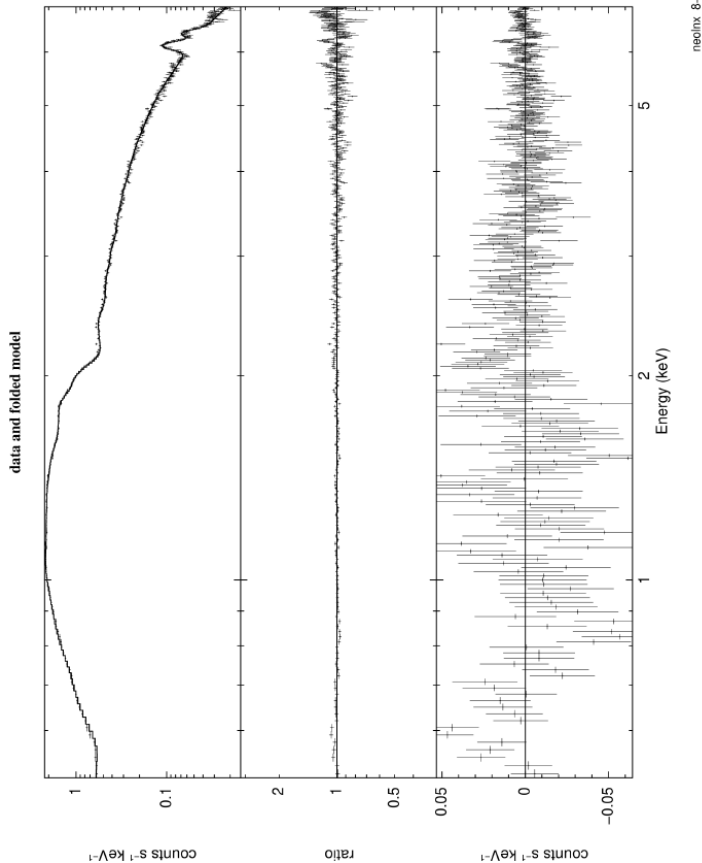
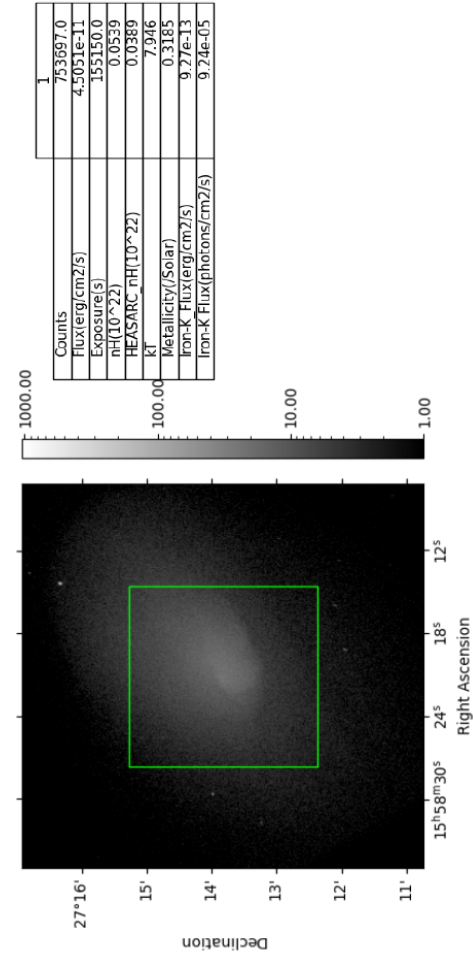
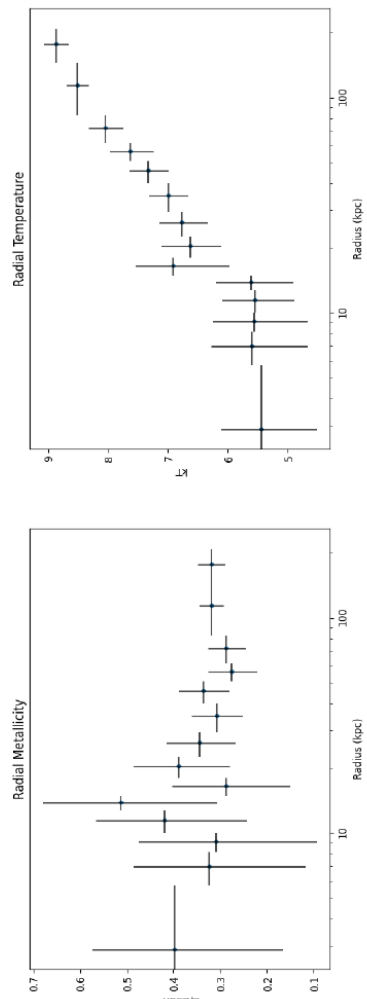
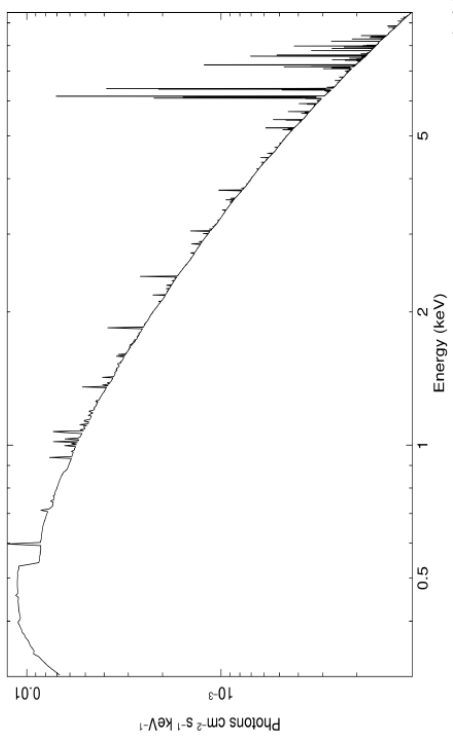
Current Theoretical Model



neulinx 30-May-2023 10:47

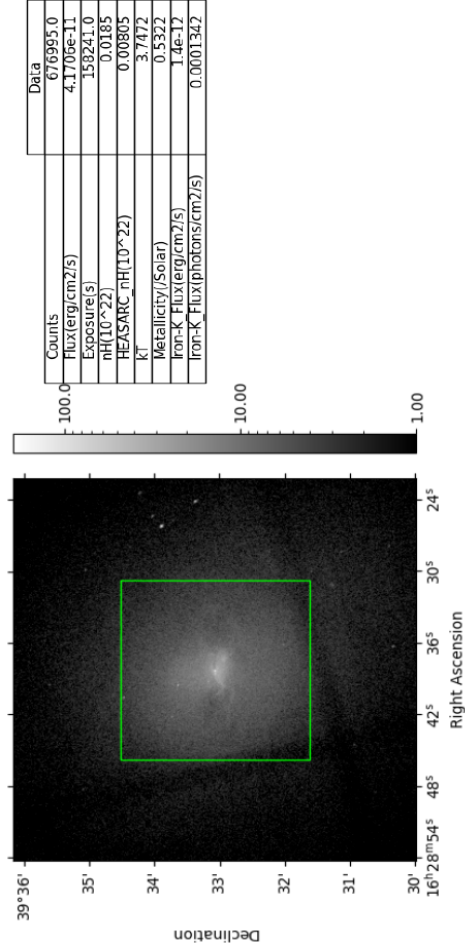
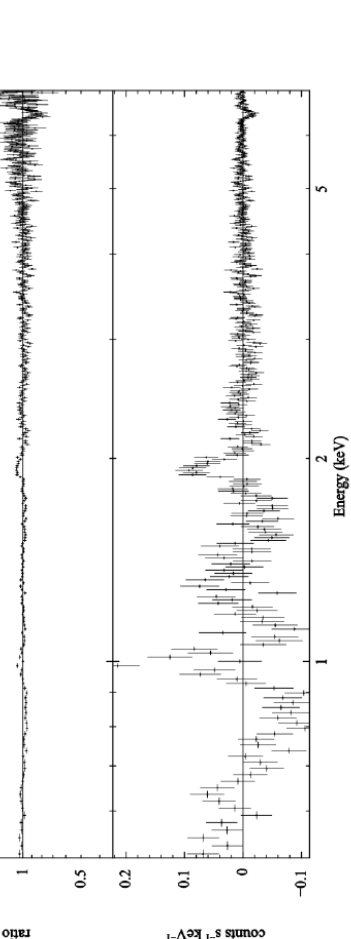
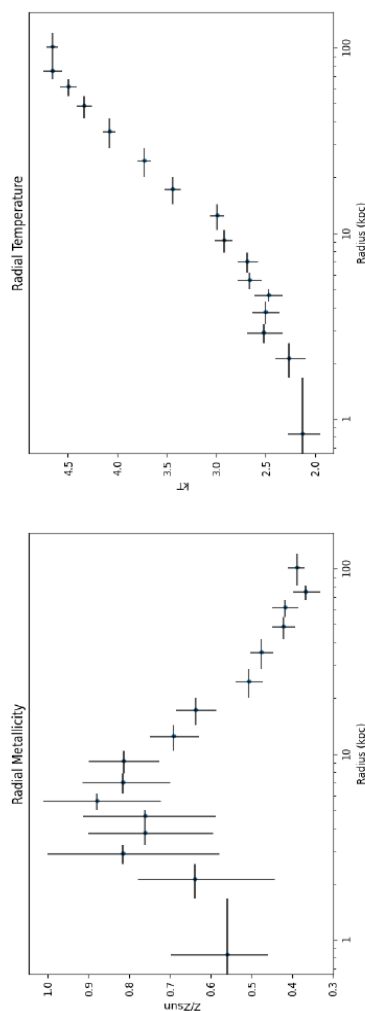
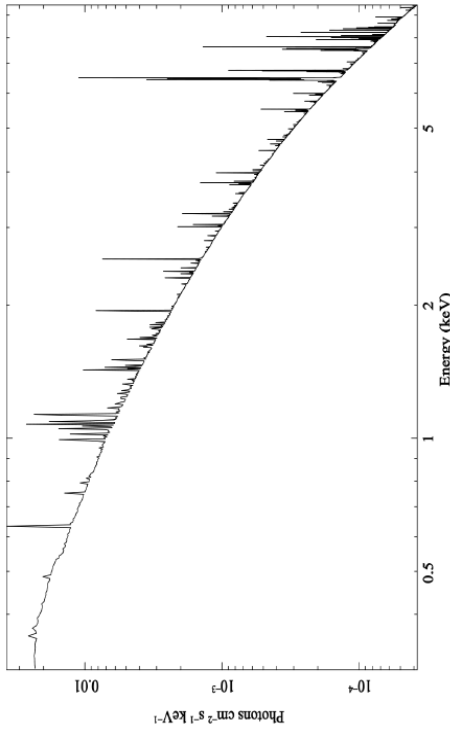
Galaxy Cluster: A2142

Current Theoretical Model



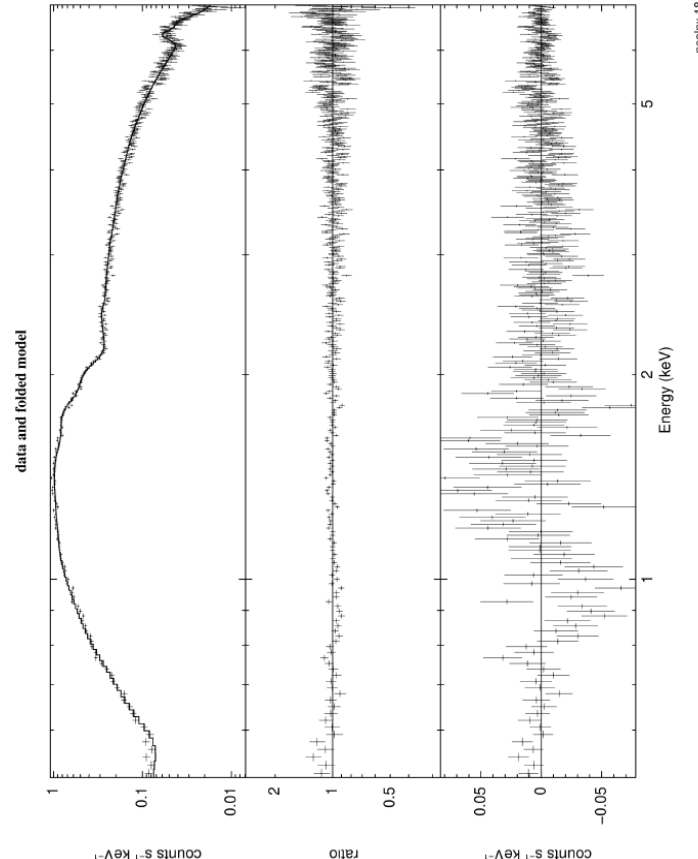
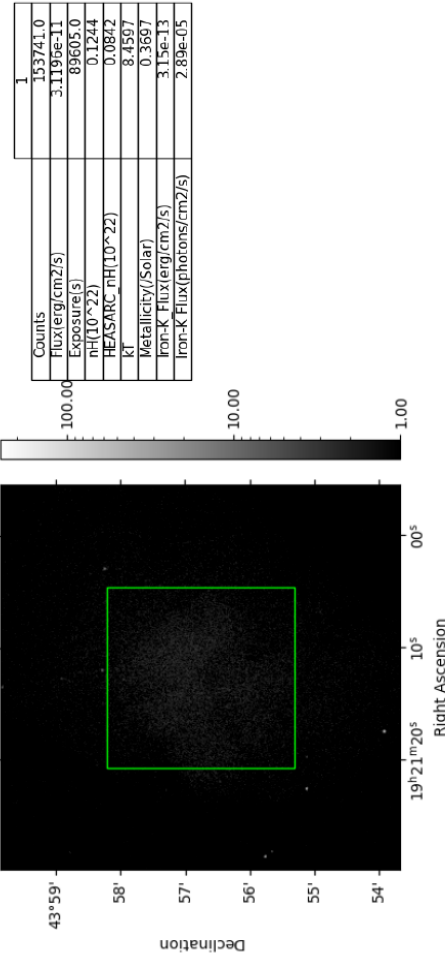
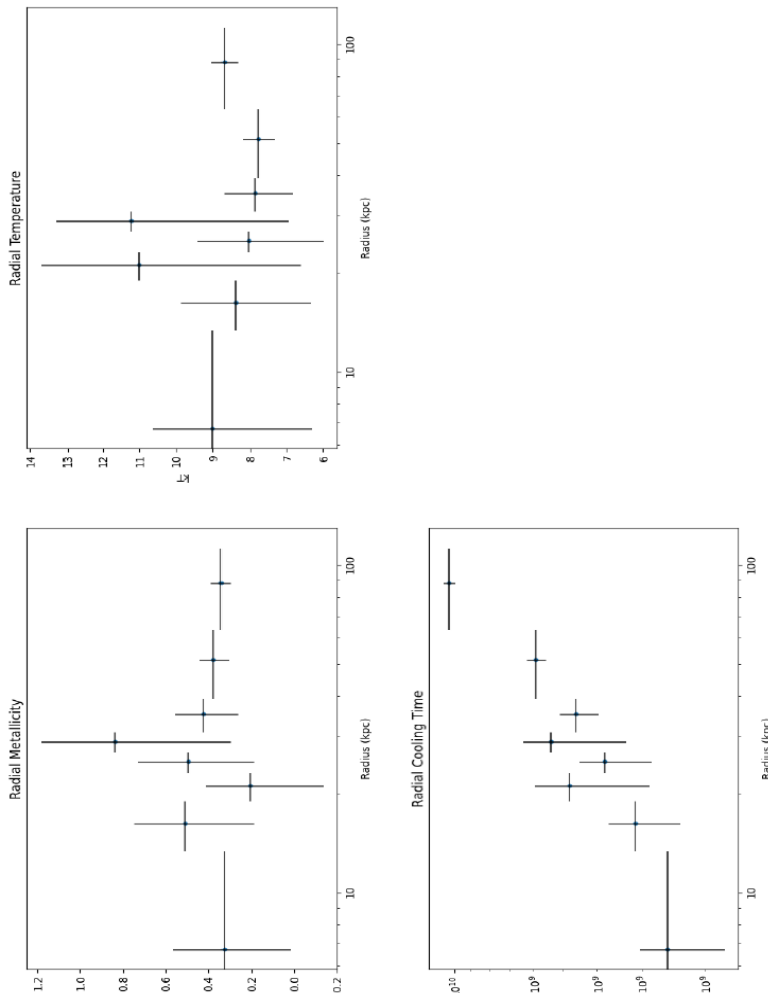
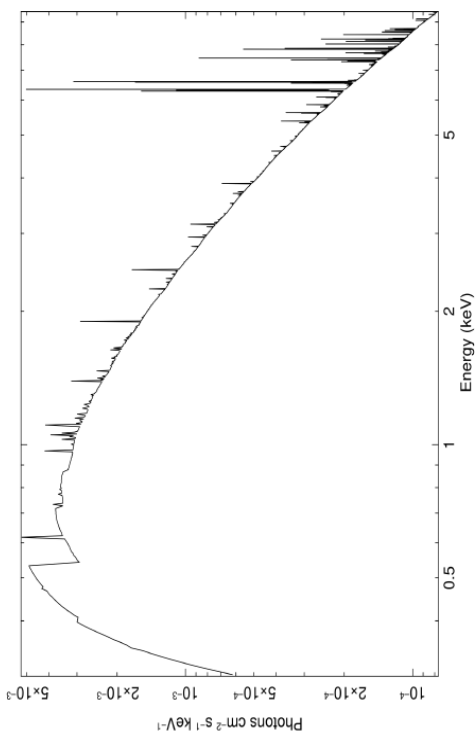
Galaxy Cluster: A2199

Current Theoretical Model

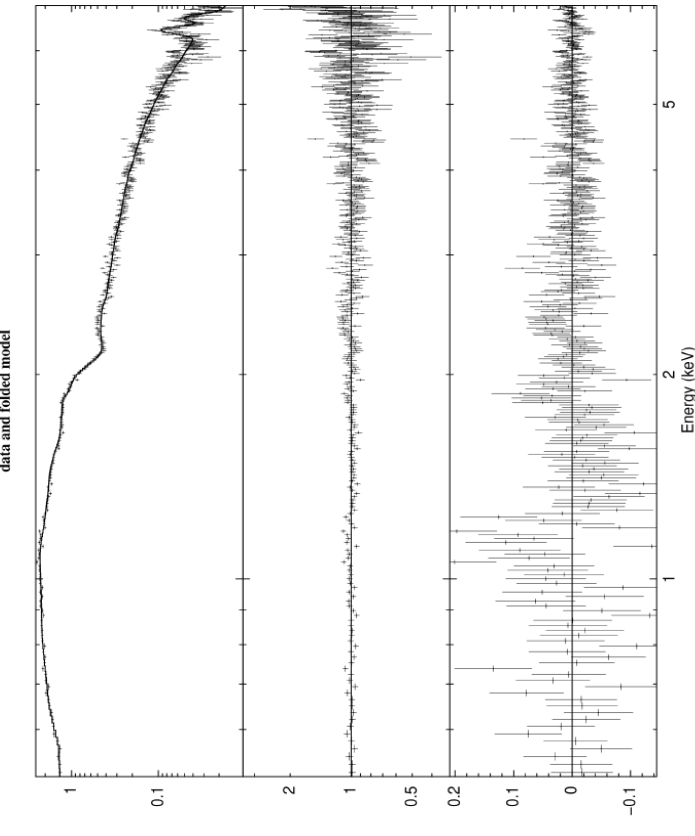
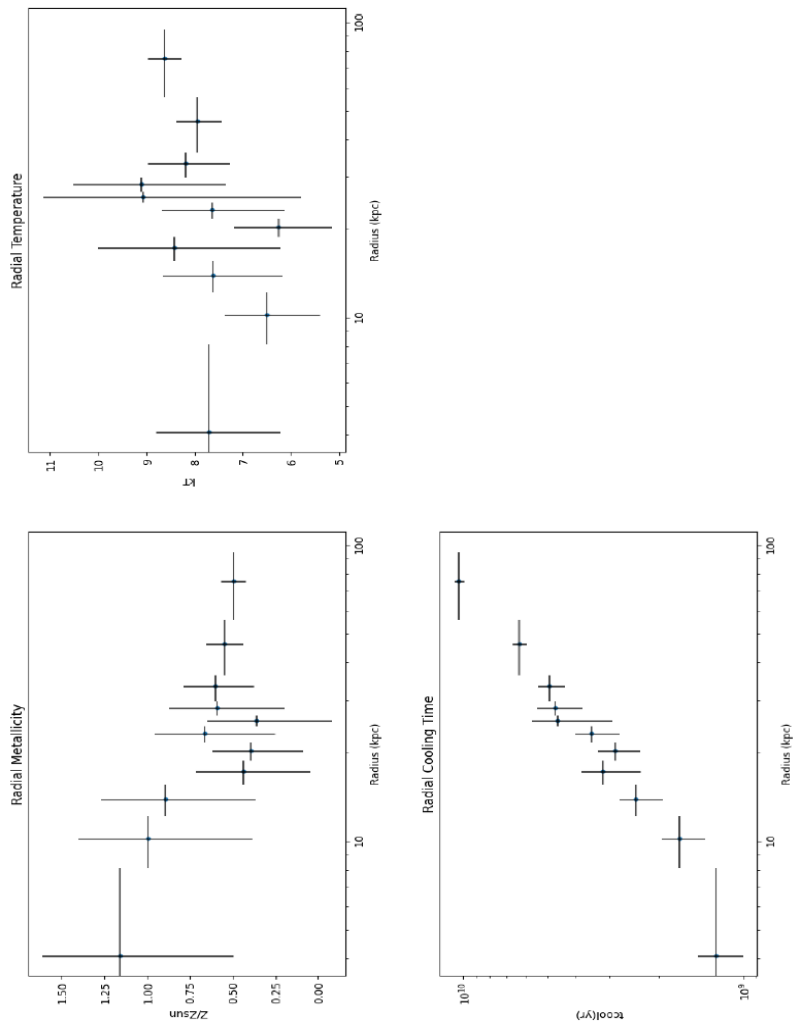
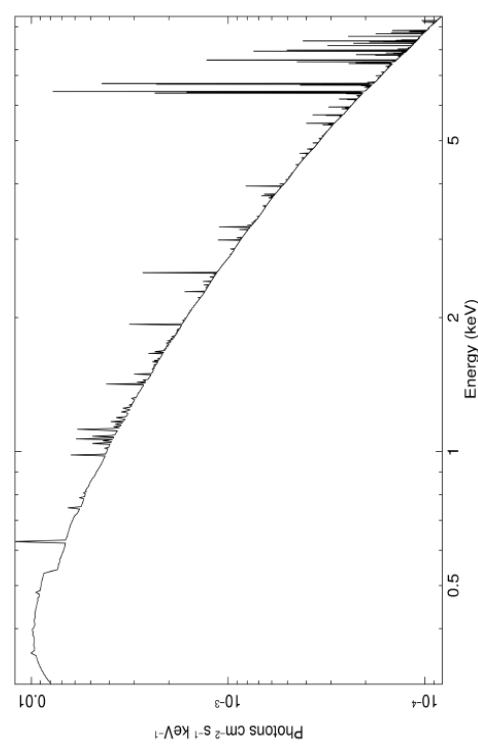
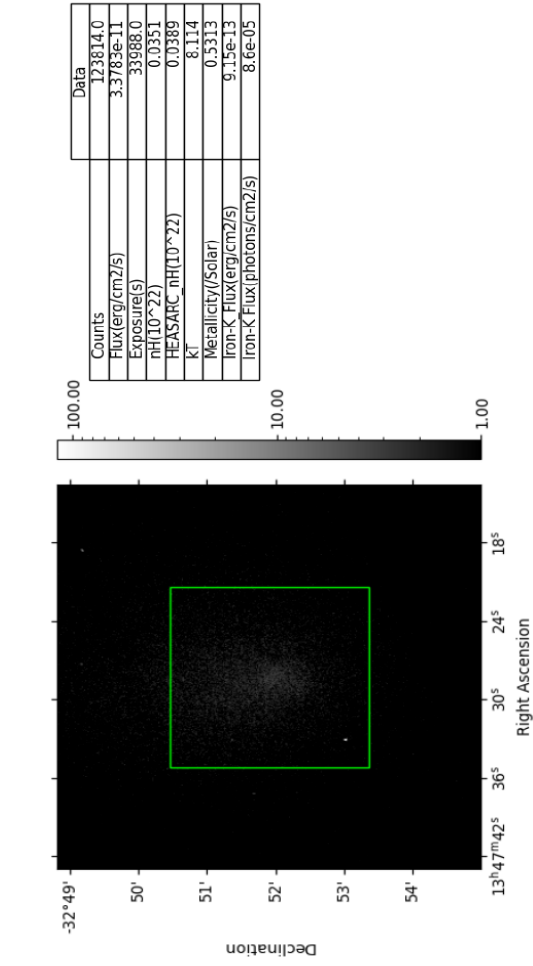


Galaxy Cluster: A2319

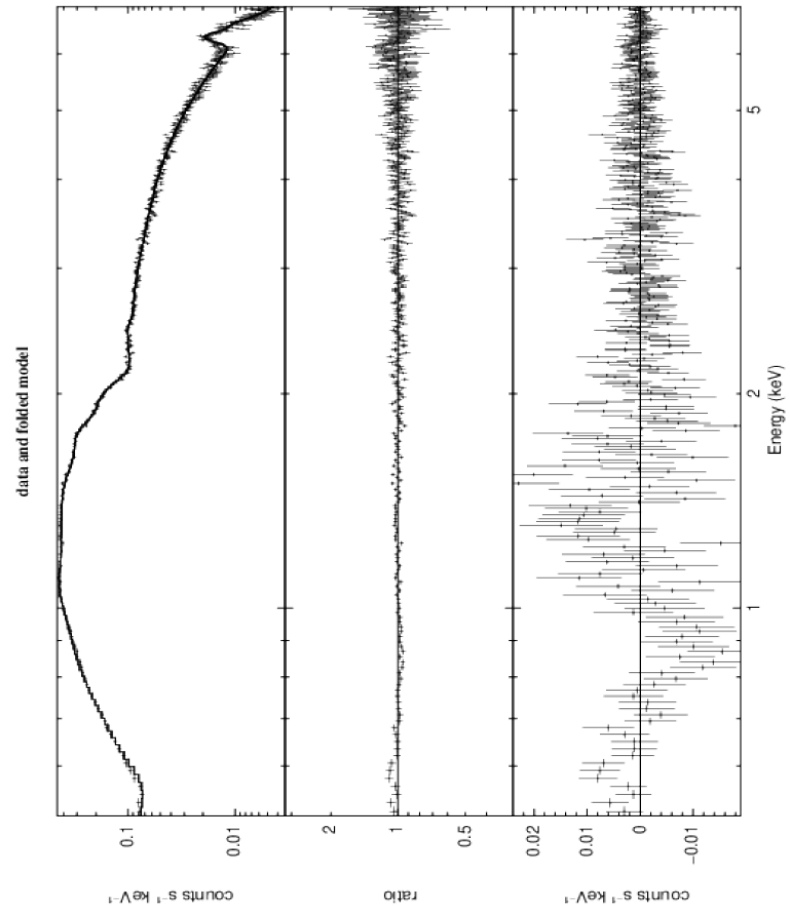
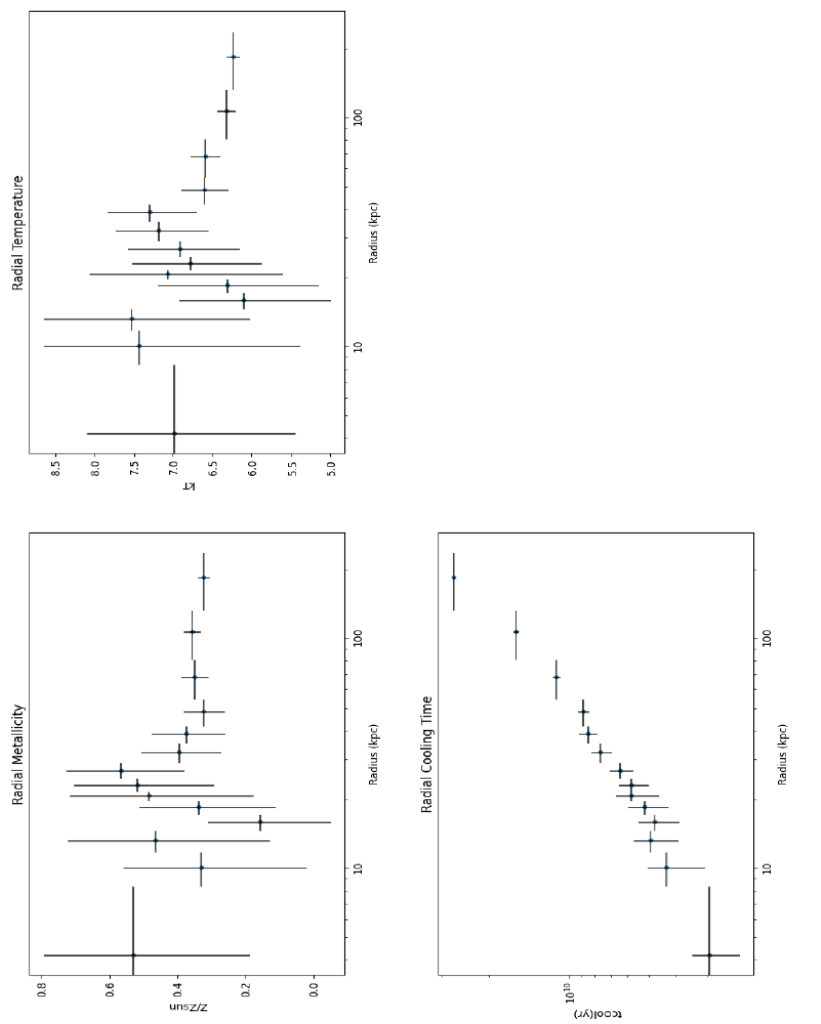
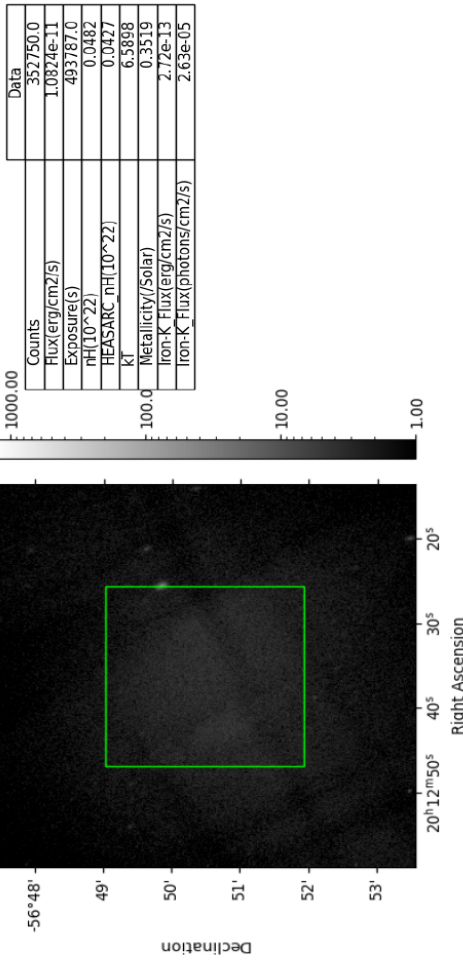
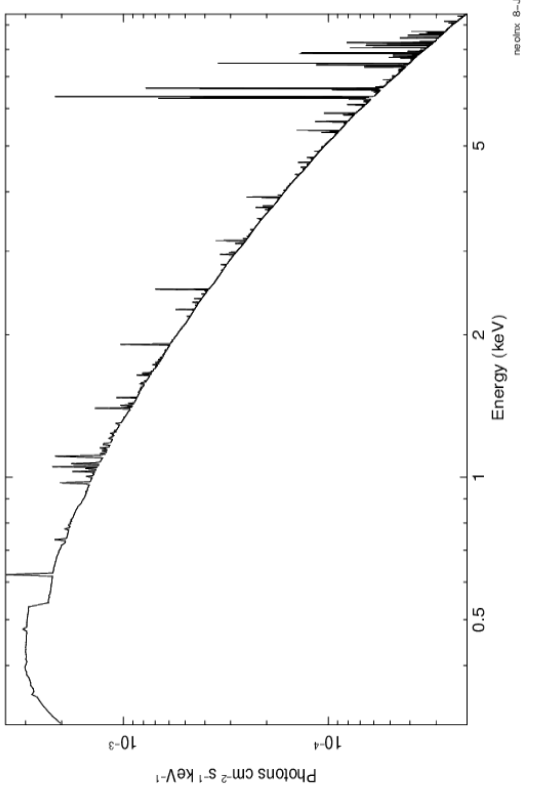
Current Theoretical Model



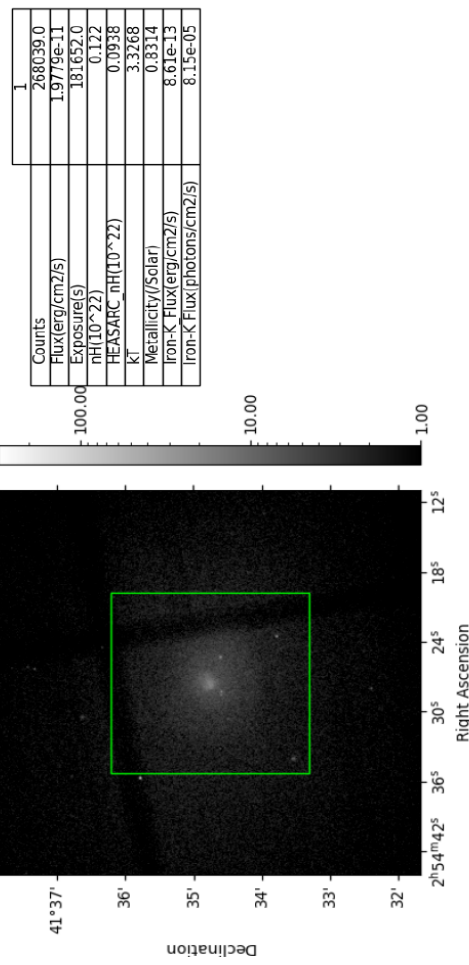
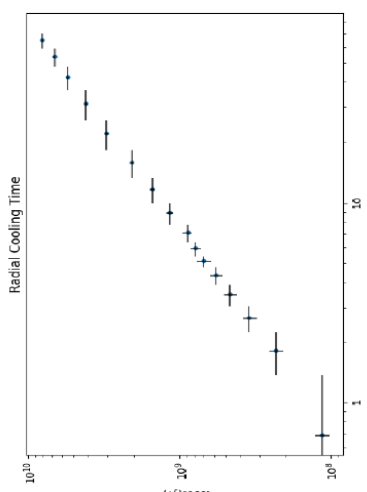
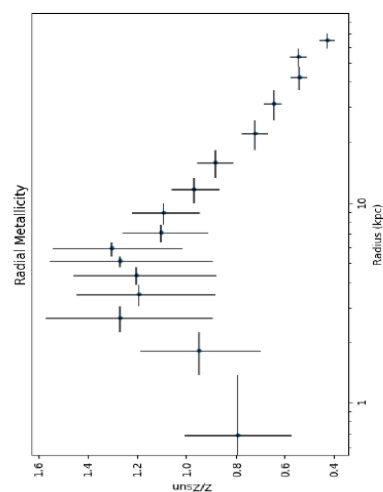
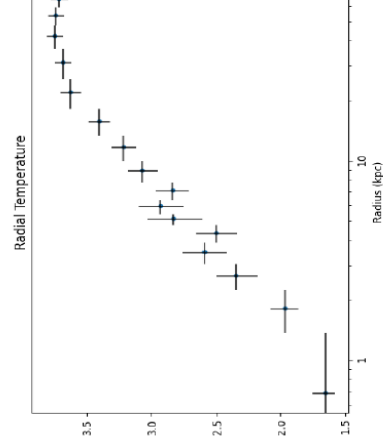
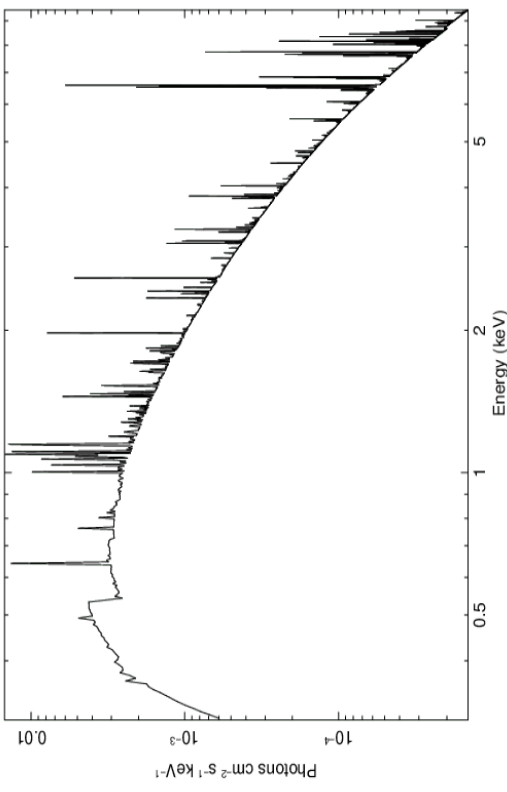
Galaxy Cluster: A353



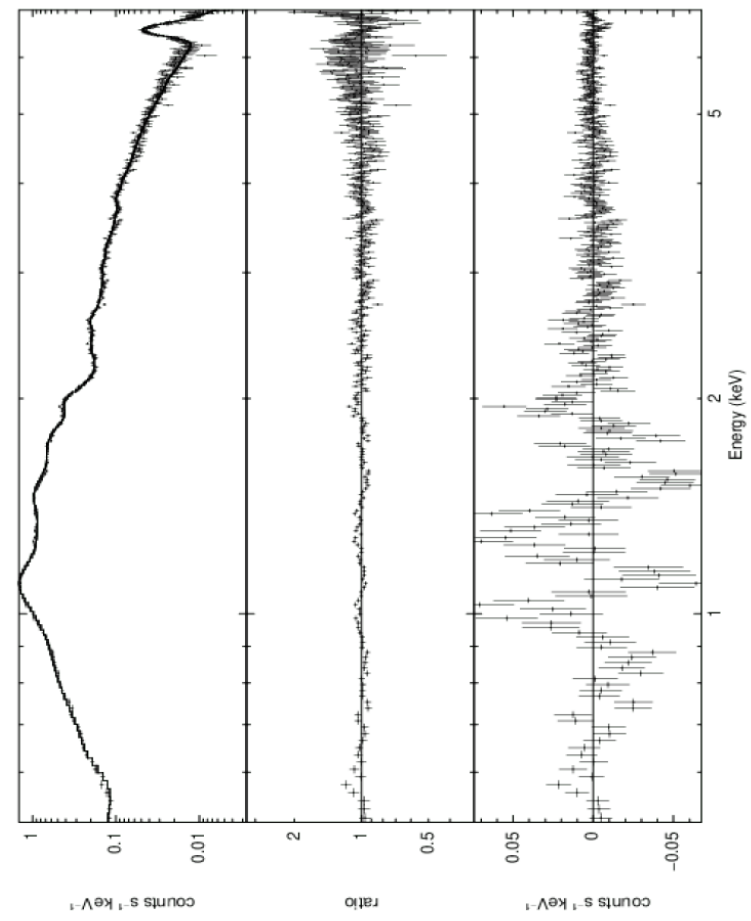
Galaxy Cluster A300



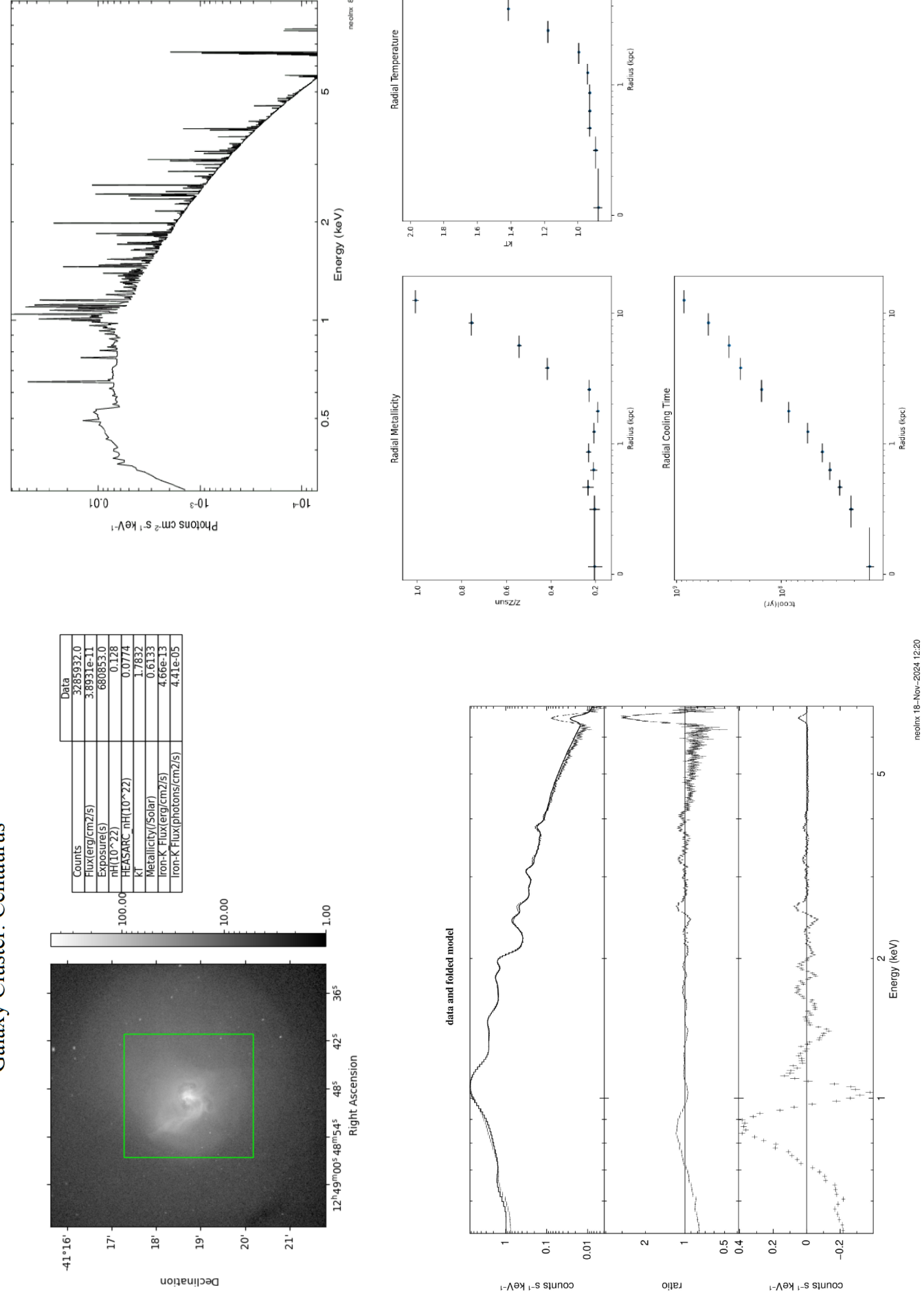
Current Theoretical Model



data and folded model

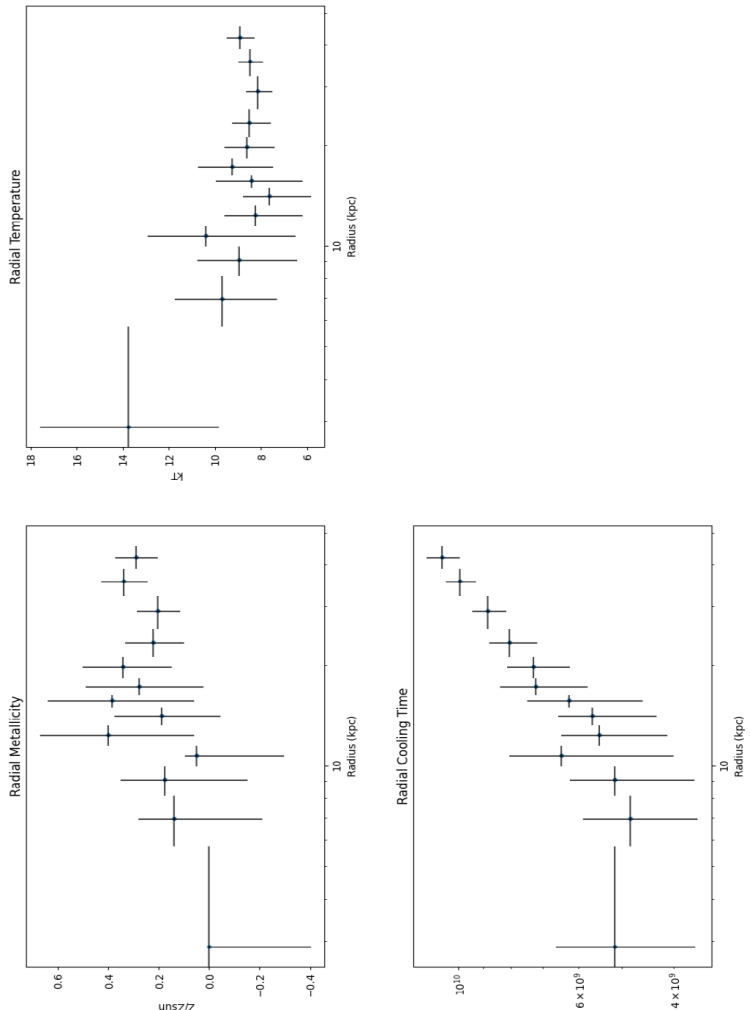
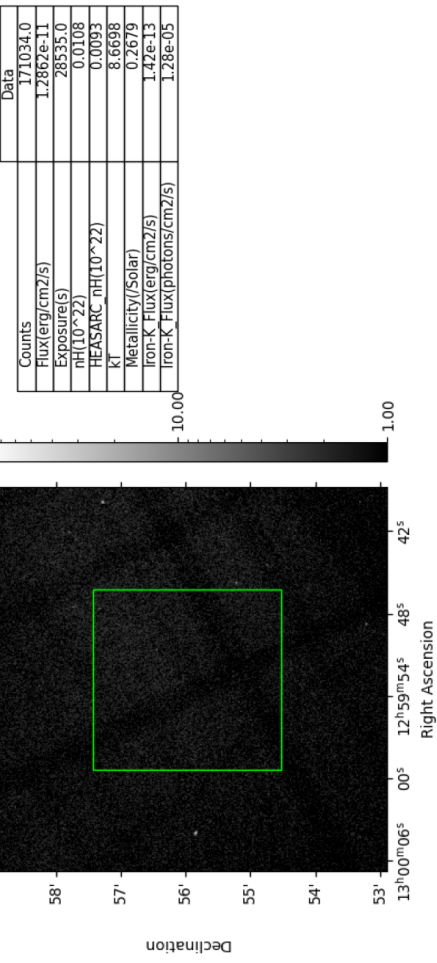
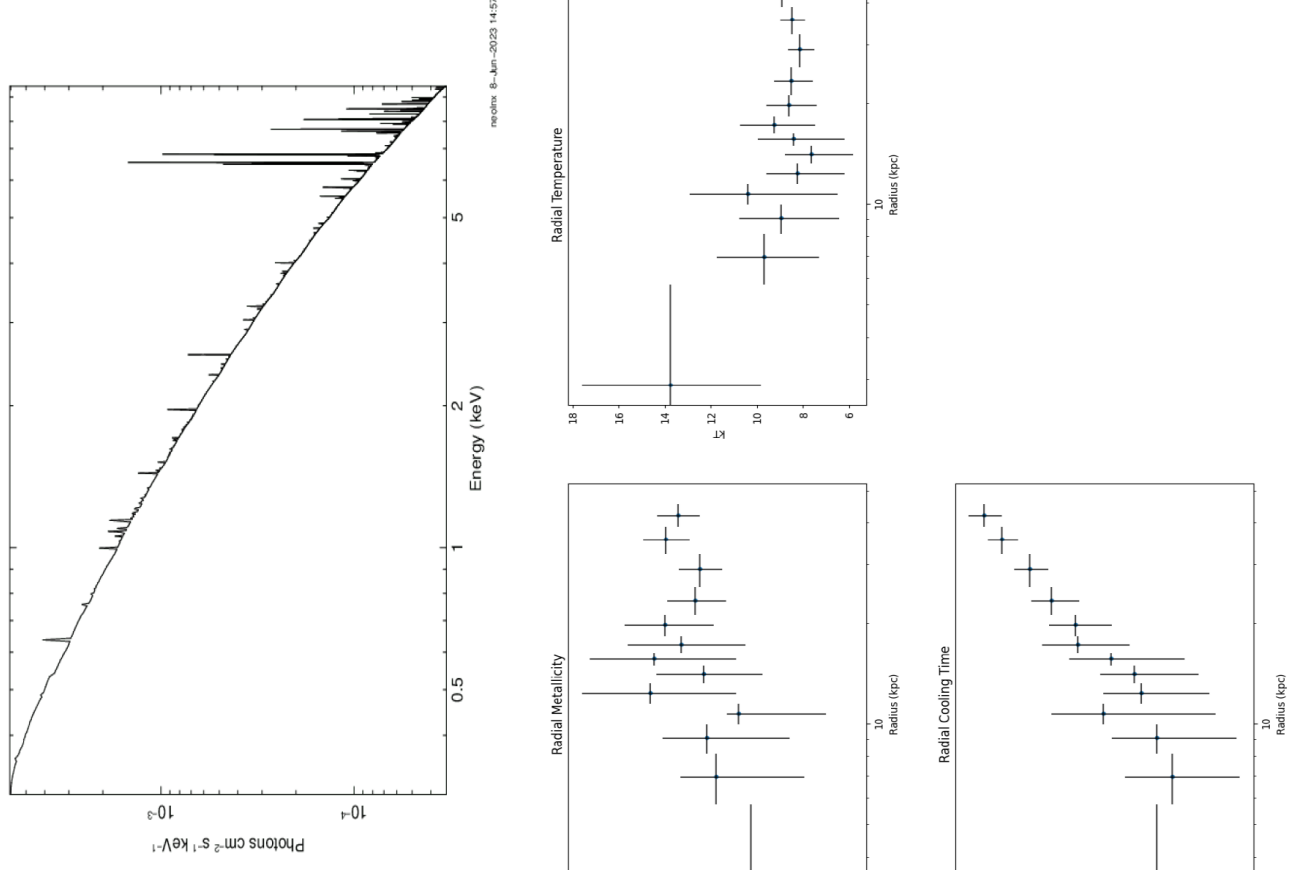


Galaxy Cluster: Centaurus



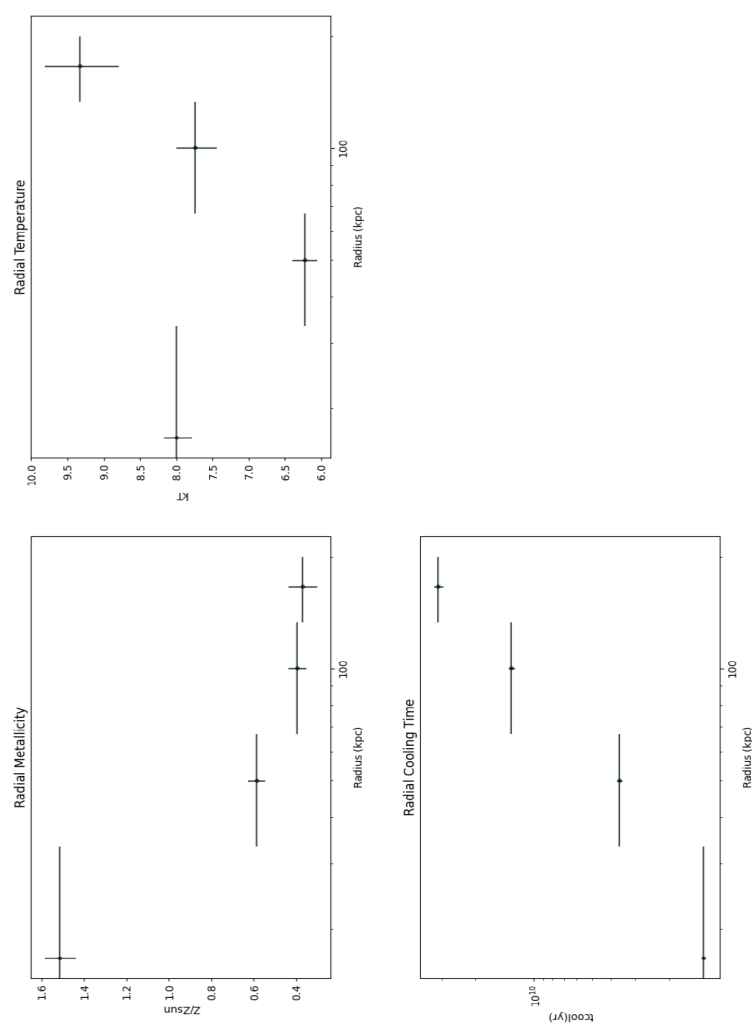
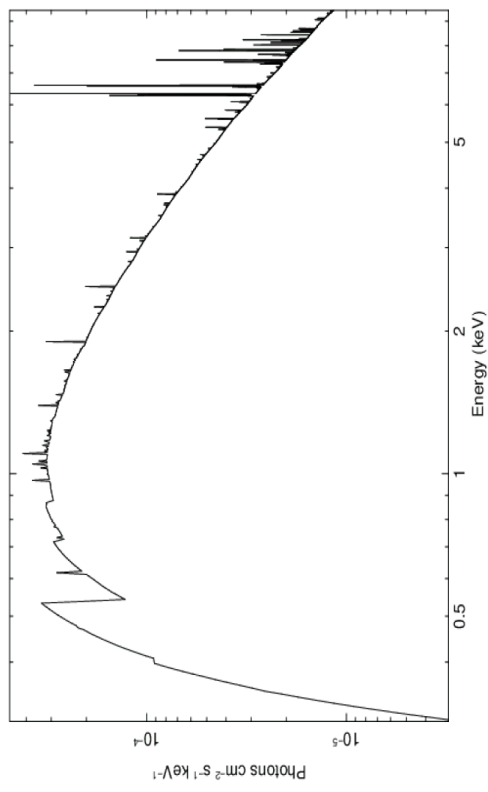
Galaxy Cluster: Coma

Current Theoretical Model

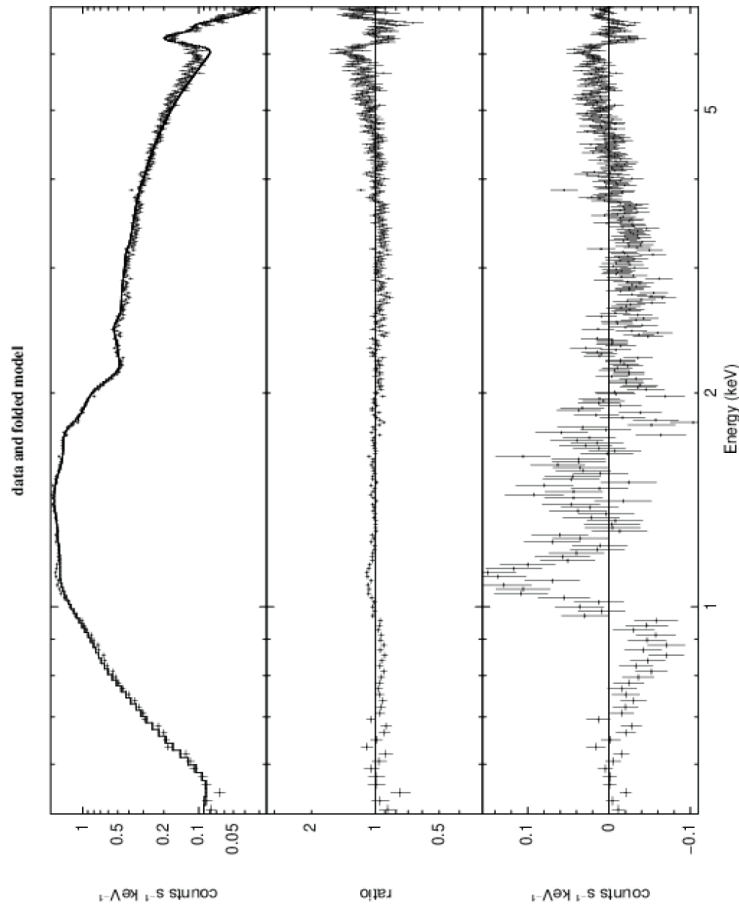
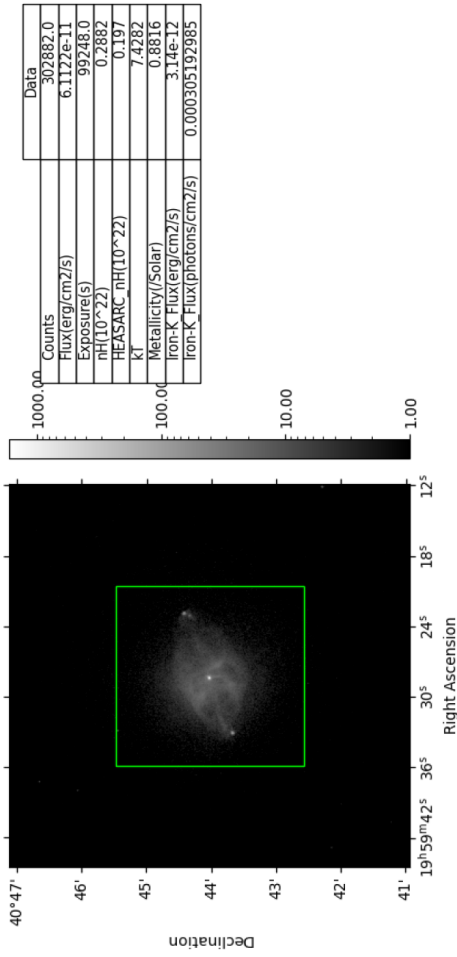


Galaxy Cluster: CygnusA

Current Theoretical Model

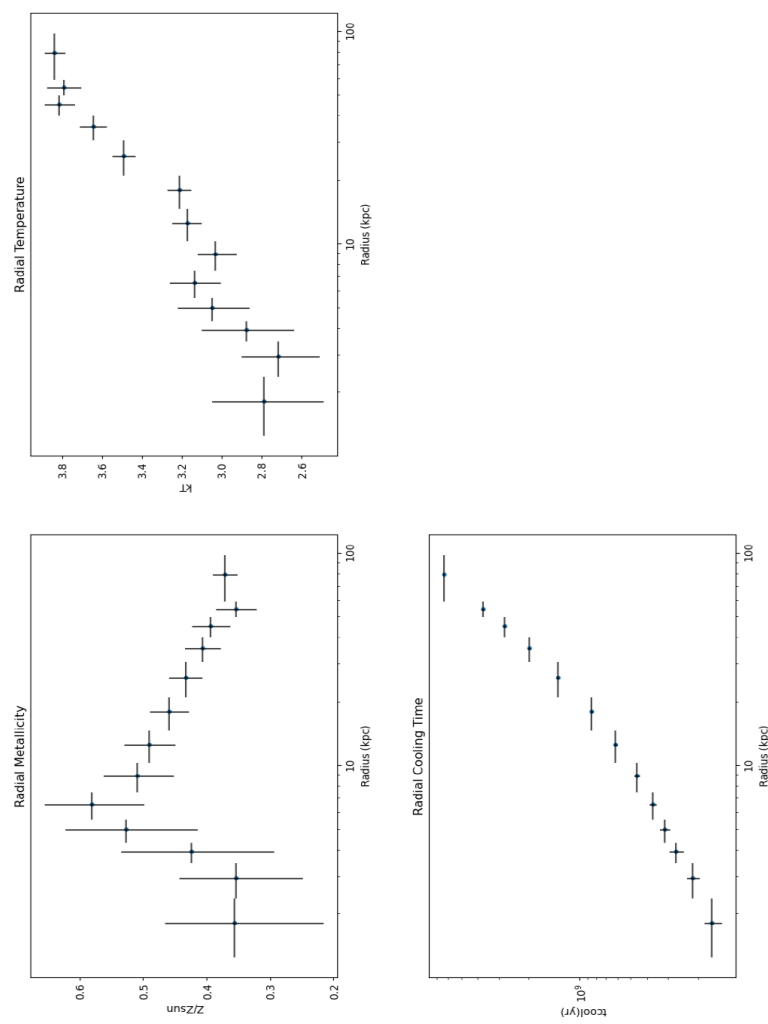
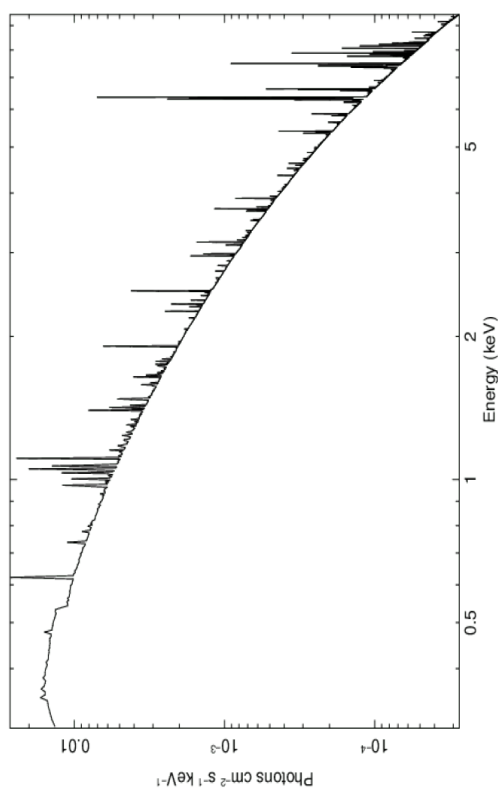


ne01mx 4-Jul-2023 !

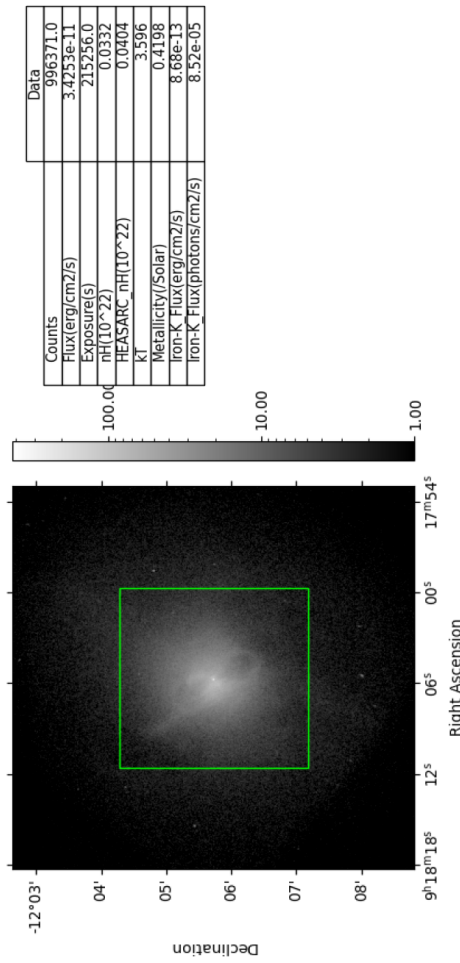


Galaxy Cluster: HydraA

Current Theoretical Model

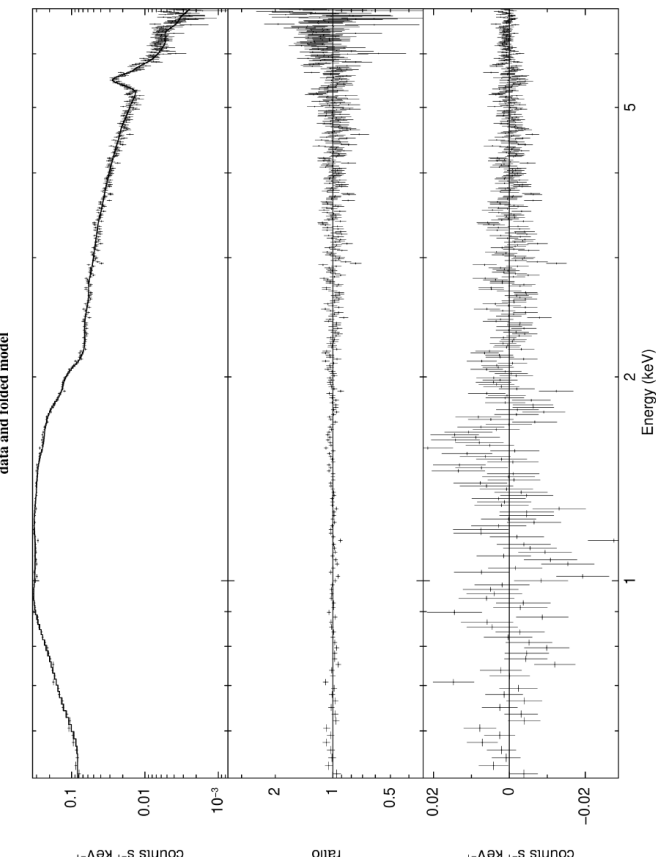
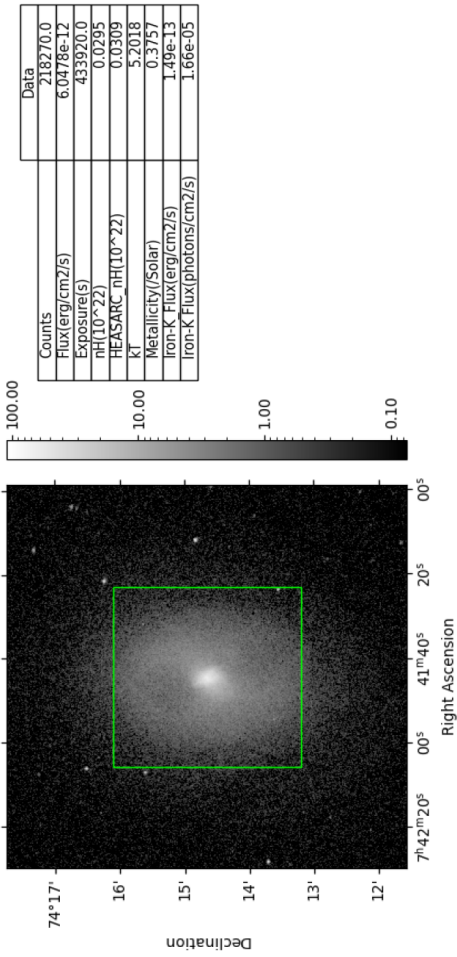
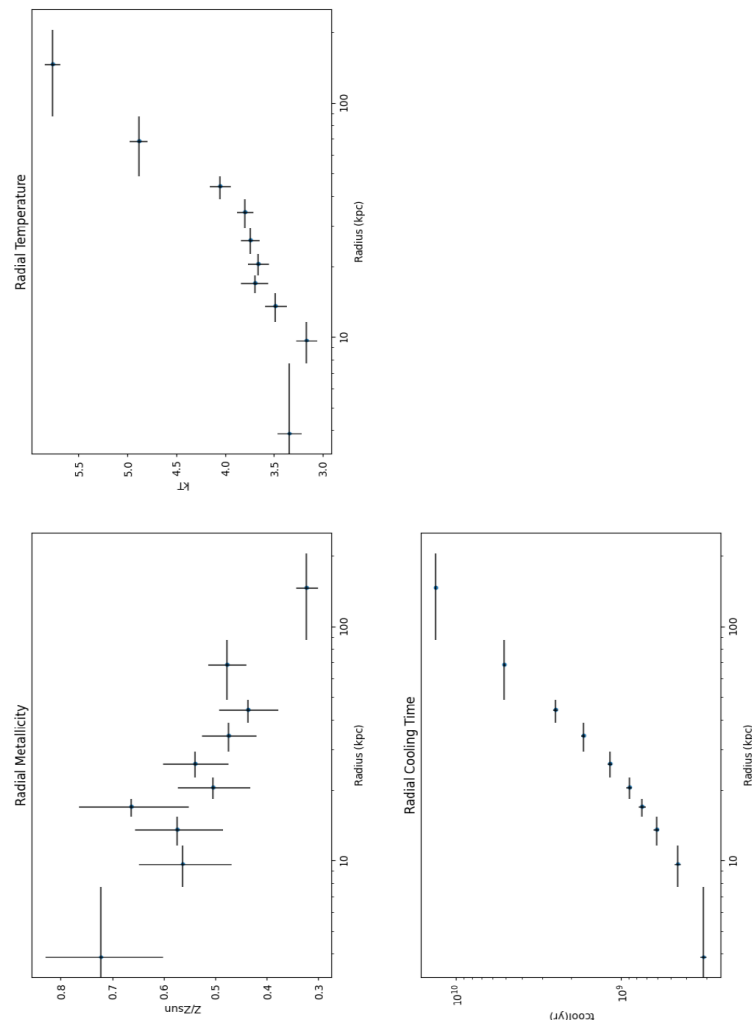
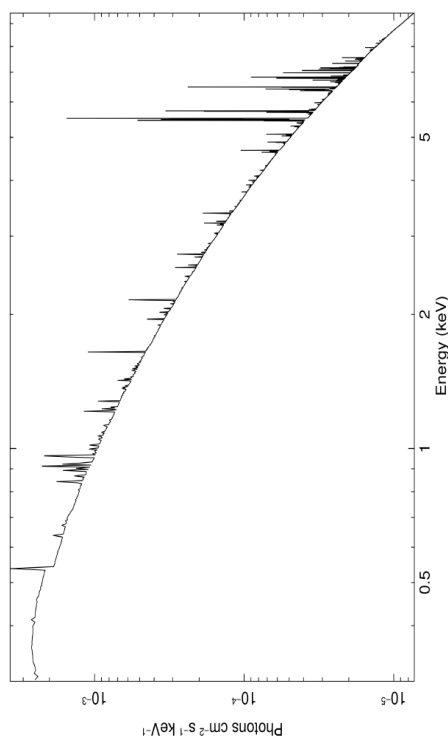


ne01mx 4-Jul-2023 1



Galaxy Cluster: MS07

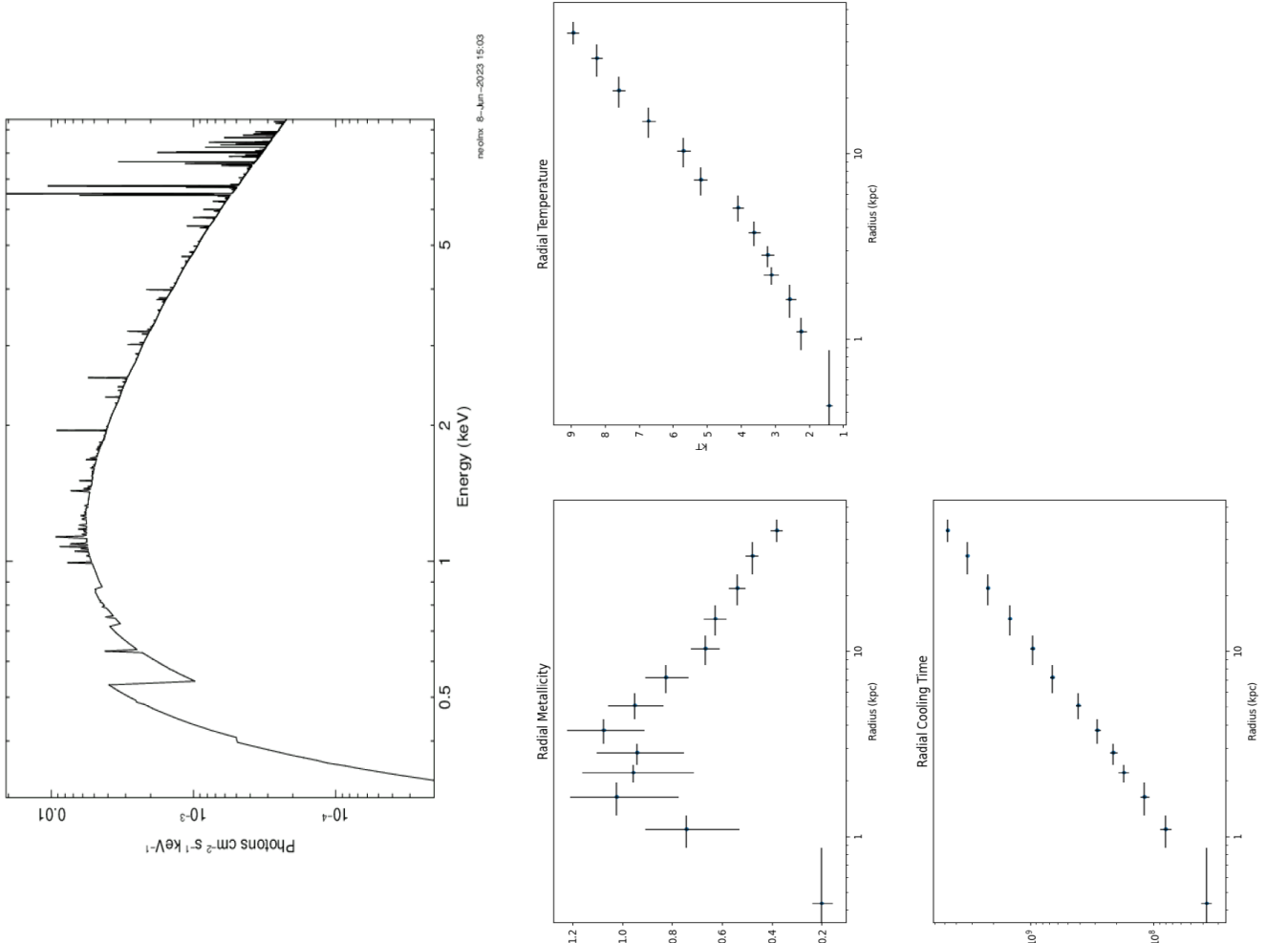
Current Theoretical Model



nebrix 30-May-2023 12:30

Galaxy Cluster: Ophiuchus

Current Theoretical Model



neolmx 19-Jun-2023

